POLITECNICO DI MILANO

FACOLTÀ DI INGEGNERIA DELL'INFORMAZIONE

CORSO DI LAUREA SPECIALISTICA IN INGEGNERIA
DELLE TELECOMUNICAZIONI

RIDGE WAVEGUIDE BANDPASS FILTERS FOR SATELLITE APPLICATIONS

TESI DI LAUREA SPECIALISTICA

Laureando: Vittorio Tornielli di Crestvolant
Matricola: 737753

Relatore: Chiar.mo Prof. Giuseppe Macchiarella
Correlatori: Dr. Christoph Ernst
Ing. Fabrizio De Paolis

Anno Accademico: 2009 - 2010

Try not to become a man of success
but rather to become a man of value.

Albert Einstein

ACKNOWLEDGEMENTS

I would like to thank in particular Fabrizio De Paolis who extensively helped me and Christoph Ernst for the great support and for all the suggestions and things that they tought me during the intership at ESTEC. A great thanks goes to Josè Lorente Acosta who is a very good friend and who patiently helped me giving his experience for both theoretical and simulations aspects. Impossible to forget also another importan person in the passive microwave group of the TEC-ETM section, that is Monica Martinez Mendoza. Many thanks also to Alberto Padilla for his support in the ESTEC microwave laboratory. I would like to thank also the staff of the Machine Shop and in particular Andre Zandvliet and Hanno Ertel who made a great work in the manufacturing of both filter and waveguides tapers even when the times available were very limited. A thanks also to the staff of the microwave laboratory and in particular to Jos Castellein and Kadir who helped and supported me in solving some setups problems related to the RF measurements. Thank to Felice Maria Vanin for his spontaneous help and support. Thank to Prof. Macchiarella for giving me the opportunity to work at ESTEC. Outside ESTEC I had very beautiful times with the "spanish friends" Carmen, Dani, Chevi, Berta, Marta, Monica, Alberto, Josè and with all the other nice people that I met during my stay in Leiden. Thank to Christian who was my office mate for a great part of my intership and who is a very good vuvuzela player. Thank to my parents.

Many thanks to Alice who from Italy constantly encoureged me during the overall period, althought her support was not technical it was undoubtedly essential.

Milano, december 2010 Vittorio Tornielli di Crestvolant

SOMMARIO

I filtri di guida d'onda Ridge sono ampiamente utilizzati in applicazioni satellitari, in particolare nello stage di ingresso quando sono richieste bande larghe ed elevate reiezioni alle spurie. Il lavoro di questa tesi è incentrato sui filtri ridge in uno studio che coinvolge tutte le principali fasi dalla progettazione alla realizzazione di un filtro prototipo. Lo scopo finale è uno studio comparativo tra filtri a singolo ridge e l'approccio convenzionale modulare in guida d'onda rettangolare. Il progetto di questi filtri per bande *C*, *Ku* e *Ka* è costituito da un Input Filter Assembly (IFA), composto di più filtri in cascata. Un primo filtro, in genere passa-banda (BPF) high-order TE_{11n} o TE_{10n}, fornisce la caratteristica IFA in banda e la reiezione vicino ad essa. Un filtro passa-basso (LPF) a larga banda, sopprime la spuria generata dal BPF per un'ampia gamma di bande di frequenza. La tecnica di progettazione qui descritta è stata utilizzata per studiare l'idoneità dei filtri in guida ridge rispetto quella IFA per applicazioni satellitari. Diversi filtri ridge sono stati progettati e simulati per diverse larghezze di banda. Strutture modulari BPF+LPF sono state progettate e simulate con prestazioni analoghe al ridge. I risultati a C-Band mostrano che per larghezze di banda superiori a 480 MHz il prototipo del filtro ridge fornisce prestazioni superiori in banda, offrendo una significativa riduzione di massa e dimensione rispetto all'approccio modulare. Per la progettazione dei filtri ridge è stata sviluppata una nuova sintesi diretta di tipo full-wave. Questa procedura permette di ottenere le dimensioni finali del filtro senza ottimizzazione dell'intera struttura, riducendo significativamente i tempi di sintesi. Essa permette di avere il controllo sul return loss in-banda e sulla reiezione fuori banda. Le simulazioni full-wave mostrano buoni risulati in banda e reiezioni fuori banda oltre la seconda armonica. Inoltre è stato costruito un prototipo in alluminio con la collaborazione di ESTEC machine shop per poi effettuare misurazioni RF che hanno confermato le caratteristiche sia in banda che fuori banda.

ABSTRACT

Ridge waveguide filters are extensively used for satellite payload applications, in particular at the input stages when broad spurious-free performance must be achieved. This thesis is a work focused on the ridge waveguide filters that involves all the main steps from design to realization of breadboard filter. The aim of this work is a comparative study between single ridge filters and conventional rectangular waveguide modular approach. Current design baseline for C-Band, Ku-Band and Ka-Band consists of a complex Input Filter Assembly (IFA), where multiple filter units are cascaded together. A first filter, typically high-order TE_{11n} or TE_{10n} mode BPF, provides the IFA in-band characteristic and the required near-band rejection. A broadband LPF, suppresses the spurious generated by BPF over the wide out of band frequency range. The design technique described here has been employed to study the suitability of ridge waveguide filters to satellite IFA applications. Several C-band ridge filters have been designed and simulated for different bandwidths. As well, conventional modular structures (BPF+LPF) have been designed simulated identical the ridge case. Results at C-Band show that for bandwidths larger than 480 MHz the selected filter prototype provides superior in-band performance while offering significant mass and size reduction with respect to the modular approach. In order to design ridge waveguide filters a novel direct step-by-step full-wave synthesis was employed. This procedure allows to obtain final dimensions of the filter without optimization of the structure, significantly reducing the time for synthesis. This technique permits to have the control on the in-band return loss and out-of-band rejection as well. Trade-off between attenuation losses and high spurious characteristics have been made to obtain optimal filters. Full-wave simulation results show very good in-band performance while preserving spurious-free out-of-band response beyond the second harmonic. Furthermore, a breadboard in aluminum was built with the co-operation of ESTEC machine shop and RF measurements have been conducted to confirm both in-band and out-of-band features.

CONTENTS

LIST OF FIGURES

LIST OF TABLES

ACRONYMS

ESA	European Space Agency
ESTEC	european space research and technology center
EM	electromagnetic
PEC	perfect electric conductor
RL	return loss
IL	insertion loss
BW	bandwidth
TRM	transverse resonance method
VSWR	voltage standing wave ratio
TE	transverse electric
TM	transverse magnetic
TEM	transverse electromagnetic
SFR	spurius free range
LNA	low noise amplifier
RF	radio frequency
LPF	low pass filter
BPF	band pass filter
VNA	vectorial network analyzer
CAD	computer-aided design
STDV	standard deviation
DEV	deviation
DUT	device under test
SOLT	short open load through
TRL	through reflected line
IFA	input filter assembly

ESTRATTO IN ITALIANO

I filtri in guida ridge sono ampiamente utilizzati in applicazioni satellitari per i loro vantaggi in termini di ingombro e riduzione della massa complessiva. Se si paragonano con le guide d'onda rettangolari, si può notare una significativa riduzione della frequenza di cutoff ed un allargamento della banda operazionale. La riduzione del cutoff porta ad una riduzione delle dimensioni trasverse. Lo scopo di questa tesi è quello di effettuare un paragone tra il filtro in guida ridge e l'approccio modulare comunemente usato come filtro di front-end nei payload satellitari, dove sono necessari filtri con caratteristiche di banda larga e con elevate reiezioni fuori banda. Filtri in guida ridge aventi la stessa frequenza ma con differenti larghezze di banda sono stati paragonati in termine di insertion loss con una baseline composta dalla cascata di un passabanda e un passabasso aventi medesima larghezza di banda e reiezione fuori banda. Per permettere questo tipo di studio, è stata sviluppata una nuova procedure di sintesi diretta che consente, partendo dalle specifiche, di arrivare alle dimensioni finali del filtro senza il bisogno di operare una ottimizzazione all'intera struttura finale, riducendo così notevolmente i tempi di sintesi. La procedura di sintesi descritta consente altresì di avere il pieno controllo sulla spuria fuori banda e sul return loss in banda. Successivamente, è stato costruito un filtro ridge prototipo presso il machine shop di ESTEC. Dopo la costruzione sono state effettuate su di esso prima misure di carattere metrologico per verificare l'effettivo rispetto delle tolleranze della macchina dichiarate in precedenza, mentre poi sono state svolte misure a radio frequenza nel laboratorio di microonde utilizzando l'analizzatore di rete. Si è verificato così il comportamento del filtro sia in banda che fuori banda.

La presente tesi è composta dai seguenti capitoli:

CAPITOLO 2 : in questo capitolo vengono descritte le proprietà della guida d'onda ridge, soffermandosi sulla configurazione a singolo ridge.

CAPITOLO 3 : viene presentata una nuova procedura di sintesi diretta che consente di arrivare alle dimensioni della guida partendo dalle specifiche del filtro ed in particolare avendo la possibilità di controllare la risposta fuori banda del filtro.

CAPITOLO 4 : il filtro in guida ridge viene paragonato con il filtro IFA avente stesso ordine, banda e reiezione della spuria. Viene fatto un confronto tra i due suddetti filtri in termini di perdita di inserzione a frequenza centrale per diverse larghezze di banda.

CAPITOLO 5 : descrive il processo di fabbricazione del filtro e dei taper necessari per le misure fuori banda. Successivamente vengono presentati i risultati delle misure metrologiche e quelle a radio frequenza sia in banda che fuori banda

APPENDICE A : in questa appendice si trova la teoria di base sui filtri necessaria per la comprensione degli argomenti presentati in questa sede.

Questo lavoro è stato condotto in uno stage di sei mesi presso lo European Space Research and Technology Center dell'Agenzia Spaziale Europea che si trova a Noordwijk, Paesi Bassi.

GUIDA D'ONDA RIDGE

La guida d'onda rigde rispetto alle guide rettangolari o circolari, è caratterizzata dalla presenza di uno o più setti detti *ridge* al suo interno. Le principali caratteristiche di questo tipo di guida sono: la propagazione del modo TE_{10} per il modo fondamentale, ridotta frequenza di cutoff, ampie larghezze di banda tra il modo fondamentale e il primo modo successivo, ridotti valori di impedenza se comparati con una guida d'onda rettangolare di uguali dimensioni. In questa Tesi verrà trattata la configurazione a singolo ridge sia per motivi di maggiore semplicità realizzativa, che per il vantaggio di avere meno errori dovuti alle tolleranze di fabbricazione. Dal punto di vista del circuito equivalente, un tratto di guida ridge può essere modellizzato con il circuito 3 dove si nota la presenza di due capacità. Utilizzando il metodo della risonanza trasversa, è possibile ricavare le frequenze di cutoff del modo fondamentale per diverse dimensioni del ridge. Il grafico parametrico di figura 4 mostra il valore della lunghezza d'onda di cutoff λ_c normalizzata alla dimensione della guida esterna a per diversi valori di s e d. Il significato dei parametri e delle lettere precedenti è esplicitato in figura 1 sia per il singolo che per il doppio ridge. In particolare, ci si riferirà alla dimensione d anche con il nome *gap*. Altra proprietà fondamentale della guida d'onda ridge è la grande banda in termini di differenza tra la frequenza di cutoff del primo modo superiore e del

modo fondamentale. Tali valori di banda sono rappresentati nel grafico parametrico 6 per diversi valori di s/a e d/b. I valori di attenuazione della guida ridge per diverse bande e per diverse dimensioni s/a sono invece rappresentati nel graifico di figura 7 nel quale i valori di α_n vogliono stare a significare i valori dell'attenuazione della guida ridge rispetto all'attenuazione in una guida rettangolare avente medesime caratteristiche. Da questo grafico si può notare come per bande larghe (e quindi solitamente per piccoli valori del gap), le attenuazioni possono essere anche 10 volte maggiori rispetto alla classica guida rettangolare. Per quanto riguarda il valore dell'impedenza caratteristica ad una certa frequenza ω, essa dipende dal valore a frequenza infinita per un fattore di scala definito nell'equazione (2.20). Per questo motivo, si può calcolare l'impedenza caratteristica della guida ridge ad una certa frequenza una volta conosciuto il valore dell'impedenza a frequenza infinita, servendosi dei grafici parametrici di figure 10, 8 e 9 a seconda che si stia utilizzando una definizione del tipo *power-current*, *power-voltage* o *voltage-current*. Un volta che sono state definite le specifiche della guida d'onda, è possibile sfruttare i grafici prima elencati per trovare le dimensioni trasverse della guida.

SINTESI DIMENSIONALE

Un nuovo metodo di sintesi diretta del filtro in guida ridge viene presentato in questo capitolo. Innanzitutto occorre precisare che la struttura di filtro passabanda ridge qui utilizzata è quella composta da risonatori come linee di trasmissione, direttamente accoppiate tramite invertitori di impedenza. Le linee di trasmissione sono i tratti di guida ridge, mentre gli accoppiamenti sono tratti di guida d'onda rettangolare aventi le stesse dimensioni a e b delle linee ridge. Da quanto detto nel capitolo della guida d'onda ridge, si evince che se le dimensioni dei due tratti di linea sono le stesse, accade che si ha propagazione nel ridge e si è invece sotto la frequenza di taglio nel tratto di guida rettangolare. Per questo motivo i tratti rettangolari vengono detti anche tratti *evanescenti*. La sintesi consta così di due step: nel primo si definiscono le dimensioni trasverse della guida ridge, nel secondo si trovano le lunghezze sia dei risonatori ridge in propagazione che dei tratti di guida rettangolare sotto il taglio. Per fare ciò viene proposta una procedura a sintesi diretta. Nello scenario che si sta considerando, i seguenti punti meritano di essere sottolineati:

- Tutti i risonatori ridge hanno le stesse dimensioni e la stessa frequenza di cutoff e sono in propagazione, mentre
- tutti i tratti a guida rettangolare hanno la stessa frequenza di cutoff tra loro e sono sotto il taglio.

Le guide d'onda rettangolari aventi dimensioni trasverse costanti ed operanti sotto il taglio realizzano gli invertitori di impedenza, come i tratti ridge a gap costante realizzano serie risonatori $\lambda_g/2$. Il cutoff del modo TE_{10} determina le dimensioni a e b dei tratti ridge e di quelli evanescenti. Quando la frequenza di cutoff è vicina alla banda passante del filtro, la risonanza è essenzialmente confinata al risonatore e la lunghezza della linea ridge è maggiore di quella tratto evanescente. In questo caso il filtro opera maggiormente come filtro direttamente accoppiato con gli elementi di guida evanescente che fungono da invertitori. Se invece la frequenza di cutoff è lontana dalla banda passante del filtro ($f_c \ll f_0$) la risonanza si distrubuisce tra la guida sotto il taglio e la guida in propagazione, avendo come conseguenza una riduzione della lunghezza del ridge ed un aumento di quella del tratto evanescente. Quando la lunghezza dei risonatori diventa piccola rispetto la lunghezza d'onda in guida ($l < \lambda_g/10$) il filtro opera come se avesse delle induttanze concentrate in serie con degli accoppiamenti induttivi.

Il design della sezione trasversa del ridge si effettua utilizzando i grafici presentati del capitolo 2 e seguendo gli step sotto indicati:

1. Definizione dei requisiti a radio frequenza: perdita di inserzione, reiezione fuori banda, potenza.
2. Definizione della geometria del ridge valutando preliminarmente le dimensioni a, b, s a d. Inizialmente, s e d sono scelti sulla base dei vincoli realizzativi. Dopodiché una corretta combinazione dei parametri a e b deve essere trovata in accordo con la progazione del modo TE_{20} della guida ridge. Questo modo è sempre il secondo modo superiore e dove sempre essere collocato oltre la frequenza più alta specificata dalle specifiche di reiezione fuori banda. Inoltre, il progettista deve assicurare che il cutoff della guida rettangolare sia sempre al di sotto del range di frequenze specificate dal filtro.
3. Valutazione dell'ottima dimensione del gap d in accordo la frequenza di cutoff del TE_{10} e della banda desiderata utilizzando i grafici 4 e 6. Diminuedo la dimensione del gap è possibile migliorare considerabilmente la reiezione

fuori banda e ridurre la dimensione complessiva del filtro. Tuttavia, dal momento che il gap del ridge non può essere eccessivamente piccolo per i motivi relativi al fattore di merito Q, potenza e vincoli realizzativi, la reiezione delle spurie e la riduzione delle dimensioni del filtro possono venire limitate.

4. Calcolo dell'impedenza caratteristica del ridge e valutazione dei requisiti di adattamento di impedenza.

Una volta definita la sezione trasversa si provvede alla sintesi delle lughezze dei risonatori e degli accoppiamenti.

Il modello dei tratti sotto il taglio è rappresentato con i circuiti di figura 19. Il tratto evanescente opera la funzione di inversione e due tratti di linea $\Delta l_{i,i+1}$ vanno a correggere la lunghezza dei risonatori adiacenti in modo da aggiustare la frequenza di risonanza che verrebbe altrimenti modificata dalla presenza della discontinuità. Il metodo che viene proposto si basa sull'uso del simulatore full-wave. Inizialmente vengono definiti i parametri di scatter dell'invertitore le cui formulazioni dipendono dal valore K (3.4). L'idea di base è quella di utilizzare l'analisi full-wave per ottenere la lunghezza del tratto sotto il taglio e del tratto ridge direttamente. Questo può essere fatto valutando i parametri S di una struttura composta da due tratti ridge collegati da un tratto evanescente di guida rettangolare. Ponendo i piani di riferimento delle porte di ingresso e uscita in corrispondenza del tratto di linea rettangolare, si può effettuare la simulazione elettromagnetica e valutare i parametri di scatter del tratto sotto il taglio che funge da invertitore. La relazione che lega il modulo di S_{21} con il parametro K è esplicitato nella (3.6). La lunghezza del risonatore viene data dalla formula (3.10) dove Φ_i e Φ_{i+1} sono rispettivamente le fasi di S_{11} del tratto sotto il taglio valutati alla frequenza centrale dei tratti evanescenti a destra e sinistra del risonatore. Questo metodo è particolarmente veloce in quanto non richiede molte risorse computazionali, inoltre i parametri S_{11} e S_{21} sono facilmente estrapolabili da qualsiasi simulatore full wave.

La procedura di sintesi che si propone è quindi la seguente:

1. Determinare il numero di risonatori N e i valori degli invertitori K o J usando i polinomi di Tchebycheff le cui formulazioni si trovano in appendice A.

2. Determinare le lunghezze iniziali dei tratti evanescenti che ottengono il valore desiderato di inversione a f_0 usando ad esempio charatterizzazioni della discontinuità in modo

analitico. Le lunghezze dei tratti sotto il taglio sono poi corrette in modo da ottenere i corretti valori di inversione K utilizzando la formula (3.6). Se si accorcia un guida d'onda evanescente si aumenta il valore di accoppiamento e viceversa. Come conseguenza si ha che la larghezza di banda di questi tipi di filtri viene controllata dal corretto dimensionamento degli accoppiamenti.

3. Determinazione della lunghezza dei risonatori. Essi nominalmente sono lunghi $\lambda_g/2$. Qualora si accorci un tratto di guida ridge si aumenta la frequenza di risonanza mentre se lo si allunga la frequenza di risonanza diminuisce. Come conseguenza, la frequenza centrale del filtro può essere controllata aggiustando le lunghezze dei tratti ridge. Nella pratica, le discontinuità con la guida sotto il taglio devono essere considerati. Per questo la lunghezza nominale dei risonatori viene determinata per mezzo della formula (3.10)

A questo punto il filtro presenta la corretta risposta in banda con tutti i poli visibili e un return loss equiripple. Per correggere l'errore dovuto alla dispersione del filtro si può utilizzare la teoria di Levy la quale correggere lo shift in frequenza che si nota per i filtri a bande più larghe. Vegono poi presentati i risultati delle simulazioni per filtri a banda *Ka* e banda *C*. Si fa notare come si è in grado di controllare la spuria del filtro modificando le dimensioni trasverse della guida ridge. Nella prima classe di filtri a banda *Ka* la sezione trasversa è stata scelta per ottenere prestazioni ottimali in termini di fattore Q, mentre nella seconda si sono modificate tali dimensioni in modo da avere reiezioni oltre la seconda armonica. I risultati confermano tale aspettativa, inoltre si osserva che si è in grado di ottenere anche reiezioni superiori fino oltre la terza armonica. Successivamente vengono presentati i risultati della sintesi per filtri a banda *C* confermando ancora una volta i dati di prima.

Per interfacciare il filtro con sistemi standard si è scelto di implementare un transformer di impedenza per la classe di filtri a banda *C*. Viene quindi presentata la procedura classica di sintesi del transformer e la relativa. risposta Il voltage stanging wave ratio (VSWR) del caso peggiore, per questo transformer, è pari a 1.08.

Viene presentato anche un metodo alternativo per la sintesi del filtro ridge che fa riferimento all'articolo di Zaki del 1987. In questo articolo viene presentato un metodo per il calcolo del coefficiente di accoppiamento tra due risonatori dielettrici circolari. Nella nostra sede si applica questo approccio al caso di riso-

natori ridge accoppiati da tratti di guida sotto il taglio. I risultati di questa procedura per bande *C* mostrano filtri che rispecchiano perfettamente le specifiche sia in termini di larghezza di banda che in termini di equiripple return loss. Questo metodo richiede però un secondo step per filtri a larga banda.

CONFRONTO TRA IL FILTRO RIDGE E L'APPROCCIO MODULARE

La struttura di un payload satellitare viene raffigurata in 45. In questa figura si notano il filtro di front end, l'amplificatore a basso rumore, il down converter, lo stadio di demultiplexer, gli amplificatori di potenza, i multiplexer e il filtro di output. Ponendo la nostra attenzione sullo stadio di input, le principali caratteristiche di questo filtro sono la larga banda, la ridotta perdita di inserzione e l'alta reiezione delle spurie per evitare che nel sistema entrino componenti frequenziali non desiderate. I tradizionali filtri in guida d'onda rettangolare ad iris induttivo non sono in grado di soddisfare il requisito dell'elevata reiezione fuori banda. Il grafico di figura 47 mostra come per un filtro composto da risonatori $\lambda_g/2$ la spuria si trovi a $1.5f_0$. Non potendo soddisfare il requisito di reiezione fino, ad esempio, la seconda armonica si risolve questo problema ponendo in cascata al passabanda un filtro passabasso a larga banda che ha il compito di pulire la spuria. Questa configurazione fatta da passabanda + passabasso viene detta *approccio modulare* o Input Filter Assembly (IFA).

Ciò che ci si propone è capire se il filtro in guida ridge studiato precedentemente è in grado di sostituire il filtro IFA. Per questo vengono confrontate una categoria di filtri IFA aventi reiezione oltre la seconda armonica, con un classe di filtri in guida ridge con stesse prestazioni. Il confronto viene fatto in termini di perdita di inserzione calcolata a f_0. Com'è noto, l'insertion loss diminuisce all'aumentare della larghezza di banda, per questo motivo sono stati progettati una serie di filtri ridge aventi tutti stessa frequenza centrale, ordine, return loss e spuria ma con differenti larghezze di banda. Allo stesso modo sono stati progettati filtri IFA composti da un filtro passabanda ad iris induttivi aventi stesse caratteristiche a radiofrequenza rispetto a quelli ridge, e un passabasso di riferimento. Le perdite di inserzione per le due classi di filtri sono state simulate e proposte nel grafico di figura 54. In questo grafico si nota come per banda stretta le perdite del ridge siano superiori rispetto all'approccio

modulare, tuttavia, ad un allargamento della banda le perdite di inserzione del ridge diventano comparabili con il filtro IFA fino a diventare inferiori oltre una certa larghezza di banda. Questo dimostra che il filtro ridge è un buon candidato alternativo a questo tipo di approccio modulare. Inoltre, il filtro ridge ha svariati vantaggi in termini di ingombro e di peso. La figura 52 mostra i due tipi di filtri in scala l'uno accanto all'altro. Risultano così evidenti i vantaggi in termine di spazio occupato e ingombro.

COSTRUZIONE DEL PROTOTIPO E MISURE

Con la collaborazione del machine shop dell'ESTEC è stato costruito un filtro ridge prototipo. Il filtro è stato costruito in alluminio. Prima di arrivare però alla costruzione, si sono svolti ulteriori studi sul filtro. Per prima cosa è stata effettuata un analisi delle tolleranze. Il machine shop ha dichiarato che l'incertezza dovuta agli errori di fabbricazione è pari a $20\,\mu m$. Ciò significa che le dimensioni avranno una distribuzione statistica di tipo gaussiano centrata sul valore nominale e con deviazione standard di $20\,\mu m$. Per questo è stata svolta un'analisi alle tolleranze facendo variare le dimensioni nominali in modo randomico con distrubuzione normale e deviazione standard dichiarata dal machine shop. I risultati di questa analisi sono mostrati nei grafici di figura 59. In particolare si sono rappresentati i risultati delle conseguenze sui parametri S facendo variare nel primo caso tutte le dimensioni ad eccezion fatta dei gap, e nel secondo anche i gap. Si osserva che nella prima analisi il filtro pare non molto sensibile alle tolleranze: si registra un buon return loss e gli shift in frequenza sono praticamente inesistenti. Nel secondo caso però gli errori hanno effetti devastanti sulla caratteristica. Questo significa che questa categoria di filtri è molto sensibile alle tolleranze in particolare per gli errori sul gap. Si è perciò deciso di procedere alla costruzione del prototipo composto dal filtro e un *lid* che lo chiude al top. Per via della grande sensibilità dei gap, si è deciso di costruire 2 lid. Così facendo se la caratteristica dovesse risultare non conforme alle specifiche si andranno ad inserire delle viti di tuning in uno dei due lid. Inoltre, dal momento che il lid chiude la parte superiore del filtro, se l'errore di fabbricazione sul singolo gap porta ad un aumento dello stesso, questo può essere compensato con una vite di tuning ad esempio, ma se l'errore comporta un riduzione del gap con la configurazione attuale non ci sarebbe modo di poterlo correggere. Per questo motivo è stato deciso di aumentare tutti i gap del valore di tolleranza dichiarato dal machine shop e cioè

di 20 µm. L'effetto dell'aumento dei gap è quello di un shift in frequenza della caratteristica come evidenziato dalla figura 60. Per la costruzione si è usata la milling machine; per maggiori dettagli circa il processo di fabbricazione si faccia riferimento al capitolo 5.

Successivamente alla costruzione si sono svolte misure metrologiche per verificare che le misure e le tolleranze precedentemente dichiarate dal machine shop siano state effettivamente rispettate. Le misure metrologiche sono state svolte nel laboratorio di metrologia dell'ESTEC e sono state condotte con una incertezza di misura di 2.95 µm. Le tabelle elencano tutte le misure e le deviazioni rispetto al valore nominale. Si può notare che i gap hanno una deviazione finale molto inferiore rispetto a quella dichiarata. Il gap peggiore ha una deviazione rispetto al valore nominale di 8 µm. Questo è dovuto essenzialmente al tipo di processo di fabbricazione che è stato notevolmente avvantaggiato in quanto tutti i gap erano costanti.

Alla fine sono state svolte le misure a radio frequenza tramite un analizzatore di rete nel laboratorio di microonde di ESTEC. Sono state qui svolte misure sia in banda che fuori banda. Le misure in banda mostrano che la caratteristica del filtro ridge è molto migliore rispetta quella prospettata dall'analisi alle tolleranze. Inoltre si nota uno shift in frequenza di 10 MHz rispetto al filtro simulato. La figura 73b mostra su uno stesso grafico sia i valori misurati che quelli teorici della simulazione. Si può così constatare che non sono necessarie dei dispositivi di tuning in quanto il return loss del caso peggiore è di -20 dB. Sono state effettuate anche misure fuori banda con l'aiuto di tapers per l'adattamento della porta d'ingresso WR-137 con le transizioni. Sebbene, per mancanza nel laboratorio di alcuni kit di calibrazione, alcuni risultati risultino meno accurati rispetto ad una corretta calibrazione i risultati mostrano che la presenza della spuria è a 14 GHz proprio come ci si aspettava dalla simulazione.

CONCLUSIONI

In questo lavoro la sintesi e le applicazioni dei filtri passa banda in guida ridge sono state presentate. Le performance di questi filtri sono state dimostrate essere in accordo con le specifiche di reiezione della spuria oltre la seconda armonica. Si è mostrato anche come sia possibile controllare la reiezione fuori banda agendo sulle dimensioni transverse della guida. Le dimensioni del gap devono essere scelte in modo da effettuare un compromesso tra i requisiti di elevate reiezioni e ridotte attenuazioni.

Questo trade-off è stato mostrato per i filtri in banda *C* con buoni risultati.

Sono state inoltre presentate due diverse tecniche di sintesi. L'errore riguardo l'eccessivo allargamento di banda che si nota nella prima metodologia è essenzialmente dovuta all'erroneo metodo di calcolo dello slope e quindi dell'errato valore dell'invertitore K. Una spiegazione di questo fenomeno può essere compresa facendo riferimento alla distribuzione dei campi di figura 44. Si nota cioé che il modo della risonanza non è un TE puro ma assomiglia ad un TEM. Dal momento che non ci si trova ne nel caso di risonanza del modo TE ne del modo TEM, questa discussione è lasciata come sviluppo futuro. Inoltre con la ridotta lunghezza dei risonatori ($l \approx \lambda_g/10$) la risonanza non è del tutto confinata all'interno del risonatore ma è distribuita anche nel tratto di linea sotto il taglio.

La tecnica descritta dall'articolo dei Zaki per risonatori dielettrici è stata qui applicata ai risonatori ridge del filtro in discussione. Questo motodo mostra di poter raggiungere ottimi risultati in banda consentendo di ottenere esattamente la larghezza di banda secondo le specifiche. Essa mostra che per bande strette ($w = 1\%$) si è in grado di arrivare direttamente alle dimensioni finali del filtro mentre per bande larghe ($w = 10\%$) è necessario un secondo step.

Lo schema a blocchi di un payload satellitare è stato presentato così come le principali specifiche del filtro di input. L'approccio modulare costituito dalla cascata di un filtro passabanda e di uno passabasso è stato descritto e paragonato con i filtri in guida ridge ottenuti con i metodi di sintesi qui descritti. Per le bande di interesse, è stato provato che la caratteristica fuori banda non viene alterata in quanto essa dipende dalle dimensioni trasverse della guida. Per questo motivo l'errore che si è riscontrato sull'allargamento di banda dovuta alla sintesi, non è affatto critica in quanto il paragone con l'approccio modulare viene svolto a parità di banda effettiva o misurata. Qualora l'applicazione richiedesse esattamente una certa larghezza di banda, si può utilizzare il metodo Zaki qui descritto che è stato provato dare ottimi risultati a riguardo anche se richiede costi computazionali più onerosi. Il confronto con l'approccio modulare mostra come per larghe bande la perdita d'inserzione del ridge sia migliore di quella del filtro IFA.

Un filtro prototipo è stato costruito e poi sono state effettuate sia misure di tipo metrologico che a radiofrequenza. Le misure in banda dimostrano un return loss del caso peggiore pari a $-20\,\mathrm{dB}$ senza dispositivi di tuning. Il fuori banda risulta invece pulito e la spuria si trova a $14\,\mathrm{GHz}$ come ci si aspettava.

Per la caratteristica fuori banda, migliori perdite di inserzione per larghe bande e ridotto ingombro e dimensioni rispetto al filtro IFA, si conclude che il filtro ridge può essere un buon candidato come filtro di input per il payload satellitare.

1 INTRODUCTION

RIDGE waveguide bandpass filters are extensively used in many satellite applications for their advantages in terms of mass and size reduction. Compared to rectangular waveguides, ridge waveguides show the advantages of very wide fundamental mode operation bandwidths and low cutoff frequency. The low cutoff frequency yields a small cross section and hence a compact size of ridge waveguide components. Furthermore, great design flexibility exists in ridge configuration, according to different electrical and mechanical requirements: single or double ridge, triple ridge, and single or double antipodal ridge. In light of the described advantages, evanescent-mode ridge waveguide filters have found considerable attention in many telecommunication, terrestrial and space applications because of their wide, spurious free out-of-band response, compact size, and reduced weight. The price to pay is in terms of insertion loss and power handling capability, making ridge waveguide filters ideal candidates for applications at receiver front-end or after down-conversion. Several papers have been published on the topic [28, 30–33, 36] however no information on how to derive the filter dimensions is provided and optimization-based design techiques are routinely employed. Furthermore, other design methods neglect any negative impacts on the out-of-band rejection performance [12], [4]. In this study we focused on the single ridge waveguide due to its semplicity in term of manufacturing, tolerances and mechanicals advantages. In [39, 43] is possible to find some interesting works on different types of ridge waveguides.

The aim of this work is to investigate the suitability of ridge waveguide bandpass filter at the front-end of a satellite payload, where wide bandwidths and high spurious rejections are necessary prerequisites. A comparison in term of insertion loss between ridge filters and state of art modular approach input filter assembly (IFA) for several bandwidths have been made. For making this study, several ridge filters have been designed with a novel full-wave technique that lets get final dimensions starting from specifications without the need for optimization of the overall structure. This direct synthesis permits to control the out of band rejection and the in-band return loss as well. The present work is structured as follows:

CHAPTER 2 : the fundamental properties and features of the ridge waveguide are presented and described.

CHAPTER 3 : a novel procedure for the synthesis of a single ridge waveguide filter that allows to obtain final dimensions of the filter starting from specifications is presented. Great importance in given to the control of the out of band rejection.

CHAPTER 4 : ridge waveguide filter is compare with standard rectangular waveguide modular approach of same order, bandwidths and central frequency. A comparison in term of insertion loss is made at the end of the chapter.

CHAPTER 5 : describes the manufacturing and measurements of a prototype ridge waveguide filter. Mechanical aspects and problematics involved in building are discussed. Measurements of physical dimensions and of the radio frequency (RF) in band and out of band responses are presented.

APPENDIX A : the basic filter's theory necessary for the design of the filter is proposed.

This work was conducted with the support of the European Space Agency (ESA) in a six months intership, from March to September 2010, at the european space research and technology center (ESTEC) located in Noordwijk, The Netherlands.

2 RIDGE WAVEGUIDE

Ridge waveguide is a particular type of waveguide either rectangular or circular, in which a ridge septum is inserted. The presence of the ridge has many implication on the reduction of the cutoff frequency, lowered impedance, and wide bandwidth free from high-mode interference if compared with rectangular waveguide of identical inner dimensions. One of the first study of ridge waveguide was presented in [8] and afterwards investigated in [20].

2.1 GEOMETRY

This work is focused on the rectangular ridged waveguide and even if there are some applications where the circular ridged configuration may be of interests for some applications [35], in the following only rectangular shape will be discussed. The two most common geometries of ridge waveguide are depicted in Fig. 1:

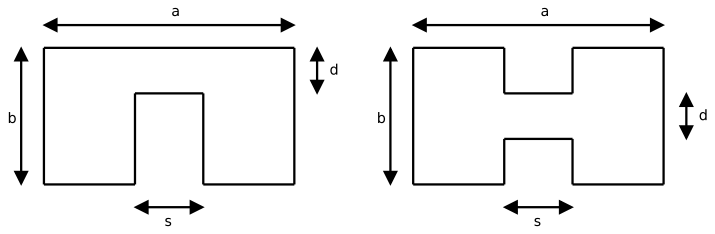

(a) Single ridge **(b)** Double ridge

Figure 1: Cross section of single and double ridge

Main parameters of this geometries are:

- a width inner dimension of the waveguide
- b height of the waveguide
- s width of the ridge
- d gap of ridge

For the single ridge the d dimension is the gap between ridge and external enclosure while in the double configuration is the gap between the two ridges. The distribution of the electric field of the dominant mode in this type of waveguides is shown in

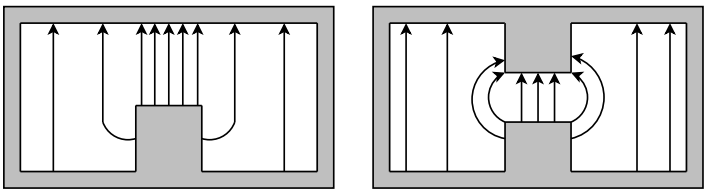

(a) Single ridge **(b)** Double ridge

Figure 2: Electric fields in single and double ridge waveguides

Fig. 2. The gap is the causes of a strong E field in it and therefore an accumulation of charges between the two sides of the gap, therefore it can be modellized by the presence of the two capacitors like in Fig. 3 and characteristic admittance Y_{02} in the gap area and Y_{01} outside the gap.

2.2 CUTOFF FREQUENCIES

By applying the transverse resonance method (TRM) to the equivalent circuit of Fig. 3 it is possible to derive the equations [17] for the cutoff frequency of the TE_{n0} modes:

$$\cot(k_x l) - \frac{b}{d}\tan\left(k_x \frac{s}{2}\right) - \frac{B}{Y_{01}} = 0 \tag{2.1}$$

$$\cot(k_x l) + \frac{b}{d}\tan\left(k_x \frac{s}{2}\right) - \frac{B}{Y_{01}} = 0 \tag{2.2}$$

where $l = (a - s)/2$ and k_x is the propagation constant in the x direction at cutoff and is given by

$$k_x = \frac{2\pi}{\lambda_c} \tag{2.3}$$

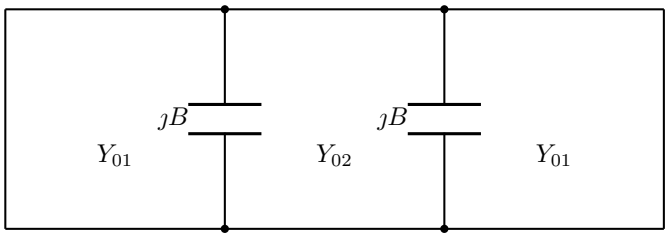

Figure 3: Equivalent circuit for a rectangular ridge waveguide

Equation (2.1) refers to the TE_{n0} with n odd while eqs. (2.2) applies to the even TE_{n0} modes. The characteristic admittances Y_{01} and Y_{02} are defined as

$$Y_{01} = \frac{k_x}{\omega\mu}\frac{1}{b} \tag{2.4}$$

$$Y_{02} = \frac{k_x}{\omega\mu}\frac{1}{d} \tag{2.5}$$

The value of the normalized susceptance term B/Y_{01}, which represents the effect of the step discontinuity, is taken from published data in the *Waveguide Handbook* [23] and can be calculated for both single and double ridge with the formulas (2.6) and (2.7):

$$\frac{B}{Y_{01}} \approx 4\left(\frac{a}{\lambda_c}\right)\frac{b}{a}\ln\csc\frac{\pi d}{2b} \qquad \text{single ridge} \tag{2.6}$$

$$\frac{B}{Y_{01}} \approx 2\left(\frac{a}{\lambda_c}\right)\frac{b}{a}\ln\csc\frac{\pi d}{2b} \qquad \text{double ridge} \tag{2.7}$$

In [19] it is shown that parameters of single ridge can be evaluated starting from the double ridge geometry taking only an half of its equivavent circuit. This is the reason why in the formulas of the normalized susceptance there is a factor of 2 between the two definitions. A scrutiny of this arrangement indicates that the two capacitors formed in this way are in series due to the fact the top and bottom ridges are at different potential in order to support the electric field. The normalized capacitance of the single ridge with the nomenclature used to label the details of the waveguide is therefore twice that of the double one as asserted.

Solving the non-linear equation (2.1) is it possible to obtain the cut-off wavelength for the dominant mode TE_{10}; Fig. 4 illustrates the cut-off space of a single ridge structure.

In [20] are presented graphs and curves for both double ridge that can be applied directly to single one with identical s/a and d/b ratios, but with an aspect ratio b/a which is one half that of the double ridge. Since the electrical properties depend to variuos degree upon the ratio b/a, its a common opinion that an aspect ratio $b/a = 0.25$ is not very favorable for the single ridge guide, so was found the expedient value of $b/a = 0.45$. All the data related to single ridge proposed in the paper and in this work, derive from waveguides of an aspect ratio of 0.45. For those waveguides with different ratios b/a is possible or to use an *extension factor* or to use data of [29]. Curves has been parametrized with ratios s/a and d/b in order to be entirely indipentent from particular dimensions. To be notice that in

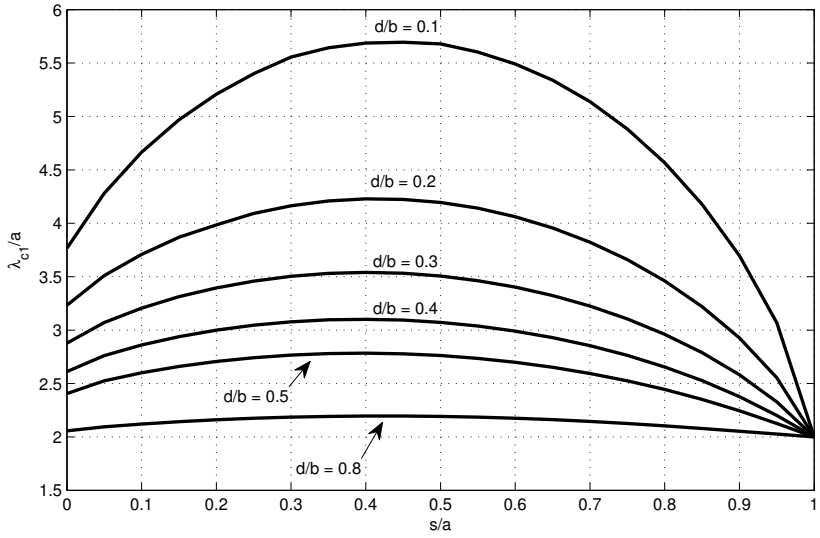

Figure 4: Cutoff curves for the TE_{10} in a single ridge waveguide with aspect ratio $b/a = 0.45$

Fig. 4 the cut-off wavelengths λ_c are normalized respect of the width of the guide. In a traditional *rectangular waveguide* the cut-off wavelength of the fundamental mode is given by the well known formula

$$\frac{\lambda_c}{a} = 2 \tag{2.8}$$

so its immediate to notice from Fig. 4 that the presence of the ridge brings to a *lowering* of the cut-off frequency.

The cut-off wavelength of the TE_{20} mode is depicted in Fig. 5 for different s/a and d/b ratios.

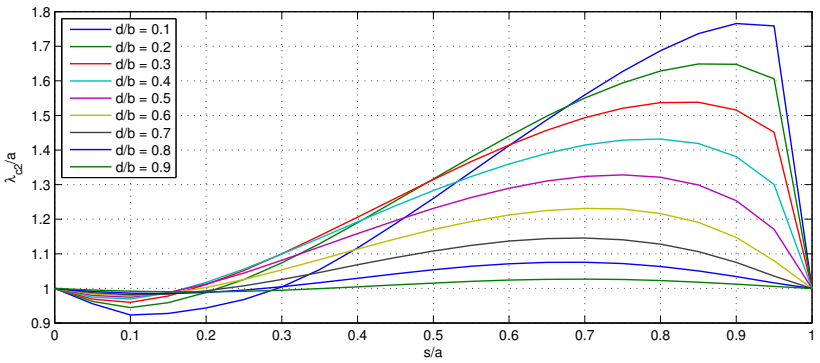

Figure 5: Cutoff curves for the TE_{20} in a single ridge waveguide with aspect ratio $b/a = 0.45$

2.3 BANDWIDTH CONSIDERATIONS

With the term *bandwidth*, as used here, is defined the ratio of the cutoff wavelengths of the fundamental mode and the next higher mode. For the ridge waveguide it means the ratio between the cutoff wavelength of the TE_{10} and the cutoff wavelength of the TE_{20}.

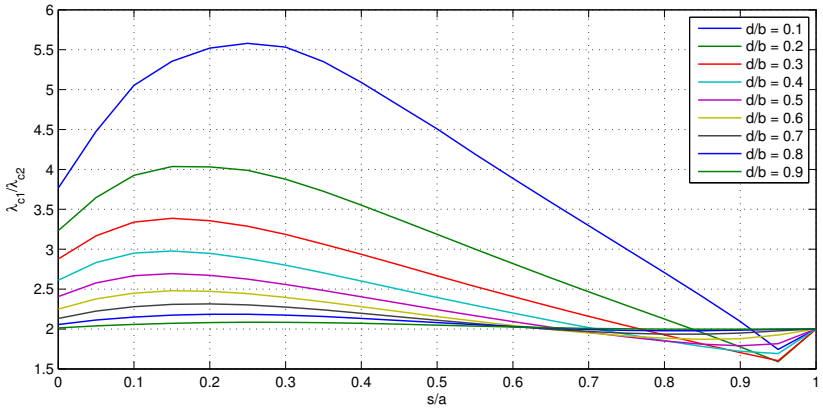

Figure 6: Ridge bandwidth

Looking at the graph in Fig. 6 can be observed that with properly adjusting the dimensions is possible to reach the desired separation between the fundamental and first higher mode. This separation can be very large (ie. more than 5 times f_{c1}). It has been proved that cut-off frequency of the third mode TE_{30} is always greater than that of TE_{20}. In this way Fig. 6 gives the space of frequencies where is satisfied the single mode propagation condition. On other hand, cutoff calculation of the TE_{01} mode show that the cutoff wavelength for this mode is very nearly equal to 2b. In order to extend the upper bandwidth limit of the ridge waveguide, to the TE_{20} mode cutoff, the b/a ratio should approximately be made equal to one-half the extension factor of the TE_{20}. For large bandwidths, this would require the b/a ratio to be about 0.4 for the double ridge and 0.45 for the single ridge. It should realized that with the term *bandwidth* as defined here is not the *useful bandwidth* over which the waveguide may be operated. The latter depends mainly upon how close to the lower cutoff frequency one is willing to work. Experience has shown that this may be 15% above cutoff.

2.4 ATTENUATION AND POWER FLOW

Has discussed in [20], is convenient to present ridge attenuation data making a comparison with a rectangular waveguide of same cutoff frequency.

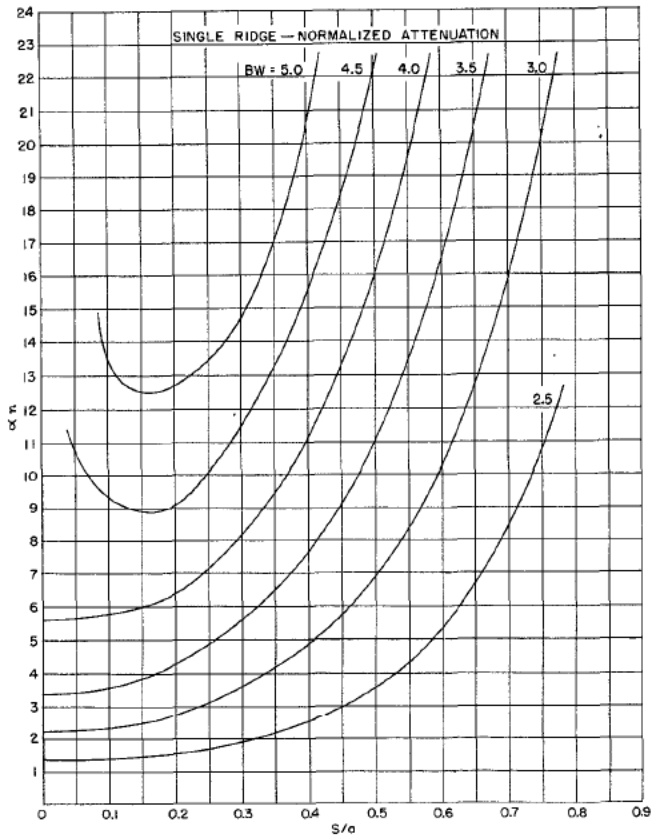

Figure 7: Single ridge attenuation normalized to the attenuation of a rectangular waveguide of same cutoff.

In Fig. 7 the attenuation of a single ridge waveguide has been calculated for different dimensions s/a and bandwidths, and it has been normalized to the attenuation of a rectangular waveguide that has the same cutoff frequency. Thus in the last picture the value of the normalized attenuation α_n is given by:

$$\alpha_n = \frac{\alpha_{\text{ridge}}}{\alpha_{\text{rectangular WG}}} \tag{2.9}$$

By a first view of the graph is immediate to notice that for large bandwidths the value of attenuation can be, for example, more than 10 times the attenuation of the rectangular waveguide.

The power flow in the waveguide at finite frequency may be related to one at infinite frequency with the relation

$$P_t(\omega) = P_t(\infty)\left(\frac{\lambda}{\lambda_g}\right)^2 \tag{2.10}$$

and

$$P_t(\infty) = \frac{E_0^2 d}{2\pi\eta_0}\left\{\frac{2md}{\lambda_c}\ln\csc\left(\frac{\pi d}{2b}\right)\cos^2(\theta_2) + \frac{\theta_2}{2} + \right.$$
$$\left. + \frac{\sin(2\theta_2)}{4} + \frac{d}{b}\left(\frac{\cos\theta_2}{\sin\theta_1}\right)^2\left[\frac{\theta_1}{2} - \frac{\sin(2\theta_1)}{4}\right]\right\}\lambda_c \tag{2.11}$$

To cater for the lumped element susceptances of single and double ridge waveguides, m takes the value

$$m := \begin{cases} 1 & \text{for double ridge} \\ 2 & \text{for single ridge} \end{cases}$$

E_0 is the peak electric field intensity (V/m) at the centre of the waveguide:

$$E_0 = \frac{V_0}{d} \tag{2.12}$$

Variables θ_1 and θ_2 are the electrical lengths respectively outsite and inside the gap of the equivalent circuit of Fig. 3 with a magnetic wall in the middle [7]:

$$\theta_1 = \frac{\pi(a-s)}{\lambda_c} \tag{2.13}$$

$$\theta_2 = \frac{\pi s}{\lambda_c} \tag{2.14}$$

In the particular case of

$$\begin{cases} s = a \\ d = b \\ \theta_1 = 0 \\ \theta_2 = \pi/2 \end{cases}$$

$P(\omega)$ reduces to the result of an ordinary rectangular waveguide.

Quantity α is expressed in unit per length and if it is sufficently small, the time average power P_t transmitted through the waveguide may be rewritten approximately as

$$P_t \to P_t \exp(-2\alpha z) \tag{2.15}$$

The power loss per unit length P_l is then given by:

$$P_l = -\frac{\partial P_t}{\partial z} = 2\alpha z P_t \tag{2.16}$$

The attenuation per unit length is therefore described by

$$\alpha = \frac{P_l}{2P_t} \tag{2.17}$$

in which P_l may be determined as the dissipation in each wall of the waveguide:

$$P_l = \frac{1}{2} Z_s \int_A |J|^2 dA \tag{2.18}$$

where Z_s is the skin resistance of the metal enclosure:

$$Z_s = \sqrt{\frac{\omega \mu_0}{2\sigma}} \tag{2.19}$$

J is the current density and σ is the resitivity of the waveguide wall. In this way with the previous formulas (2.17) (2.10) (2.18) is it possible to calculate both attenuation for ridge and rectangular waveguide, making able the drawing of Fig. 7.

2.5 RIDGE IMPEDANCE

Is well known from the theory of the electromagnetic fields that in a transmission line where are propagating transverse electric (TE) or transverse magnetic (TM) modes there are not a unique definition characteristic impedance like in the transverse electromagnetic (TEM) lines. The main property of ridge waveguides is that the impedance (or the admittance) at finite frequency is related to one at infinite frequency by the following relation:

$$Z_0(\omega) = Z_0(\infty) \left(\frac{\lambda_g}{\lambda_0} \right) \tag{2.20}$$

The calculation of impedance at infinite frequency relies on the fact that the field distributions at cutoff frequency and at infinite frequency are identical. At $f = \infty$ the wave impedance is that of free space. Hence, if the E field is known, the H field is give by

$$H_x = \frac{E_y}{120\pi}$$

Both E and H are completely transverse at $f = \infty$ and the current at top and the bottom of the waveguide is completely longitudinal. Knowledge of distribution of E_y either at cutoff or at infinite frequency is sufficient to solve this problem. Depending on application and desired behavior of the microwave circuit, the designer can use one of the following definitions of impedance (or admittance):

1. power to voltage definition (see 2.5.1);
2. voltage to current definition (see 2.5.2);
3. power to current definition (see 2.5.3).

2.5.1 Power Voltage definition

Power to voltage definitio is very useful, for example, when is necessary to design transitions between ridge waveguide and another different type of waveguide (ie. coaxial or rectangular waveguide). In this case a useful definition of impedance is like the following:

$$Z_{PV}(\infty) = \frac{V_0^2(\infty)}{2P_t(\infty)} \tag{2.21}$$

where $V_0(\infty)$ is the peak voltage across the centre of the ridge at infinite frequency and $P_t(\infty)$ is the average power carried by the guide as defined in (2.11). $Z_{PV}(\infty)$ is plotted in Fig. 8.

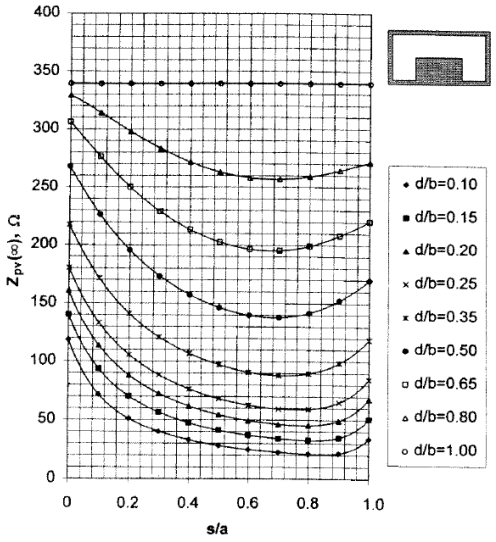

Figure 8: Power-voltage values of impedance at infinite frequency for single ridge.

2.5.2 Voltage Current definition

A first definition of $Z_{VI}(\infty)$ was given by [8] as the ratio of voltage across the centre of the guide to the total longitudinal current on top of face:

$$Z_{VI}(\infty) = \frac{V_0}{I} = \frac{120\pi d E_0}{2\int_0^{a/2} E dx} \tag{2.22}$$

This definition does not considers the step discontinuity at either side of ridge, so it has been corrected like explained in [26]. Values of Z_{VI} are presented in Fig. 9.

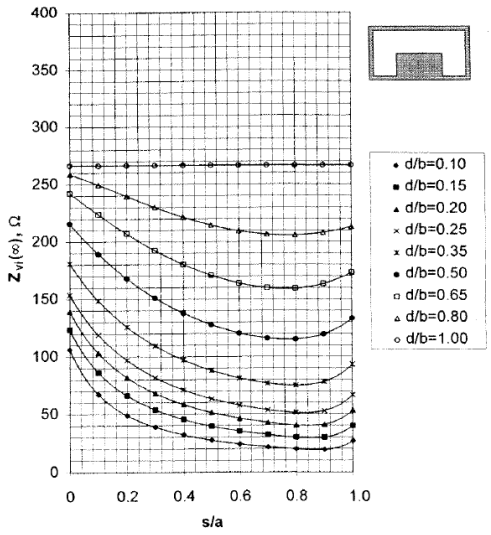

Figure 9: Voltage-current values of impedance at infinite frequency for single ridge.

2.5.3 Power Current definition

Once the values of $Z_{PV}(\infty)$ and $Z_{VI}(\infty)$ have been already calculated, it is possible to derive the plot of $Z_{PI}(\infty)$ using the following relation:

$$Z_{PI}(\infty) = \frac{Z_{VI}^2(\infty)}{Z_{PI}(\infty)} \tag{2.23}$$

Solving (2.23) is possible to make the graph of Fig. 10.

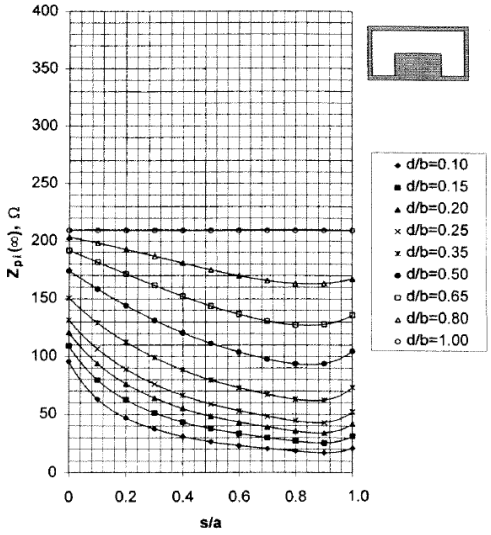

Figure 10: Power-current values of impedance at infinite frequency for single ridge.

2.6 RIDGE TRANSFORMERS

The great broadband property of the ridge waveguide derived from the great spacing between the cutoff of the fundamental mode and the cutoff of the first higher mode, is the reason why these type of waveguides are largely employed in many applications. However, in order to permit interoperability with the rest of the system, a network that matches the impedance of the ridge to one of a rectangular waveguide or a coaxial cable may be required.

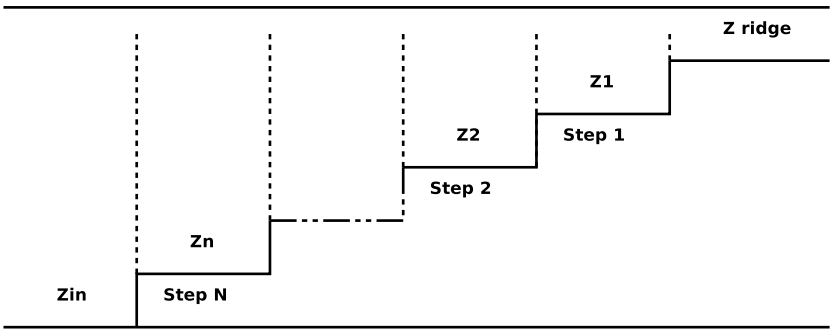

Figure 11: Scheme of single ridge transformer. Here the Z_{in} represents the empedance of the rectangular or coaxial transmission line, while Z_k are the impedances of each step.

While tapered ridge could be used for this puropose, it is more efficient and probably less costly to employ several quarter-wave

ridges sections. One possible solution is first to calculate the number of required steps depending on the specifications of desired voltage standing wave ratio (VSWR), then to calculate the values of impedance of each step with the classical theory [9] of Tchebycheff polinomials. Once the number and the values of impedance of each ridged step have been calculated, it is possible to use graphs 8, 9 or 10 in order to get final dimensions. Nevertheless, the theory underlying the transformer design is based on many semplifying assumptions, which make difficult to predict the exactly the value of desired VSWR. For this reason an optimization of overall the transformer is often required.

An example of design of a double ridge stepped transformer may be found in [18].

3 DIMENSIONAL SYNTHESIS

3.1 FILTER STRUCTURE

In this chapter we are going to present the dimensional synthesis method that has been used for obtaining the final physical lengths of the filter. The filter studied was composed by transmission lines resonators and rectangular evanescent couplings: resonators are piece of single ridge waveguide and K inverters are obtained with piece of rectangular waveguides of the same dimension of ridge cross-section, ad consequently operating below cut-off. One target of this project is also to build a filter of this type, so particular attention was paid for practical problems related to the manifacturing process. First of all the cross-section of the ridge waveguide is chosen to be the same for all resonators and both input and output waveguide port. The dimensions of the evanescent couplings are also chosen all equal and moreover identical to ridge external enclosure.

The top view structure for a *single* ridge waveguide filter is depicted in Fig. 12: from this figure its possible to see that all ridge resonators have the same width and they are coupled each other with an empty waveguide. In the present treatment longitudinal dimension of ridge resonators will be indicated with l_{r1}, l_{r2}, l_{r3},..., l_{rN}, where N is the order of the filter, like the dimensions of the couplings with l_{c1}, l_{c2},..., l_{cN}, l_{cN+1} as it is shown in Fig. 13. The length of the input/output waveguide has no impact on the performance of the filter. The transverse parameters are those indicated in Fig. 1 and for this work a single ridge is chosen. Practical considerations made the choice for the single ridge despite of the double: first of all single ridge has

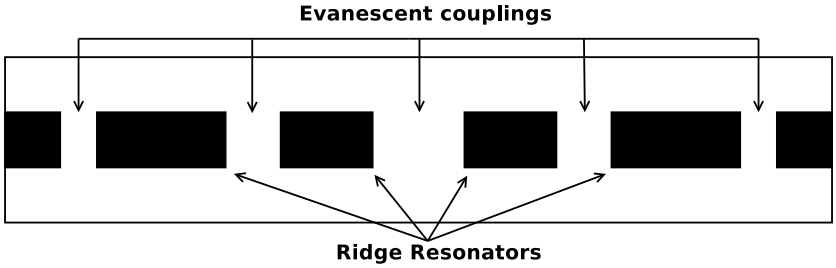

Figure 12: Top view layout

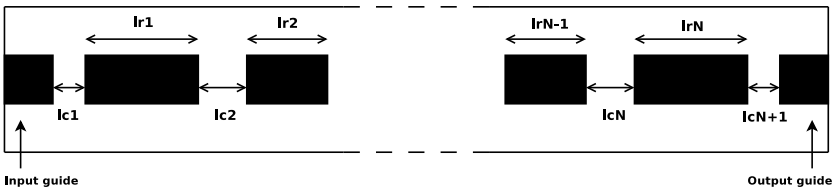

Figure 13: Filter dimensions legenda. In this top view of the filter is possible to understand the meaning of filter's parameters.

less impact to the manifacturing tolerance to the gap (or the d dimension), furthermore the double ridge has the disadvantage of the impossibility of inserting tuning screws. The convenience of having the same cross-section dimensions for both ridges and evanescent couplings is that a uniform rectangular sketch can be closed on top by a *lid*.

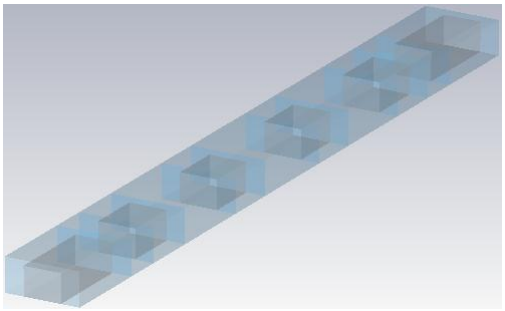

Figure 14: Four poles single ridge waveguide filter. The first and the last piece of ridge are the input and the output waveguide.

3.2 RIDGE RESONATOR

Fig. 14 shows clearly the use of ridge waveguides as resonators. An *eigenmode* analysis was performed with the electromagnetic (EM) simulator with electric walls as boundary conditions. The fundamental mode of ridge waveguide is the TE_{10} and like the rectangular waveguide, and the length of a resonating ridge cavity is exactly $\lambda_g/2$. In reality the length of each resonator must be changed to correct the effect of the coupling discontinuity. In a prototype filter of half-wavelength resonators and *K-inverters* each resonator has to see a shorted circuit at both ends and theoretically it has an electrical length of π.

The ideal situation is depicted in Fig. 15 in which a ridge is closed by perfect electric conductor (PEC) shows that the maximum of the electric field is placed exactly at the centre of ridge.

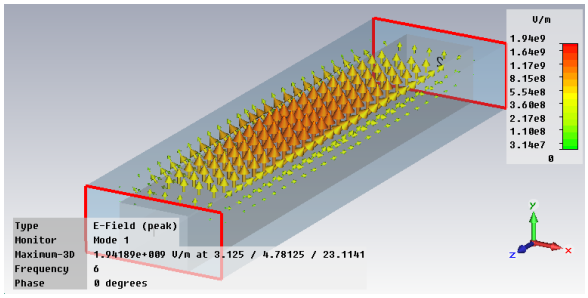

Figure 15: Resonant ridge cavity closed by PEC.

Transverse dimensions in millimiters of Fig. 15 are: $a = 12.5$, $b = 5.625$, $s = 6.25$, $d = 0.84375$, and the longitudinal length is $l = 46.2283$ millimiters. The cut-off frequency is $f_0 = 5.053\,\text{GHz}$ and the wavelength in the waveguide is $\lambda_g = 92.4566$ millimiters.

3.3 EVANESCENT COUPLINGS

Dimensions of the ridge enclosure and empty waveguide coupling are setted the same. By this way cut-off frequency of the rectangular trait is necessarily higher. If we put the operative bandwidth in a range of frequencies in which they are up the cut-off of ridge and below the one of rectangular waveguide, we are talking abount *evanescent* couplings. Others useful articles on evanescent discontinuity are [11, 36, 40].

A piece of waveguide below cutoff closed on two ridge waveguides is propagation, realizes an inverter that is used in the filter.

In Fig. 16a is depicted an evanescent waveguide which acts as inverter. Its length is variable $l_I^{i,i+1}$ where the subscript I means that this is the inverter physical structure of the filter. In a cascading of inverters and resonators is common to indicate each with the letter i the i-th resonator and the inverter between two resonators i and $i+1$ with $K_{i,i+1}$. When loaded with two ridges, evanescent waveguide behaves like the inverter circuit of Fig. 16b. The discontinuity effects caused by the rectangular waveguide are modellized as two negative transmission lines $\Delta l_{i,i-1}$ and $\Delta l_{i,i+1}$ which corrects the lengths of adjacent ridge resonators. Length of evanescent waveguide is a function of its relative K inverter, and once this dimension is fixed is directly obtained the values of $\Delta l_{i,i+1}$ and $\Delta l_{i,i-1}$

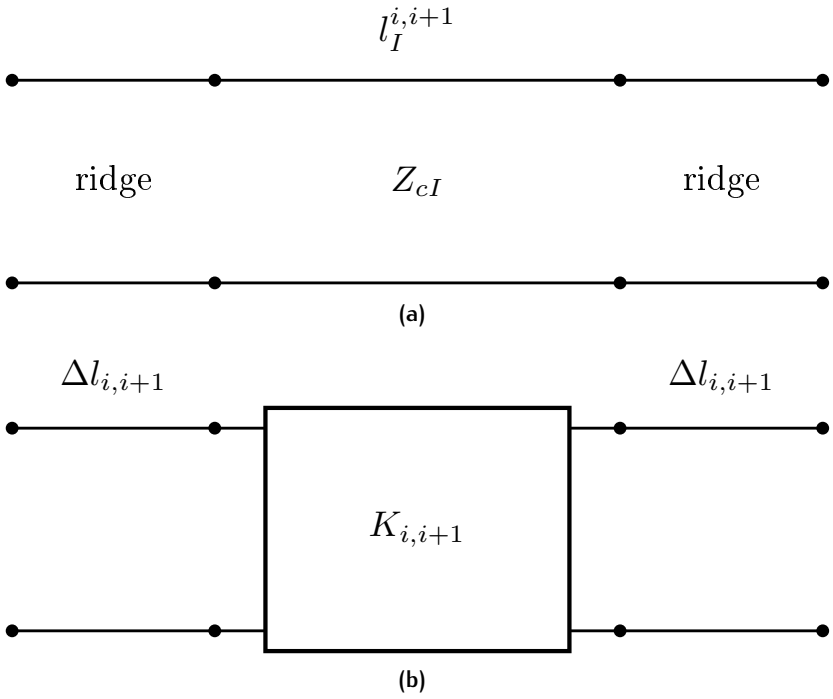

Figure 16: Equivalent circuit of an evanescent waveguide

3.4 FULL-WAVE APPROACH

Although ridge waveguide filters are commonly employed in many telecommunication, terrestrial and space applications, the synthesis procedure that starting from specifications brings to final dimensions consists in a two-step [28] method where the approximated lengths are then optimized by simulations software.

This approach was extensively used in the past and important studies on evanescent mode and structure [12–14] can provide many formulas to get initial dimensions band-pass filters. However the problem of ridge waveguide filters with below cut-off couplings is relatively complicated and analitical closed formulation are not always possible to derive. Depending on the accuracy of the model used for describing the problem, the derived formulas can be more or less accurate. Anyway, they remain good approximations and a next optimization is required. The process of synthesis is summarized in Fig. 17. The results that are possible to obtain after the optimization process depends by how much is sophisticated the simulation tool, by the number of parameters involved in the optimization and by the computational power that can be provided. Time and resources necessary for the optimization step must be considered carefully

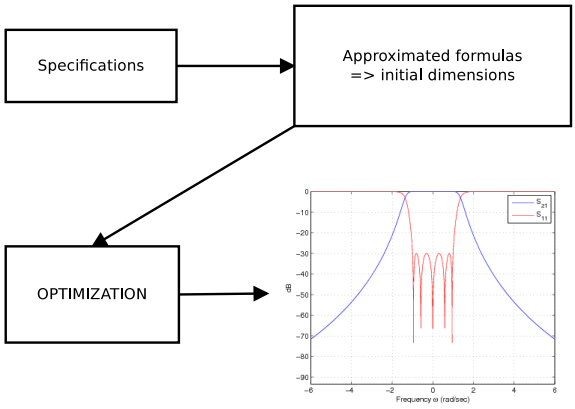

Figure 17: With approximated formulas is necessary an EM optimization in order to get desired response.

because they can have a non trascurable impact in budgets and final deadlines.

In a different way synthesis presented in these work is based in a full wave approach with the help of an EM simulator. This technique was succesfully developed in [41] for getting directly the final dimensions for inductive irises waveguide band-pass filters and diplexers.

3.5 DESIGN PROCEDURE

Synthesis procedure here used, that permits to obtain directly final dimensions starting from specifications, can be summarized by the follwing steps:

1. design of ridge cross section,
2. synthesis of filter structure.

Ridge cross section defines the propagating properties of the ridge waveguide and moreover the propagating features of the filter's resonators. The model here used is composed by ridge waveguides of the same cross section and constant gaps alternately connected to constant cross section rectangular waveguide portions. In addition, evanescent rectangular waveguide has the same cross section as the ridge waveguide. An extension to the generalized case (i.e. cross sections of evanescent and ridge waveguide not necessarily the same) is possible though additional design, manufacturing and tuning efforts are not justified in most of applications. Note that the impedance transformer section is not addressed here, being not relevant to the

synthesis procedure presented. In the scenario under consideration, the following points must be outlined:

- all rectangular waveguide sections have same cut-off frequency and are evanescent
- all ridge waveguide sections have same cut-off frequency and are in propagation.

Constant cross section evanescent rectangular waveguide operating below its fundamental mode cutoff frequency realizes an impedance inverter, while constant gap ridge waveguide sections realize series half-wave resonators between the impedance inverters. The TE_{10} cut off of the ridge waveguide determines the length ratio of the ridge waveguide to the evanescent waveguide. When the cutoff frequency is close to the filter band, the resonance is essentially confinated in the resonator and the ridge waveguide length is larger than the evanescent waveguide length. In this case the filter operates more like a direct-coupled cavity filter with the evanescent waveguide as the coupling element. If the cutoff frequency is shifted lower from the filter band ($f_c \ll f_0$), the resonance is distributed both in the resonator and in the evanescent coupling, leading to a decrease of the ridge waveguide length and to an increase the evanescent waveguide length. Finally, when the cutoff frequency is very far from the filter band, the evanescent waveguide length is much larger than the ridge waveguide length. When the resonator length is small (say, $< \lambda_g/10$), the filter behaves as a microwave analog of lumped inductance filters with series inductance coupling, the magnitude of the series inductance being controlled by the separation between capacitive obstacles. The equivalent circuit of a small post (acting as an obstacle) in cutoff waveguide is not necessarily the same as one the one that applies in the propagating case. The lumped circuit concept is a powerful tool because many established lumped circuit configurations could be realized directly in corresponding equivalent waveguide circuits, providing a great deal of flexibility according to different design cases.

3.5.1 Design of Ridge Cross Section

Cross-section dimensions of ridge waveguide (Fig. 1) must be first identified according to specifications such as fundamental mode cut-off frequency, location of higher order modes, power-handling considerations, envelope requirements and technology constrains. The geometry of ridge section also affects the waveg-

uide characteristic impedance and eventually the filter matching network. It is well known [20] that if $a \gg d$ the characteristic impedance is linearly proportional to d, while showing negligible dependence on b and s dimensions. Therefore, the ridge section must be selected considering the impedance mismatch generated between filter section and I/O waveguide interface. A significant mismatch may require a high-order and bulky impedance transformer.

Using Graphs and data of chapter 2 the dimensions of the ridge cross section can be found in accordance with the specifications. The ridge waveguide design procedure is performed making use of a simple numerical code or existing design curves and is summarized in the following steps:

1. Review of key RF requirements: insertion loss, out-of-band rejection, power handling.

2. Definition of ridge waveguide geometry, evaluating preliminary a, b, s and d dimensions. Initially, s and d are selected on the basis of technology considerations. Then a proper combination of a, b values is chosen according to ridge waveguide TE_{20} mode cut-off frequency. This mode is always the second higher order mode and shall be located beyond the highest specified frequency point for the out of band rejection. Furthermore, the designer must ensure that rectangular waveguide section (in our case directly fixed when choosing a and b) is operating below cut-off within the specified filter frequency range.

3. Evaluation of optimum d value according to desired ridge waveguide TE_{10} cut-off frequency and bandwidth with the help of graphs 4 and 6 . Decreasing the ridge gap height d can considerably improve the filter spurious response and reduce envelope length. However, since the ridge gap height cannot be too small due to Q (quality factor), power handling requirement and manufacturing difficulty, the filter spurious response improvement and length reduction are limited.

4. Calculation of ridge waveguide characteristic impedance and evaluation of impedance matching requirements.

This part of the synthesis is particular sensitive because it describes the properties of the filter in term of insertion loss, power capability, out of band response and cutoff of the waveguide. All these parameters are given by the specifications and is a task for

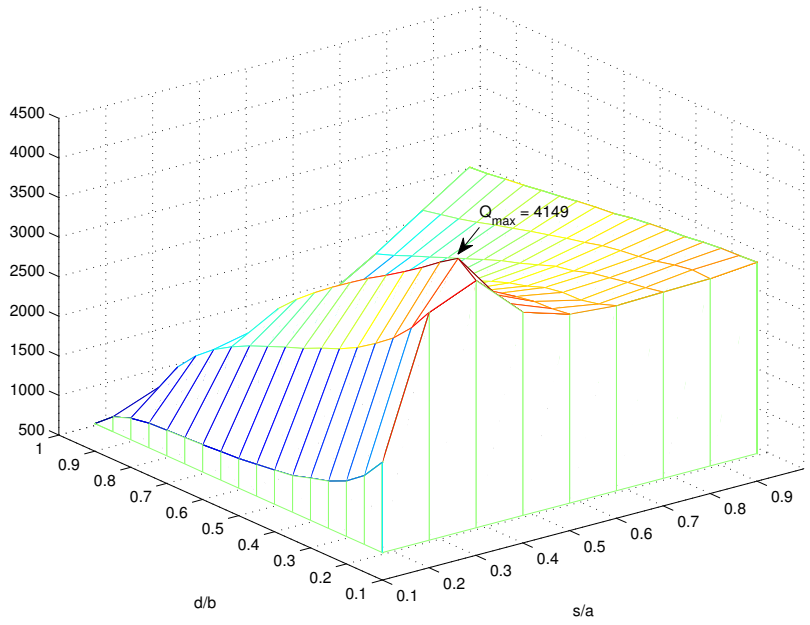

Figure 18: Value of quality factor by varying ridge dimensions with silver material. There is a maximum value corresponding to $s/a = 0.3$ and $d/b = 0.2$

the designer to find the correct compromise between all the variables. Particular attention was paid to the impact of the Q factor. Since the quality factor is inversely proportional to the attention of the waveguide

$$Q \propto \frac{1}{\alpha}$$

once fixed the cutoff frequencies of the fundamental and the first higher mode (in chapter 2 this quantity was defined as *bandwidth of the waveguide*) it is possible to change the dimension of s in order to obtain the optimum Q. An useful approach is to study the impact of the dimensions of the waveguide on the Q. If we refer to the ridge resonant cavity of Fig. 15 a 3D plot of the quality factor for silver is shown in Fig. 18. That figure demonstrate that there is an optimum value that is obtained for $s/a = 0.3$ and $d/b = 0.2$ ratios. When fixing the transverse dimensions the value of the Q is a variable that must be taken into account but it is not the only one to be considered. Usually, dimensions related to the optimum value of Q of Fig. 18 do not meet other specifications like the out of band or the cutoff frequency. If we use the aluminum in place of Silver, we obtain the same figure but scaled down. The maximum in this last case is located at the same $s/a = 0.3$ and $d/b = 0.2$ but its value is $Q_{max} = 3213$.

Upon completion of these steps the filter cross sections are fully determined and require no further changes.

3.5.2 Direct Synthesis of Filter Section

Once the cross section has been fixed, the only dimensions to be evaluated are the lengths of both ridge resonators and evanescent couplings. In literature there are a lot of examples of ridge waveguide filters obtained by first calculating approximated lengths and then performing an overall optimization. Here a direct synthesis that brings directly to the final dimensions without further optimization is proposed.

Prototype filter here used is a sequence of half-wavelength resonators with K inverters as shown in Fig. 19a. The inverters are normalized to the impedance of the propagating transmission lines. By replacing the theoretical inverters with the evanescent couplings, the equivalent circuit of the lines below the cut-off must be used. Fig. 19b shows the filter with the equivalent circuit of the evanescent couplings. Every ridge resonator that nominally is half-wavelength, is corrected by terms $\Delta l_{i,i+1}$ for the presence of the empty waveguide discontinuity. In order to have an equivalence between Figs. 19a and 19b the following equation must be verified:

$$l_R^i + \Delta l_{i-1,i} + \Delta l_{i,i+1} = \frac{\lambda_g}{2} \tag{3.1}$$

Final circuit that will be implemented is depicted in Fig. 19c where evanescent couplings of length $l_I^{i,i+1}$ and characteristic impedance Z_{cI} normalized to the impedance of the propagating ridge, are connected with propagating ridge resonators of length l_R^i. In this discussion all resonators are considered equal and having a slope parameter of:

$$\frac{X_{eq}}{Z_0} = \frac{\pi}{2}\left(\frac{\lambda_g}{\lambda_0}\right)^2 \tag{3.2}$$

Moreover the theoretical values of K inverters can be evaluated by the traditional formulas:

$$K_{0,1} = \sqrt{\frac{Z_0 X_{eq} w}{g_0 g_1 \omega_1'}} \tag{3.3a}$$

$$K_{i,i+1} = \frac{w}{\omega_1'}\frac{X_{eq}}{\sqrt{g_i g_{i+1}}} \tag{3.3b}$$

$$K_{N,N+1} = \sqrt{\frac{Z_0 X_{eq} w}{\omega_1' g_N g_{N+1}}} \tag{3.3c}$$

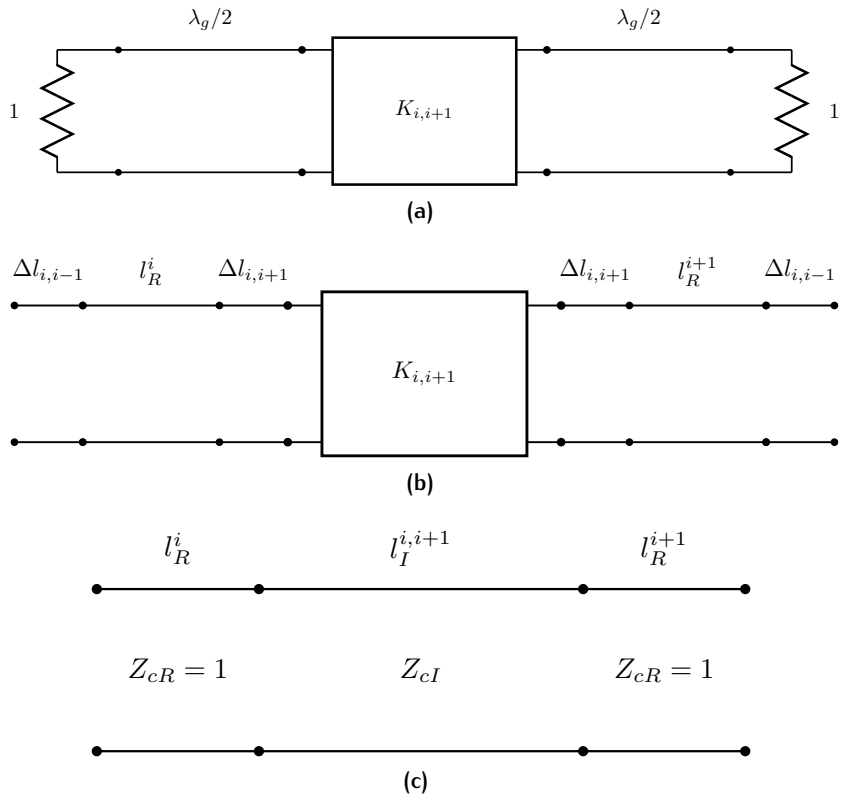

Figure 19: Models of ridge coupled resonators

The scattering matrix of an inverter may be calculated by using network transformation formulas [22], and is possible to relate the values of K inverter parameters, terminated in impedances Z_0 on each side, to their scattering parameters using formulas:

$$\begin{cases} S_{11} = \dfrac{jK - \frac{j}{K}Z_0^2}{jK + \frac{j}{K}Z_0^2} \\ S_{21} = \dfrac{2Z_0}{jK + \frac{j}{K}Z_0^2} \end{cases} \tag{3.4}$$

and for admittance inverter:

$$\begin{cases} S_{11} = \dfrac{\frac{j}{J} - jJZ_0^2}{\frac{j}{J} + jJZ_0^2} \\ S_{21} = \dfrac{2Z_0}{\frac{j}{J} + jJZ_0^2} \end{cases} \tag{3.5}$$

The frequency response of the evanescent couplings can be related directly to the theoretical value of K inverters using the formula

$$|S_{21_{i,i+1}}| = \frac{2Z_0}{K_{i,i+1} + \frac{1}{K_{i,i+1}} Z_0^2} \tag{3.6}$$

Knowing the scattering parameter on each evanescent inverter is possible to establish their length by using electromagnetic software. Eq. (3.6) is the theoretical magnitude of S_{21} of the inverter and it is a reference value: the length of the piece of waveguide below cutoff has to be equal to scattering parameter $|S_{21}|$ calculated with eq. (3.6) for given transverse dimensions. An EM analysis is then performed and scattering parameters are calculated at the central frequency f_0. The magnitude of S_{21} is then compared with the theoretical value given by (3.6). In order to derive the correct scattering parameter, length of the evanescent waveguide is varied until its scattering parameter $|S_{21}|$ matches the theoretical one. This approach represents an optimization procedure with the advantage that the solution is always possible and occurs rapidly. With commercial EM simulators the dimension of each inverter is easily obtained by optimizing the lengths that match the correct value of $|S_{21}|$ at f_0. For the present work, the computational time needed for such optimization is in the order of few seconds. An equivalent model of the evanescent coupling here used consists of an impedance inverter connected with two negative transmission lines that are absorbed by the adjacent resonators as showed in Fig. 20. Theoretically, each res-

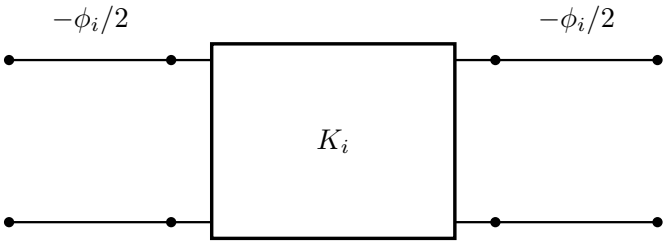

Figure 20: Model of evanescent coupling

onator sees shorted circuits at both ends and its length is $\lambda_g/2$. When the ridges are loaded with the evanescent couplings the stored energy caused by the discontinuity change the resonat frequency of the resonant and its length must be corrected. The effect of the discontinuity can be represented by the presence of an additional phase on the left and right of resonator ϕ_1 and ϕ_2. These are the negative transmission line of the model of Fig. 20

and reduce the length of resonator. Therefore, electrical length of the resonator loaded is:

$$\beta l = \pi - \frac{\phi_1}{2} - \frac{\phi_2}{2} \tag{3.7}$$

and consequently the length of resonator is

$$l = \frac{\lambda_g}{2\pi}\left(\pi - \frac{\phi_1}{2} - \frac{\phi_2}{2}\right) \tag{3.8}$$

The relationship between ϕ_i and the phase of S_{11} ($\angle S_{11}$) of the evanescent coupling is:

$$\phi_i = \pi - \Phi_i \tag{3.9}$$

where Φ_i is the $\angle S_{11}|_{\omega=\omega_0}$. In fact, if there is a shorted line, the $\angle S_{11}$ is π and ϕ is equal to zero like in the theoretical case. Therefore, the new formulation of length of resonator is:

$$l_i = \frac{\lambda_g}{2\pi}\left(\pi - \frac{\pi - \Phi_i}{2} - \frac{\pi - \Phi_{i+1}}{2}\right)$$

and by solving the last equation is possible to obtain the formula for calculating each resonator starting from the $\angle S_{11}|_{\omega=\omega_0}$:

$$l_i = \frac{\lambda_g}{4\pi}(\Phi_i + \Phi_{i+1}) \tag{3.10}$$

Using a full-wave simulator is possible to achieve easily and quickly the correct length for the couplings by using eq. (3.6) and consequently the length of the adjusted resonator by eq. (3.10) while the information of the magnitude of S_{21} and the phase of S_{11} are readily provided by most of the common commercial EM simulators.

The filter section is composed as the cascade connection of rectangular to ridge waveguide discontinuities starting with an input ridge waveguide section. The design proceeds as follows:

1. Determine the number of resonators N and the different inversion coefficient K and/or J by using Tchebycheff formulas of chapter A from filter specifications.

2. Determine initial lengths of evanescent waveguide sections to achieve the required inversion coefficients at f_0 by using analytical discontinuity characterization. The lengths of the evanescent waveguide are adjusted to achieve the desired value of the immittance inverter using formula (3.6).

Shortening evanescent waveguide length increases the coupling while lengthening evanescent waveguide length decrease the coupling. As a consequence, filter bandwidth is controlled by implementing the correct evanescent waveguide lengths.

3. Determine initial resonator length nominally half-wave. Shortening ridge waveguide length increases resonant frequency while lengthening ridge waveguide length decrease the resonant frequency. As a consequence, filter center frequency is controlled by adjusting ridge waveguide lengths. In the practical design, the rectangular to ridge waveguide discontinuity effect should be taken into account. Therefore, the nominal resonator length is shortened to subtract the waveguide discontinuity effect using formula (3.10).

At this stage of the design process filter shows the correct bandpass response, including all poles with optimized equiripple return loss.

3.6 DISPERSION OF FILTERS

Dispersion in microwave filter is a great and complex problem that derives from many factors. The most evident consequences of the dispersion on filters are the not correct bandwidth, the not equiripple return loss in band characteristic and the shift in frequency over the central frequency f_0. Normally for narrow bandwidth filters there are not this kind of problems, but for widebandwidth ($w > 5\%$ for space applications) this phenomenon must be taken into account. The reasons of dispersion are many, the most relevant are the cut-off frequency of the waveguide, the higher order modes of the filter and the dependence of frequency of the evanescent couplings. In an important papers [21] that offers a dispersed Tchebyscheff characteristic and design formulas for bandpass filters. In this work, the importance is mainly focused on the Levy's Tchebyscheff function able to describe more accurately the scattering parameters of direct coupled cavity filters including dispersion effects. The model of filter used here is composed by transmission line resonators and ideal impedance inverters. In eqs. (A.41) theory ignores the frequency variation of the shunt inductances, and in practice the K must be a function of frequency. So it is corrected by a correction factor:

$$K' = K \cdot m \tag{3.11}$$

in which m is defined:

$$m = \begin{cases} \dfrac{\omega}{\omega_0} & \text{for TEM modes,} \\ \dfrac{\lambda_{g0}}{\lambda_g} & \text{for TE or TM modes.} \end{cases} \tag{3.12}$$

where

ω is the value $2\pi f$ evaluated at generic f,
ω_0 is the central frequency $2\pi f_0$,
λ_{g0} is the wavelength in guide calculated at f_0,
λ_g is the wavelength in guide calculated at generic f.

The transfer matrix of an ideal impedance inverter

$$\begin{bmatrix} 0 & \pm jK \\ \pm\dfrac{j}{K} & 0 \end{bmatrix} \tag{3.13}$$

is then substituded with the correct factor m of (3.12):

$$\begin{bmatrix} 0 & jmK \\ \dfrac{j}{mK} & 0 \end{bmatrix} \tag{3.14}$$

In order to have an impedance inverter frequency-independent, the matrix (3.14) is splitted as the following:

$$\begin{bmatrix} \sqrt{m} & 0 \\ 0 & \dfrac{1}{\sqrt{m}} \end{bmatrix} \begin{bmatrix} 0 & jK \\ \dfrac{j}{K} & 0 \end{bmatrix} \begin{bmatrix} \dfrac{1}{\sqrt{m}} & 0 \\ 0 & \sqrt{m} \end{bmatrix} \tag{3.15}$$

The first and the third matrix of eq. (3.15) represent ideal transformers and the second matrix represents an ideal impedance inverter. Thus, the new model of impedance inverter consists of an ideal K inverter with two transformers at both ends.

Model of filter must be corrected by this theory, so the frequency dependent impedance inverter is replaced by and ideal K invert and transformers as shown in Fig. 21a. Also the model of the resonator change because the transmission line is bounded by ideal transformers with frequency dependent *turns ratio* like in Fig. 21b. It is well know that the transfer matrix of a transmission line in propagation is:

$$\begin{bmatrix} \cos\theta & jZ_0 \sin\theta \\ \dfrac{j\sin\theta}{Z_0} & \cos\theta \end{bmatrix} \tag{3.16}$$

By grouping together the matrices of a transmission line and of the transformers it is possible to define a dispersed matrix for the transmission line:

$$\begin{bmatrix} \dfrac{1}{\sqrt{m}} & 0 \\ 0 & \sqrt{m} \end{bmatrix} \begin{bmatrix} \cos\theta & jZ_0 \sin\theta \\ \dfrac{j\sin\theta}{Z_0} & \cos\theta \end{bmatrix} \begin{bmatrix} \sqrt{m} & 0 \\ 0 & \dfrac{1}{\sqrt{m}} \end{bmatrix} \tag{3.17}$$

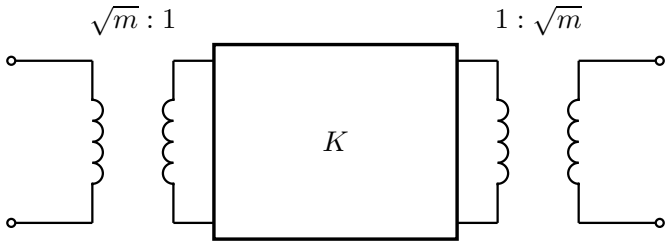

(a) Correction of impedance inverter with 2 transformers

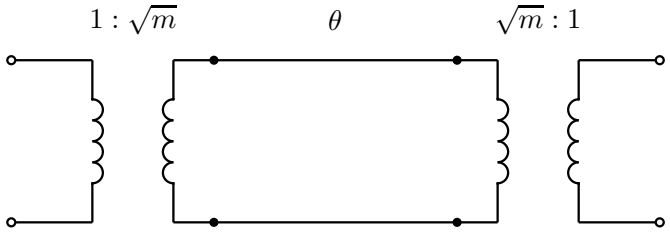

(b) Transmission line resonator is connected with transformers of adjacent inverters

Figure 21: Levy's correction

so the final transfer matrix of the transmission line added by the ideal transformers of Fig. 21b is obtained by multiplying the three matrices of (3.17) and obtaining:

$$\begin{bmatrix} \cos\theta & \jmath\dfrac{Z_0}{m}\sin\theta \\ \dfrac{\jmath}{Z_0}m\sin\theta & \cos\theta \end{bmatrix} \tag{3.18}$$

The aim is to substitute the resonator of Fig. 21b that has an electrical length of θ with a new transmission line resonator of length θ' that has the same transfer features of that of Fig. 21b. As usual, the transfer matrix of the new resonator can be expressed as:

$$\begin{bmatrix} \cos\theta' & \jmath Z_0\sin\theta' \\ \dfrac{\jmath\sin\theta'}{Z_0} & \cos\theta' \end{bmatrix} \tag{3.19}$$

The equivalent circuit associated to matrix (3.19) is that depicted in Figure 97b on page 148 in which the series reactance and the shunt susceptance where defined in eqs. (A.49) and (A.50). In that equivalent circuit the transformer indicates only the phase reversal of 180° and it can be excluded because does not affect next considerations. An equivalence between the two circuits of Fig. 22 is made so that, if close to the design frequency, the shunt

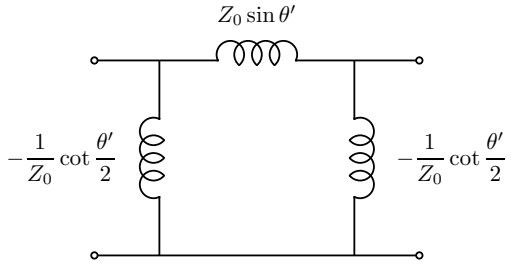

(a) Circuit of the prototype resonator

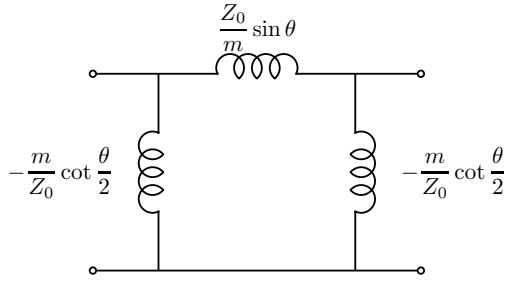

(b) Resonator correct by factor m

Figure 22: Equivalent circuits for dispersed resonators

arms of the π networks may be neglected and the following approximations is made for TE modes:

$$\sin\theta' = \frac{\sin\theta}{m} = \frac{\sin\left(\pi\dfrac{\lambda_{g0}}{\lambda_g}\right)}{\dfrac{\lambda_{g0}}{\lambda_g}} \tag{3.20}$$

because the length of resonator is nominally $l = \lambda_{g0}/2$ and the propagation constant $\beta = 2\pi/\lambda_g$. Eq. (3.20) is then introduced in the argument of the insertion loss of the Tchebycheff (A.10) in this way:

$$IL = 10\log_{10}\left\{1 + \varepsilon^2 T_N^2\left[\frac{\lambda_g}{\lambda_{g0}}\frac{\sin\left(\pi\dfrac{\lambda_{g0}}{\lambda_g}\right)}{\sin\theta'_0}\right]\right\} \tag{3.21}$$

where ε defines the ripple level and T_n is the Tchebyscheff polynomial of degree n. The new term of eq. (3.21) is giustified

because all Tchebycheff polinomials oscillate within ± 1 and the conditions at the edges ω_1 and ω_2 are the following:

$$\begin{cases} \dfrac{\lambda_{g1}}{\lambda_{g0}} \dfrac{\sin\left(\pi \dfrac{\lambda_{g0}}{\lambda_{g1}}\right)}{\sin\theta_0'} = -1 \\ \dfrac{\lambda_{g2}}{\lambda_{g0}} \dfrac{\sin\left(\pi \dfrac{\lambda_{g0}}{\lambda_{g2}}\right)}{\sin\theta_0'} = 1 \end{cases} \tag{3.22}$$

Rewriting (3.22) it follows that:

$$\sin\theta' = -\frac{\lambda_{g1}}{\lambda_{g0}} \sin\left(\pi \frac{\lambda_{g0}}{\lambda_{g1}}\right) = \frac{\lambda_{g2}}{\lambda_{g0}} \sin\left(\pi \frac{\lambda_{g0}}{\lambda_{g2}}\right) \tag{3.23}$$

In an actual specification ω_1 and ω_2 are given, so by solving the non-linear equation (3.23) is possible to find the correct central frequency ω_0 of the filter. This new frequency will be demonstrated that correct the shift of the bandpass characteristic that is common seen after the design procedure of section 3.5. When calculating the values of the K-inverters the central frequency have to be changed to that of resulting from equation (3.23).

3.7 SYNTHESIS RESULTS

In this section results of the design procedure of section 3.5 are presented. The aim of this section is to show and explain results of the synthesis procedure applied to ridge waveguide bandpass filters.

The study involves the synthesis of ridge bandpass filter of 4 poles with several bandwidths, -25 dB of in band return loss and an out of band rejection of -60 dB until the second harmonic. Two classes of ridge bandpass filters have been designed: the first at Ka-band with 20 GHz of central frequency and the second at C-band with 6 GHz of f_0. The reasons of doing the synthesis at two differents central frequencies is due essentially for practical reasons: at C-bands dimensions are greater and is easier for the machine shop the building of the filter. Nevertheless, there is a prove that this design method is independent from the central frequency.

Simulation results are good in accordance with specifications in term of in band return loss characteristic and central frequency, however the bandwidth of all the filters designed with this technique is seen enlarged by a factor $2 \div 2.4$. Taking into account

this bandwidth scaling factor results for C-band and Ka-band bandpass filters are presented.

3.7.1 Ka-band

A preliminary study of the design procedure was conducted at the Ka-band in order to confirm the expected results of the synthesis. Rules of section 3.5 have not been completely followed especially in term of the repetition of the filter. A discussion of filter at Ka-band with enhanced spurious performances is described in 3.7.2. Low insertion loss characteristics have been preferred over the stringent requirement of the propagation at $2f_0$. However, is interesting to present here these results because they are good in agreement with the specifications even though not having fully follwed the points of section 3.5, and moreover they have encouraged to continue at C-band where a more rigorous design has been applied. Specifications of the Ka-band filter are listed in table 1. Since the requirement of the out of

Table 1: Ka-band filter specifications

f_0	20 GHz
f_c	15 GHz
Filter order	4
Return Loss	25 dB

band rejection has not been considered in this preliminary study, the ratios of the ridge and consequently the absolute dimensions have been chosen in order to maximize the Q. Comparing graph

Table 2: Transverse dimensions of Ka-band ridge waveguide

a	4.8747 mm
b	2.1936 mm
s	1.2187 mm
d	0.43872 mm
b/a	0.45
s/a	0.25
d/b	0.2

of the Q factor of Fig. 18 and ratios of table 2 is observed that these values achieve both low attenuation and correct cutoff frequency of the waveguide. In order to obtain the desired Tchebycheff response with the current specifications, the parameters of the lowpass prototype filer are calculated with formulas (A.12):

$$g = \{1; 0.753308; 1.2252; 1.37121; 0.673096; 1.11917\} \qquad (3.24)$$

Table 3: Fundamental parameters of the Ka-band ridge waveguide

λ_0	14.990 mm
λ_{g0}	22.662 mm
λ_c/a	4.1
$Z_{PV}(\infty)$	75 Ω
Z_c	113.4 Ω
Y_c	0.0088192 S
$\lambda_{c1}/\lambda_{c2}$	4
X_{eq}	407.11 Ω
B_{eq}	0.031664 S

With formulas and definitions of chapters 2 and A the following essential parameters are obtained and listed in table 3. Where:

- λ_0 is the wavelength in air at f_0
- λ_{g0} is the wavelength in guide at f_0
- λ_c/a is the ratio between cutoff wavelength and width of the waveguide
- $Z_{PV}(\infty)$ is the power voltage definition of impedance at infinity frequency
- Z_c is the power-voltage characteristic impedance evaluated at f_0
- Y_c is the power-voltage characteristic admittance evaluated at f_0
- $\lambda_{c1}/\lambda_{c2}$ is the ratio of the cutoff wavelength of the fundamental and the first higher mode of the ridge waveguide
- X_{eq} is the reactance slope parameter of a transmission line cavity
- B_{eq} is the susceptance slope parameter of a transmission line cavity

These parameters are important because they will employed in the next steps of the synthesis. The wavelength λ_{g0} has been calculated at central frequency without considering the despersions explained in section 3.6. Dimensions of the rectangular waveguide evanescent couplings are the same of the envelope of the ridge, so the cutoff frequency can be calculated with the formula

$$\lambda_c = 2a$$

and for the current dimensions is listed in table 4.

Filter that will be manufactured is a symmetric structure with the same impedance waveguides connected at both I/O ports. In this way the K or J parameters are also symmetric:

$$K_{01} = K_{45} \tag{3.25a}$$
$$K_{12} = K_{34} \tag{3.25b}$$

With all the information and parameters is possible to calculate the K inverter and proceeding with the synthesis procedure. Here the objective is to see the behavior of the synthesis for the following bandwidth:

$$B = \{100\,\text{MHz}; 200\,\text{MHz}; 500\,\text{MHz}; 800\,\text{MHz}; 1\,\text{GHz};\} \tag{3.26}$$

so the values of K inverters are listed in table 5.

At this point formula (3.6) is applied and the magnitude of the scattering parameters for each evanescent coupling are calculated and listed in table 6.

Once the values of $|S_{21}|$ have been calculated it is possible to apply the direct synthesis with the help of the full wave simulator. For the present work were used *CST Microwave Studio* and *FEST* that is a simulator developed by ESA/ESTEC. A structure composed by two single ridge waveguide coupled by an evanescent coupling is simulated and the length of the empty rectangular waveguide is optimized in order to achieve the values of $|S_{21}|$ listed in table 6. It is important to notice that the reference where calculating the scattering parameters must be put at the beginning of the evanescent piece of waveguide despite of at the ridge input port. In Fig. 23 is a scheme of the top view of the coupling. The dashed lines are the reference plane where the scattering parameters have to be calculated. The full wave simulator will optimize the length of the evanescent coupling in order to obtain the desired value of $|S_{21}|$. With this method, dimensions for the evanescent couplings are listed in table 7.

Once we get the length of the empty waveguide, from the EM simulator is immediate to obtain the value of the $\angle S_{11}$. They are then evaluated at the reference plane of Fig. 23 and listed in table 8. At this point all the data needed have been obained and only the resonator lengths are missing. The last step is accomplished by the use of formula (3.10) applied to phases of S_{11}

Table 4: Cutoff of Ka-band rectangular waveguide couplings

$\lambda_{c_{\text{waveguide}}}$	9.749 mm
$f_{c_{\text{waveguide}}}$	30.75 GHz

Table 5: Values of K inverters for Ka-band filters

Bandwidth	K_{01}	K_{12}	K_{23}
100 MHz	17.5042	2.1188	1.5705
200 MHz	24.7547	4.2376	3.1409
500 MHz	39.1405	10.594	7.8523
800 MHz	49.5090	16.951	12.564
1 GHz	55.3530	21.188	15.705

Table 6: Values of $|S_{21}|$ couplings for different bandwidths in dB

Bandwidth	$\lvert S_{21_{01}}\rvert = \lvert S_{21_{45}}\rvert$	$\lvert S_{21_{12}}\rvert = \lvert S_{21_{34}}\rvert$	$\lvert S_{21_{23}}\rvert$
100 MHz	−10.4130	−28.5520	−31.1520
200 MHz	−7.6021	−22.5405	−25.1363
500 MHz	−4.1961	−14.6451	−17.2124
800 MHz	−2.6928	−10.6791	−13.1945
1 GHz	−2.0646	−8.8471	−11.3153

evaluated at central frequency of table 8 and finally listed in table 9. Filters obtained here are symmetric structures, so it is true that:

$$l_{c5} = l_{c1} \tag{3.27a}$$
$$l_{c4} = l_{c2} \tag{3.27b}$$
$$l_{r4} = l_{r1} \tag{3.27c}$$
$$l_{r3} = l_{r2} \tag{3.27d}$$
$$\Phi_5 = \Phi_1 \tag{3.27e}$$
$$\Phi_4 = \Phi_2 \tag{3.27f}$$

At this point, with dimensions of cross section of table 2 and longitudinal lengths of tables 7 and 9, the filters are fully characterized.

Table 7: Length of couplings for different bandwidths in mm at Ka-band

Bandwidth	$l_{c1} = l_{c5}$	$l_{c2} = l_{c4}$	l_{c3}
100 MHz	3.1554	7.4402	8.0517
200 MHz	2.4739	6.0256	6.6366
500 MHz	1.6114	4.1631	4.7700
800 MHz	1.1982	3.2192	3.8191
1 GHz	1.0121	2.7776	3.3714

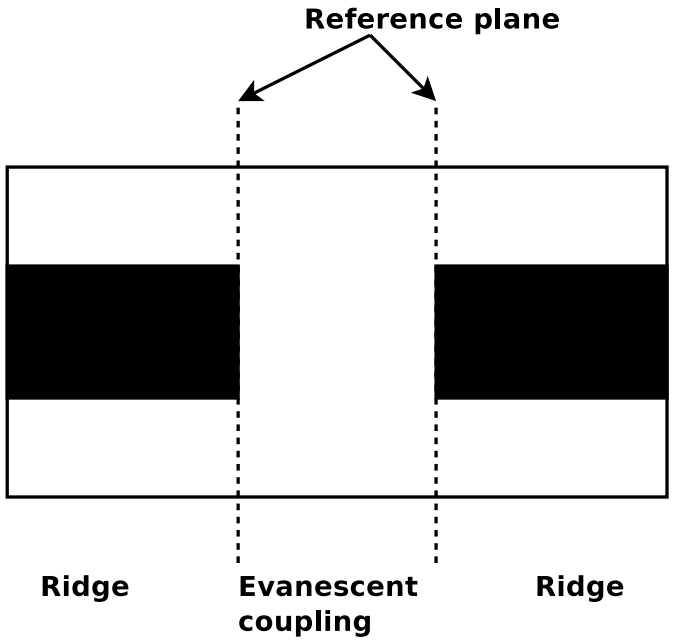

Figure 23: Top view layout of the coupling calculation

Table 8: Values of $\angle S_{11}$ for different bandwidths in degree for Ka-band

Bandwidth	$\Phi_1 = \Phi_5$	$\Phi_2 = \Phi_4$	Φ_3
100 MHz	24.03	21.16	21.14
200 MHz	26.83	21.29	21.23
500 MHz	34.64	22.20	21.71
800 MHz	41.59	23.85	22.63
1 GHz	45.78	25.34	23.47

In the following figures 24, 25, 26, 27 and 28 are depicted the characteristics of filters designed for both in-band and out-of-band.

3.7.2 Ka-band with great SFR

In the previous section filters at Ka band with high Q factor have been presented. In that discussion no rules were imposed over the out of band rejection performances of filters. Now we want to demonstrate how is possible to improve the spurious features.

First of all we set as new specification the repetition of the filter beyond the second harmonic. In this way the evanescent coupling must be below cutoff at $2f_0$. This is a constraint on the

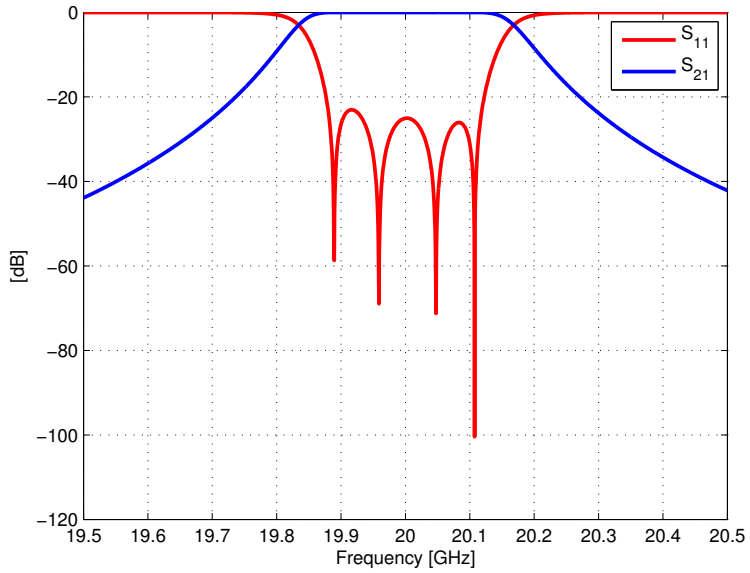

(a) In-band response

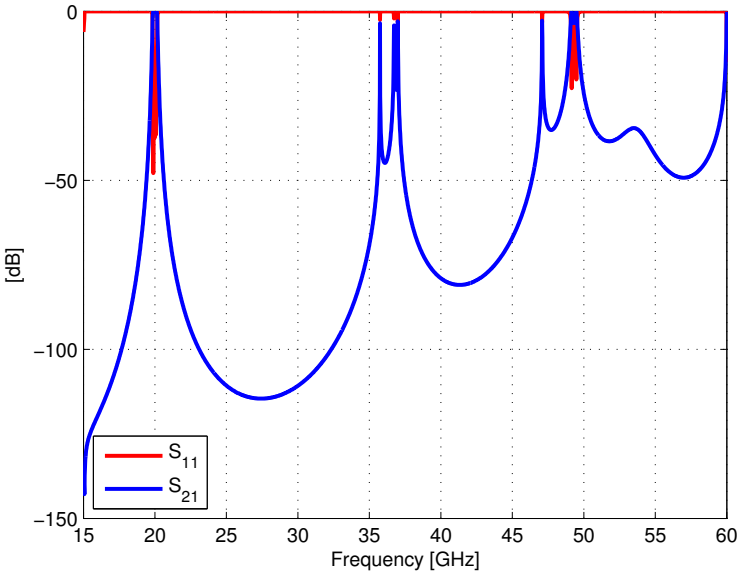

(b) Out-of-band response

Figure 24: Ka-band filter with $B = 230\,MHz$

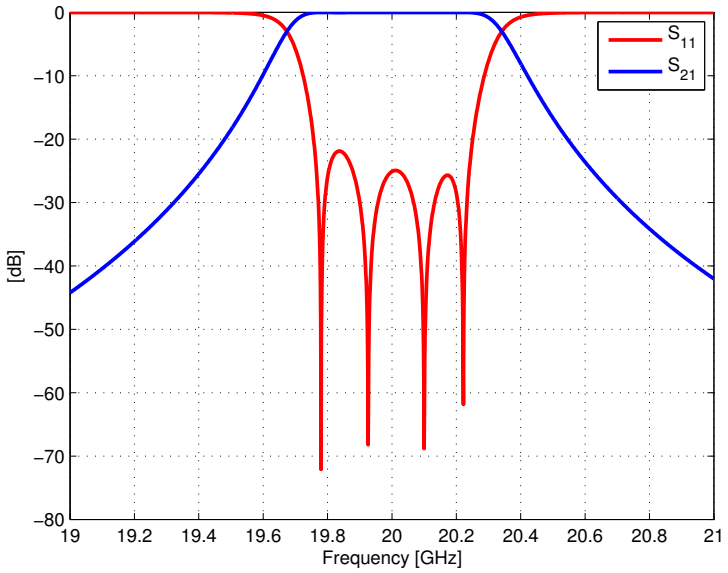

(a) In-band response

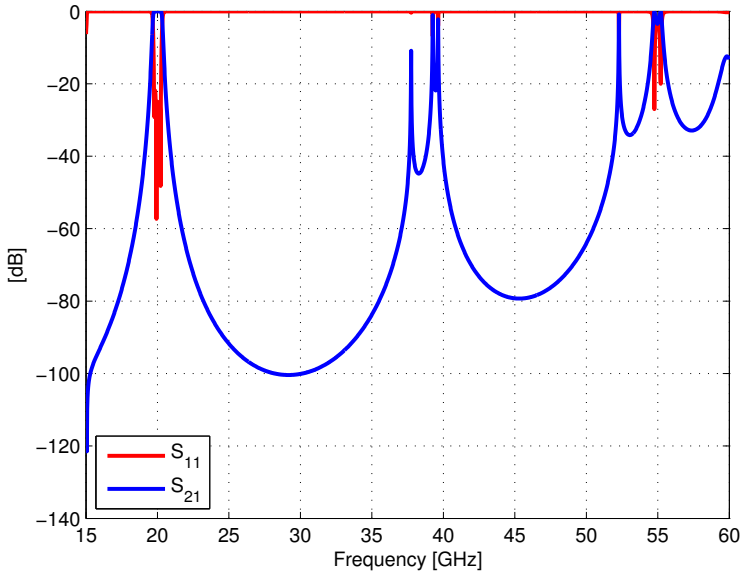

(b) Out-of-band response

Figure 25: Ka-band filter with $B = 500\,\mathrm{MHz}$

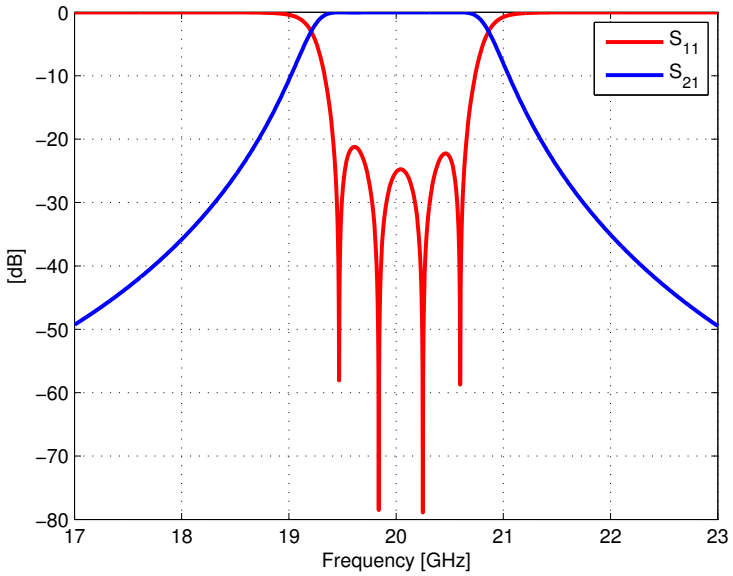

(a) In-band response

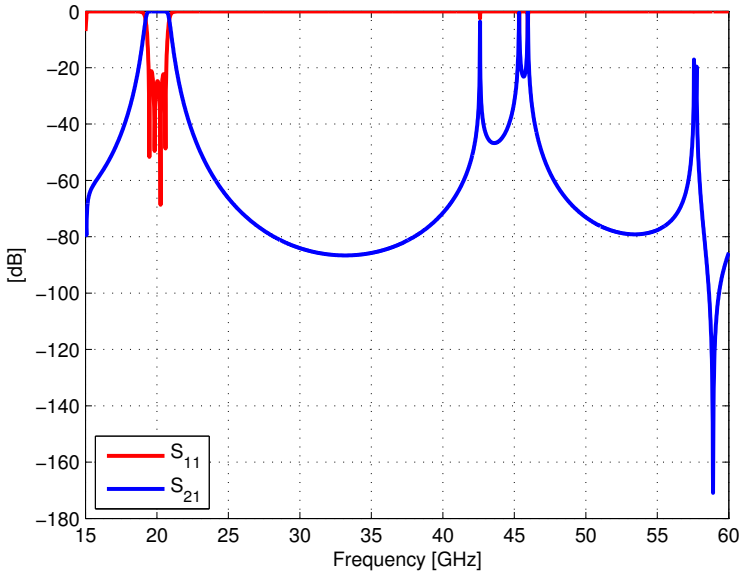

(b) Out-of-band response

Figure 26: Ka-band filter with $B = 1.2\,\mathrm{GHz}$

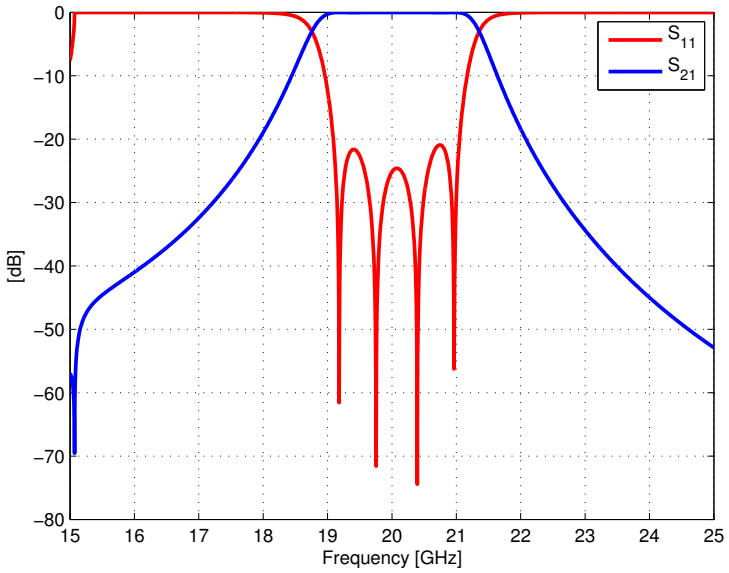

(a) In-band response

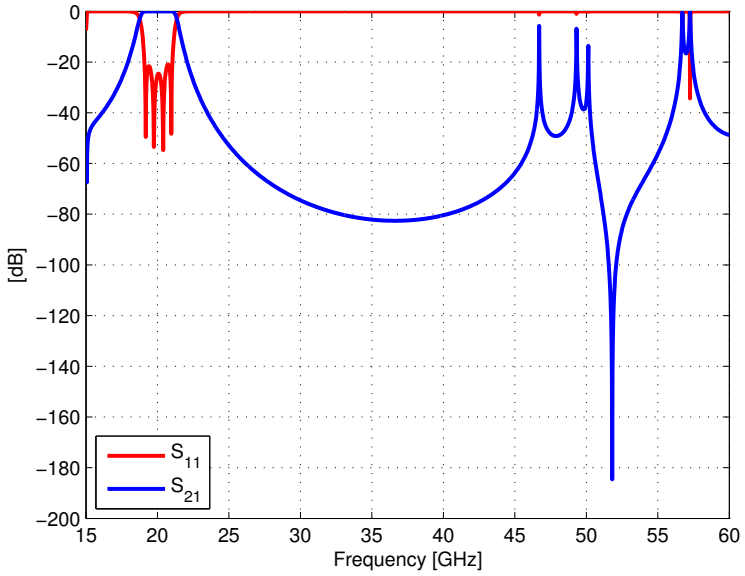

(b) Out-of-band response

Figure 27: Ka-band filter with $B = 2\,\mathrm{GHz}$

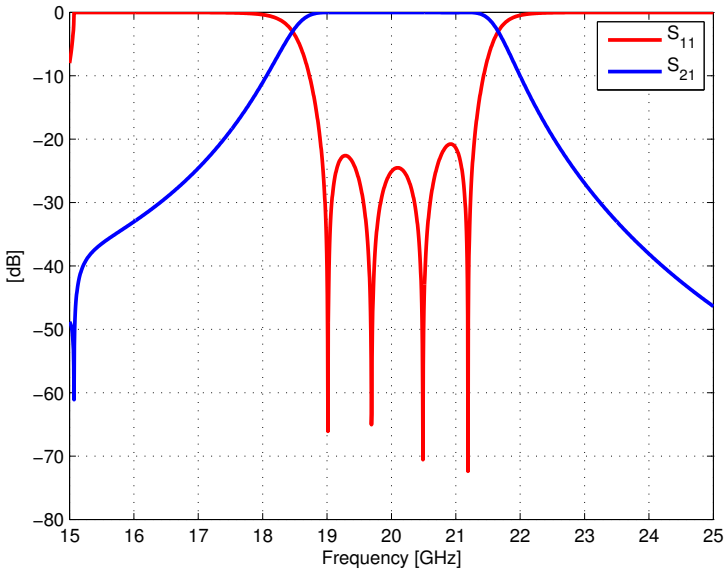

(a) In-band response

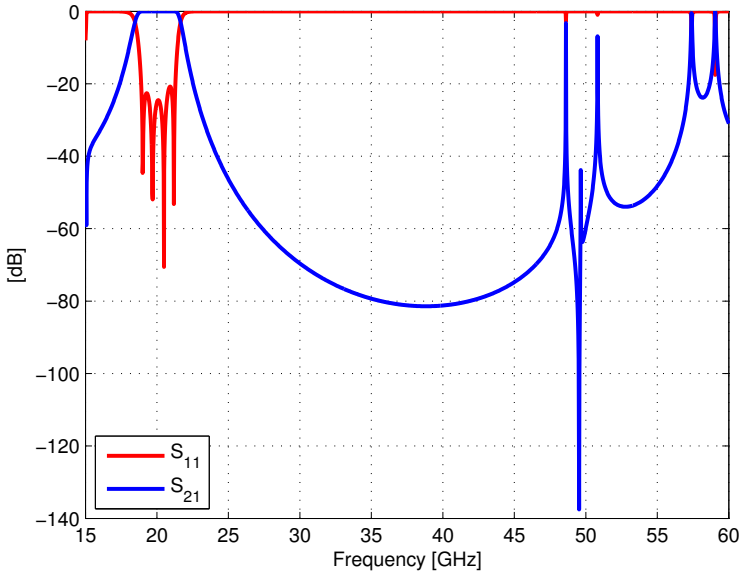

(b) Out-of-band response

Figure 28: Ka-band filter with $B = 2.3\,\mathrm{GHz}$

Table 9: Length of resonators for different bandwidths in mm at Ka-band

Bandwidth	$l_{r1} = l_{r4}$	$l_{r2} = l_{r3}$
100 MHz	1.4224	1.3314
200 MHz	1.5146	1.3383
500 MHz	1.7890	1.3821
800 MHz	2.0597	1.4630
1 GHz	2.2385	1.5363

a dimension of the envelope. Dimensions of the ridge must be indentified consequently to fix the cutoff frequency of the filter and to prevent excessive attenuations. This is a designing trade-off in which spurious rejection and Q factor are controlled by transverse dimensions. From table 10 is possible to understand

Table 10: Transverse dimensions of Ka-band ridge waveguide with high spurious performance

a	3.5 mm
b	1.575 mm
s	1.75 mm
d	0.1575 mm
b/a	0.45
s/a	0.5
d/b	0.1

that once the a dimension is fixed in order to guarantee the no-propagation at $2f_0$ the other parameters are calculated making a work trade-off with graphs of chapter 2. In this way is found that suitable ratios are : $s/a = 0.5$ and $d/b = 0.1$. Once these ratios are fixed, the dimensions of b, s, and d are known. To be noticed the smaller gap of the ridge. General parameters of this filter are listed in table 11.

At this point the procedure is the same of that describe in the previous sections. Here we want only to demonstrate that with the changing of the crosse dimensions is possible to meet the out

Table 11: High spurious Ka-band filter parameters

λ_c	20.485 mm
f_c	14.6347 GHz
λ_g	21.991 mm
$\lambda_{c_{waveguide}}$	7 mm
$f_{c_{waveguide}}$	42.827 GHz

Table 12: Dimensions of high spurious performance Ka-band filter

	100 MHz	800 MHz
l_{c1}	1.6723 mm	0.6026 mm
l_{c2}	4.2928 mm	1.7101 mm
l_{c3}	4.6699 mm	2.1426 mm
l_{r1}	1.4035 mm	2.1427 mm
l_{r2}	1.2801 mm	1.4518 mm
Φ_1	24.98°	45.92°
Φ_2	20.97°	24.73°
Φ_3	20.94°	22.80°

of band requirement. For this reason only 2 filters are designed in order to show this aspect: one for narrow bandwidth ($B = 100\,MHz$) and the second for wide bandwidth ($B = 800\,MHz$).

Following the design procedure, the values of $|S_{21}|$ have already been calculated and listed in table 6.

The others dimensions are immediatelly obtained for to the symmetry of the fiter (3.27). Simulation results (Figs. 29 and 30) show very good out of band performances: for the filter of nominal bandwidth of 100 MHz there is a spike over the 50 GHz and for the wideband filter of nominal bandwidth of 800 MHz the spike is above the 60 GHz that shows how this technology can be employed for rejection up to the *third* harmonic. In these filter we can also observe that the return loss and the central frequency are not always in accordance with specifications. This is due to the worst Q factor if compare with the previous filters. In this case an optimization would be required to obtain an equiripple return loss (RL). With FEST simulation tool, this optimization can be done in few seconds.

3.7.3 C-Band

Filters designed at Ka-band present dimensions of the order of few millimiters and they require great manufacturing precision. In order to simplify the work of the machine shop, has been decided to make another series of ridge filter at C-band. Specifications in these case have been chosen similarly to those of the Ka-band: For the out of band has been decided to have a spurius free range (SFR) up to the second harmonic with a rejection less than $-60\,dB$. As before, the constraint of the no repetition at $2f_0$ for the evanescent couplings fix the a dimension:

$$a \leqslant \frac{\lambda_{cwaveguide}}{2} \tag{3.28}$$

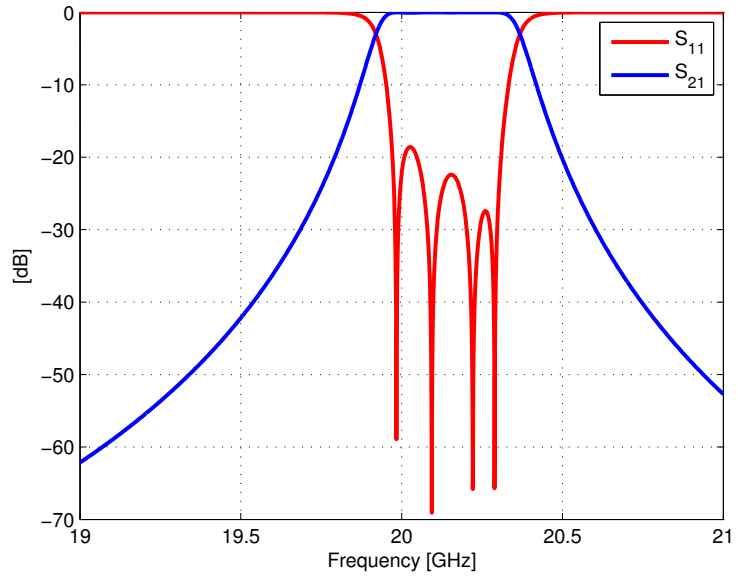

(a) In-band response

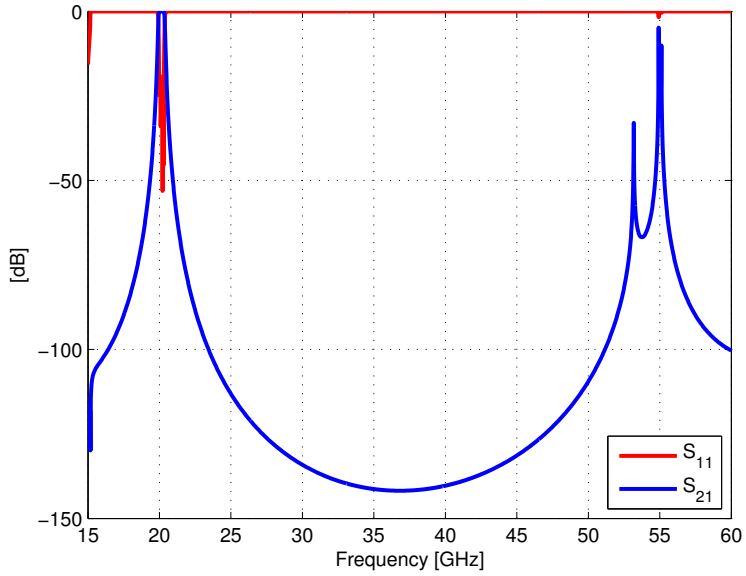

(b) Out-of-band response. The repetition is over the 50 GHz.

Figure 29: Ka-band filter with B = 230 MHz and high spurious

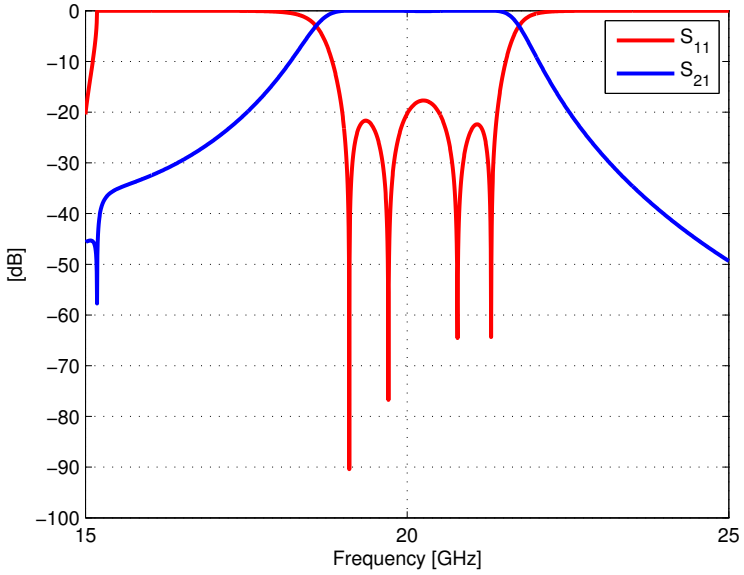

(a) In-band response

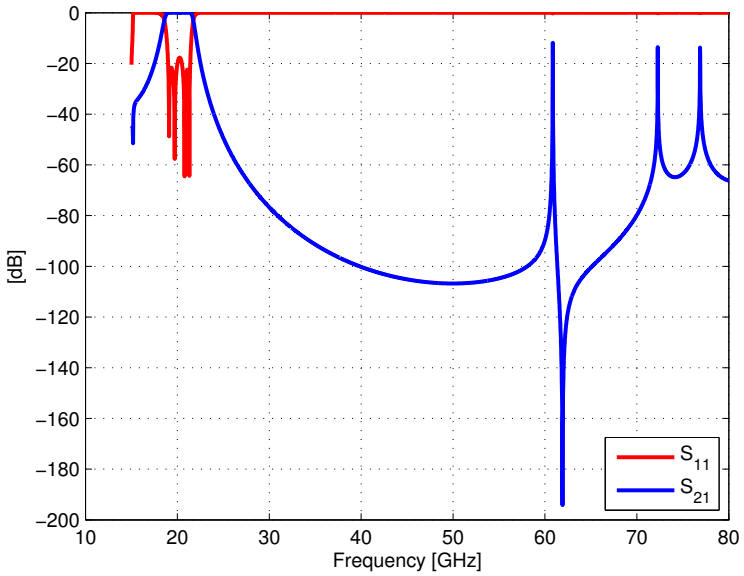

(b) Out-of-band response. To be noticed the high spurious free range beyond the third harmonic.

Figure 30: Ka-band filter with $B = 2\,GHz$ and high spurious

Table 13: C-band filter specifications

f_0	6 GHz
f_c	5 GHz
Filter order	4
Return Loss	25 dB

and since we impose that

Table 14: Cutoff of C-band rectangular waveguide couplings

$f_{c_{waveguide}}$	12 GHz
$\lambda_{c_{waveguide}}$	24.98 mm

Thus, for the (3.28), this is the conditions on the width of the waveguide:

$$a \leqslant 12.49\,mm \tag{3.29}$$

Now the ratios of s/a and d/b have to be evaluated in order to meet requirements of cutoff, bandwidth and attenuation. Studying graphs 4, 6, 7 and 18, the value of cross section have been fixed end listed in table 15.

Table 15: Transverse dimensions of C-band ridge waveguide filter

a	12.5 mm
b	5.6250 mm
s	6.2500 mm
d	0.84375 mm
b/a	0.45
s/a	0.5
d/b	0.15

From dimensions of table 15 the fundamental parameters of the waveguide are listed in table 16.

With the cross section defined the longitudinal dimensions are obtained with the full wave simulator as explained before. The bandwidths of interest are:

$$B = \{10; 27; 36; 54; 72; 100; 200; 300\}\ MHz \tag{3.30}$$

Firt to proceed in calculation of filter's parameters, we want to apply the theory of Levy described in section 3.6 in order to obtain better performances. By applying formula (3.23) the

Table 16: Fundamental parameters of the C-band ridge waveguide

λ_0	49.965 mm
λ_c/a	4.75
$Z_{PV}(\infty)$	41.055 Ω
$Z_{PV}(\omega_0)$	76.153 Ω
$\lambda_{c1}/\lambda_{c2}$	3.65
f_{c1}	5.053 GHz
f_{c2}	18.44 GHz

Table 17: Central frequencies and wavelength calculated with Levy's theory

Bandwidth	$\overline{\lambda_g}$ (mm)	$\overline{f_0}$ (GHz)
10 MHz	93.008	6
27 MHz	93.015	5.9999
36 MHz	93.021	5.9997
54 MHz	93.038	5.9994
72 MHz	93.061	5.9990
100 MHz	93.112	5.9980
200 MHz	93.434	5.9921
300 MHz	93.989	5.9820

following new central frequencies $\overline{f_0}$ and $\overline{\lambda_g}$ are obtained and listed in table 17.

These values replace the traditional f_0 and λ_g in formulas (A.36). The K inverters are calculated as usual. For these filters all values were normalized to impedance $Z_c = 1$ and the following K parameters of table 18 are calculated with this impedance.

The definition of impedance does not affect the value of the $|S_{21}|$ which are calculated with (3.6) and listed in table 19.

With FEST simulator evanescent coupling lengths are optimized in order to get scattering parameters of table. 19. The final results are listed in table 20.

The values of $\angle S_{11}$ evaluated at the dispersed central frequency $\overline{f_0}$ are then listed in table 21.

Finally using formula 3.10 the lengths of resonators are in table 22.

Simulation results for the synthesis of the C-band ridge filters are presented in Figs. 31, 32, 33, 34, 35, 36, 37 and 38 for all the bandwidths considered in this section. From this graphics is possible to see how the rejection condition is satisfied for all bandwidths and also for the extreme case of the last filter with very wide band response. Furthermore, with the Levy correc-

Table 18: Values of K inverters for C-band filters

Bandwidth	K_{01}	K_{12}	K_{23}
10 MHz	0.1097360	0.0094424	0.0069987
27 MHz	0.180329	0.025499	0.018899
36 MHz	0.208242	0.034003	0.025203
54 MHz	0.255096	0.051026	0.037820
72 MHz	0.294647	0.068075	0.050457
100 MHz	0.347462	0.094667	0.070167
200 MHz	0.49333	0.19083	0.14145
300 MHz	0.60831	0.29015	0.21506

Table 19: Values of $|S_{21}|$ couplings for different bandwidths in dB at C-band

Bandwidth	$\lvert S_{21_{01}}\rvert = \lvert S_{21_{45}}\rvert$	$\lvert S_{21_{12}}\rvert = \lvert S_{21_{34}}\rvert$	$\lvert S_{21_{23}}\rvert$
10 MHz	−13.276	−34.479	−37.080
27 MHz	−9.1360	−25.8547	−28.4535
36 MHz	−7.9768	−23.3591	−25.9559
54 MHz	−6.3929	−19.8462	−22.4373
72 MHz	−5.3165	−17.3598	−19.9431
100 MHz	−4.1513	−14.5329	−17.0994
200 MHz	−2.0087	−8.6770	−11.1397
300 MHz	−1.0316	−5.4290	−7.7209

tion we have all the filter perfectly centered at f_0 and dispersion is improved respect of the narrow band filter with high spurious at Ka-band of Fig. 29. These filters are a compromise between spurious repetition and value of Q. Theoretically it is possible to enhance the SFR but with higher attentions of the waveguide. The filters proposed are a compromise that meet both the specifications and satisfy the request of having a Q factor that is the higher possible.

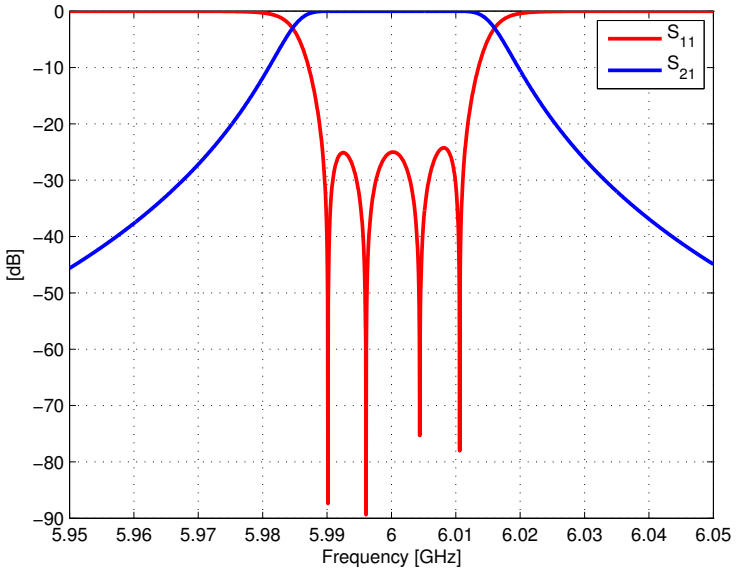

(a) In-band response

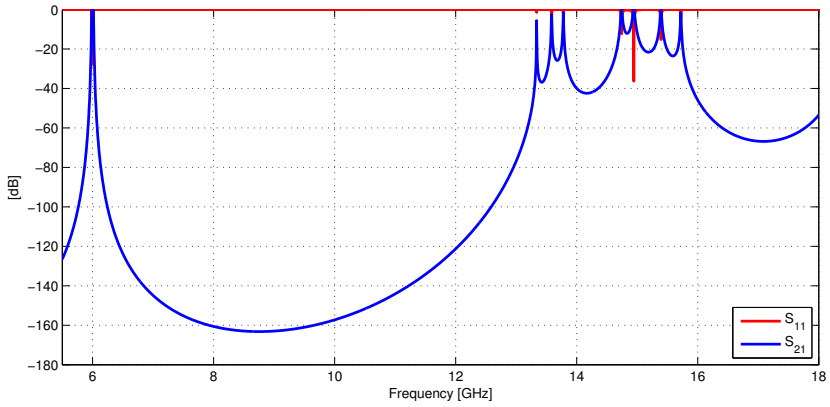

(b) Out-of-band response

Figure 31: C-band filter with $B = 22\,\mathrm{MHz}$

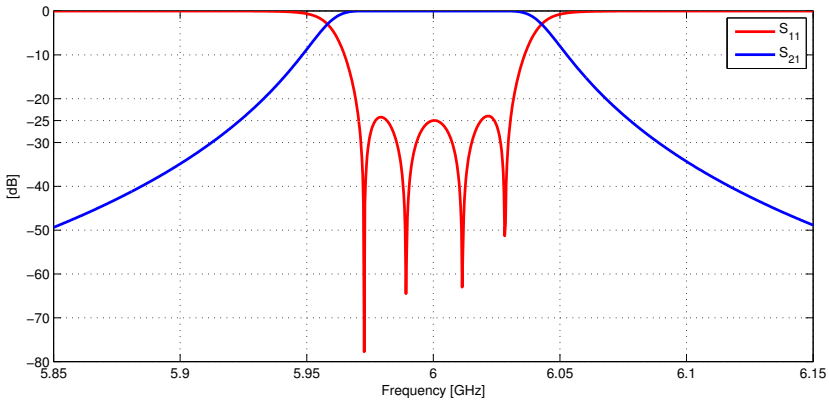

(a) In-band response

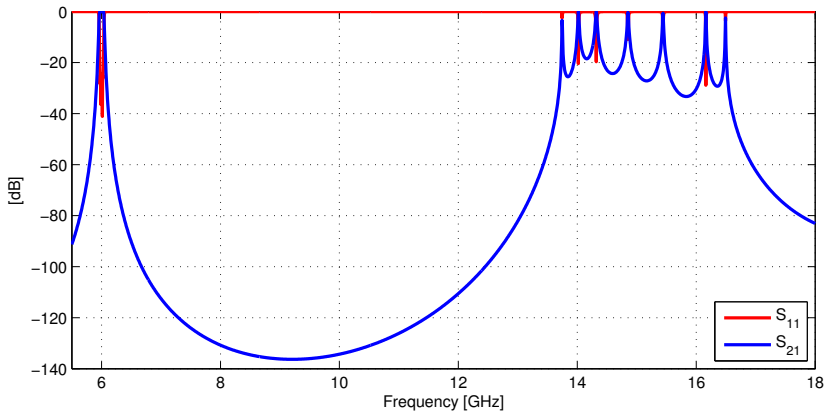

(b) Out-of-band response

Figure 32: C-band filter with $B = 60\,MHz$

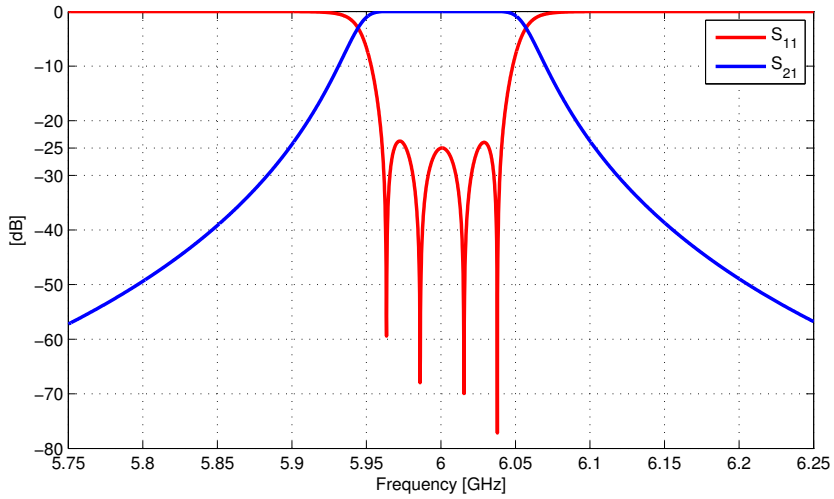

(a) In-band response

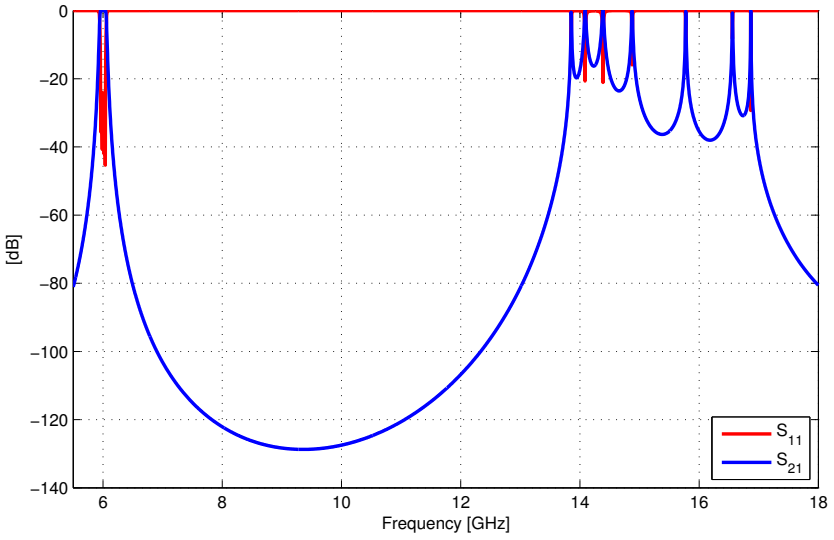

(b) Out-of-band response

Figure 33: C-band filter with $B = 81\,MHz$

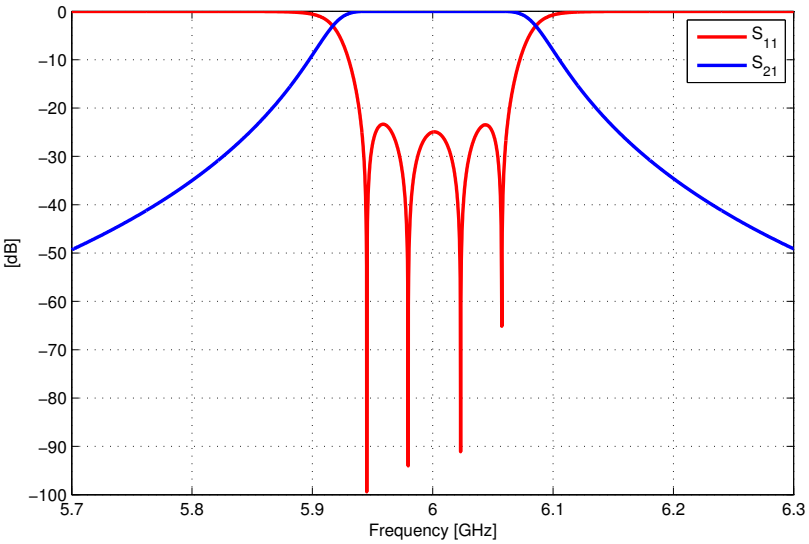

(a) In-band response

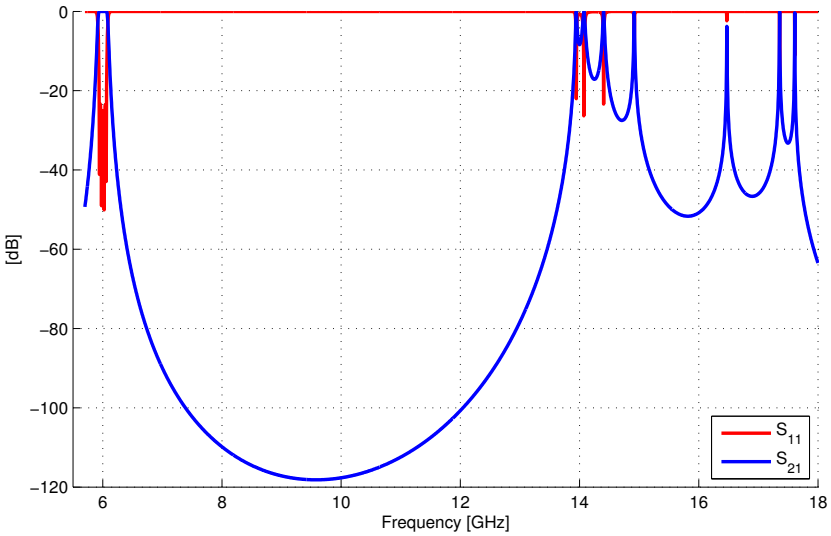

(b) Out-of-band response

Figure 34: C-band filter with $B = 122\,\mathrm{MHz}$

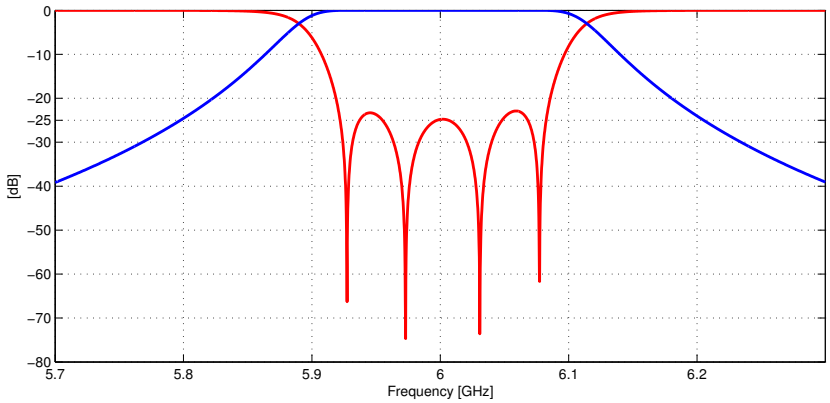

(a) In-band response

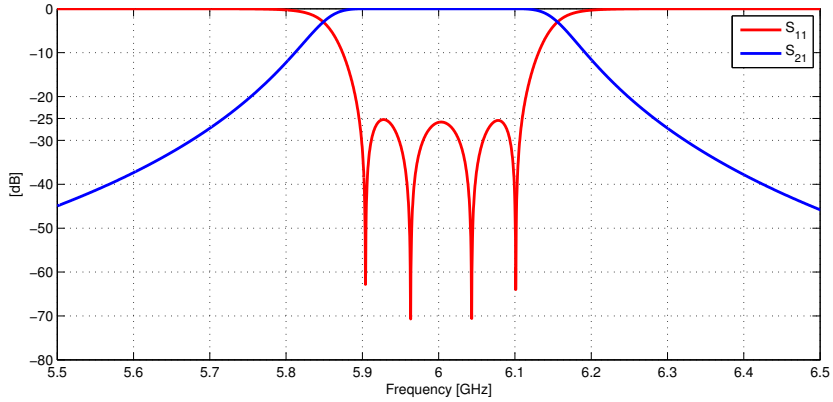

(b) In-band optimized response

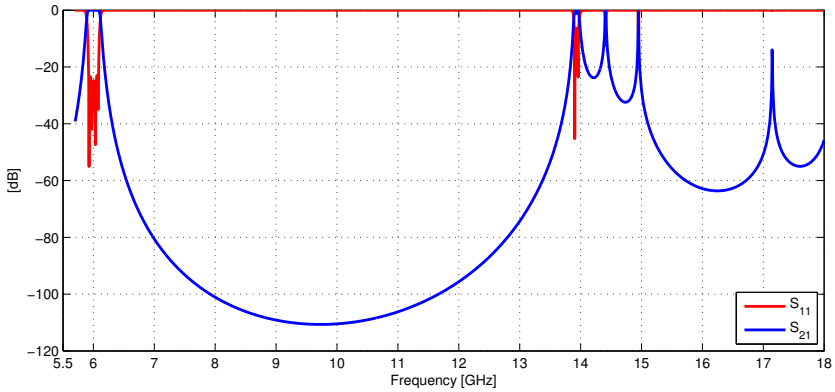

(c) Out-of-band response

Figure 35: C-band filter with $B = 164\,\mathrm{MHz}$

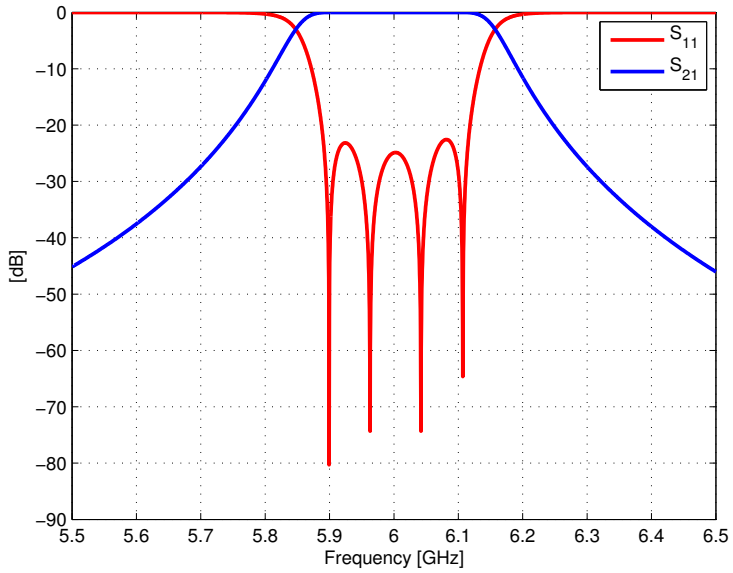

(a) In-band response

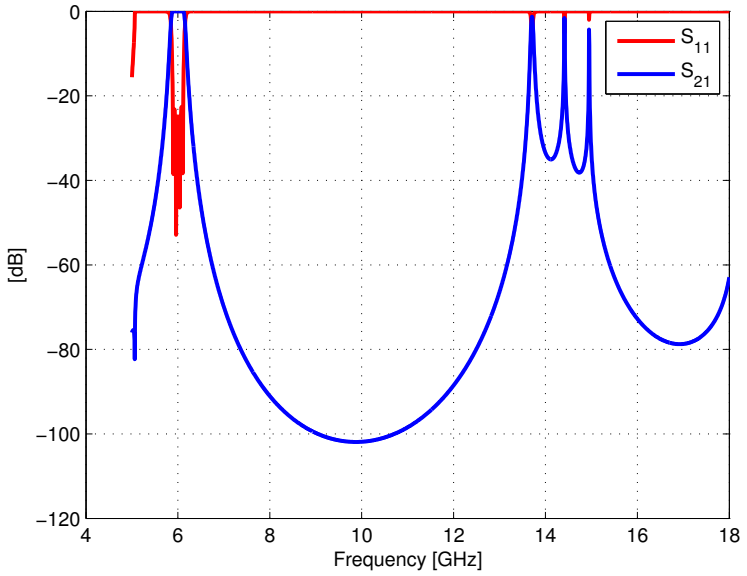

(b) Out-of-band response

Figure 36: C-band filter with $B = 226\,\mathrm{MHz}$

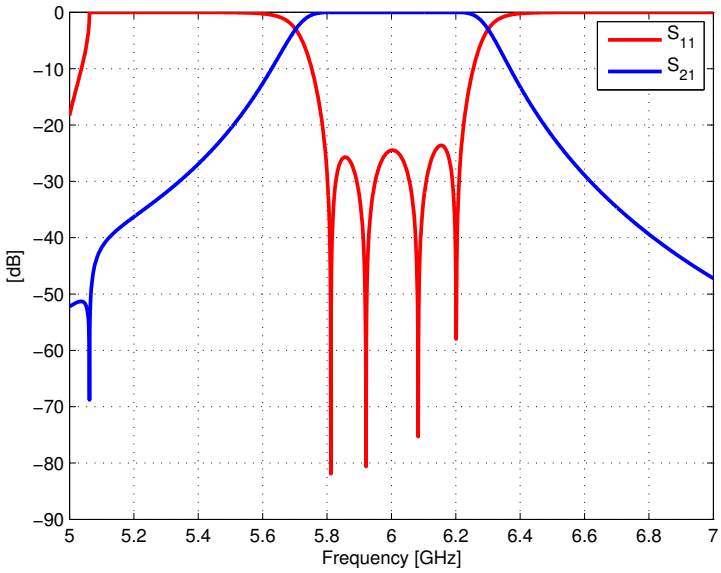

(a) In-band response

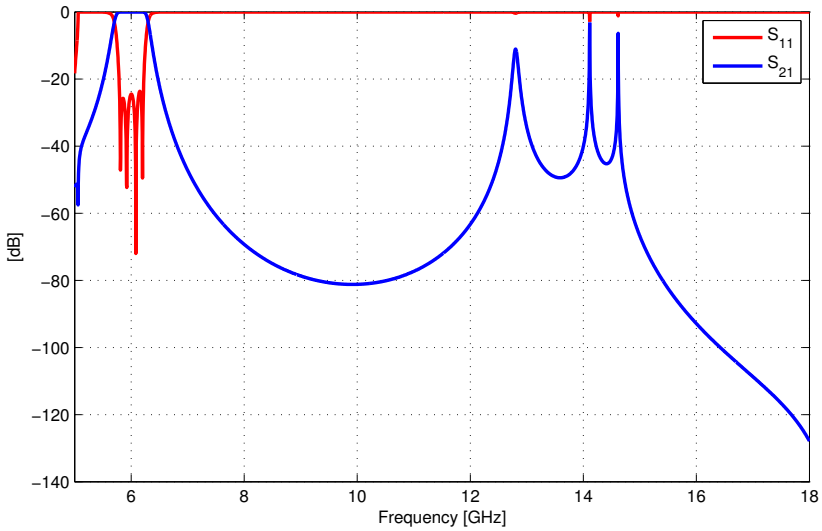

(b) Out-of-band response

Figure 37: C-band filter with $B = 425\,\mathrm{MHz}$

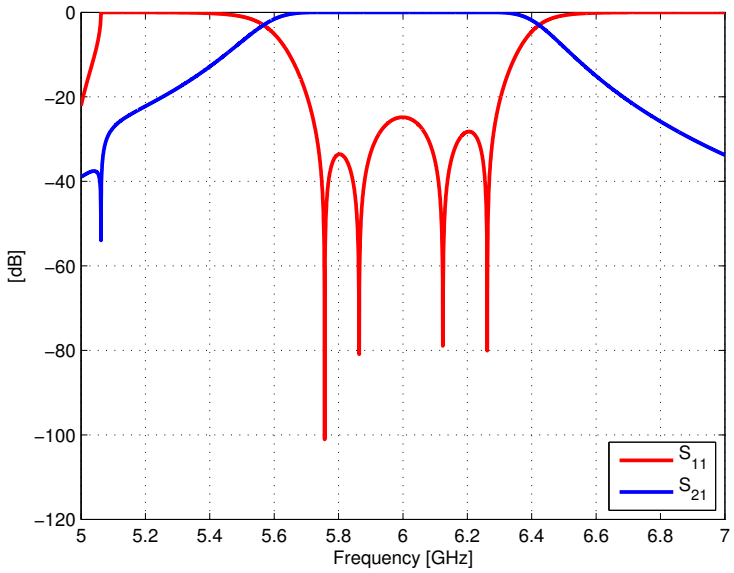

(a) In-band response

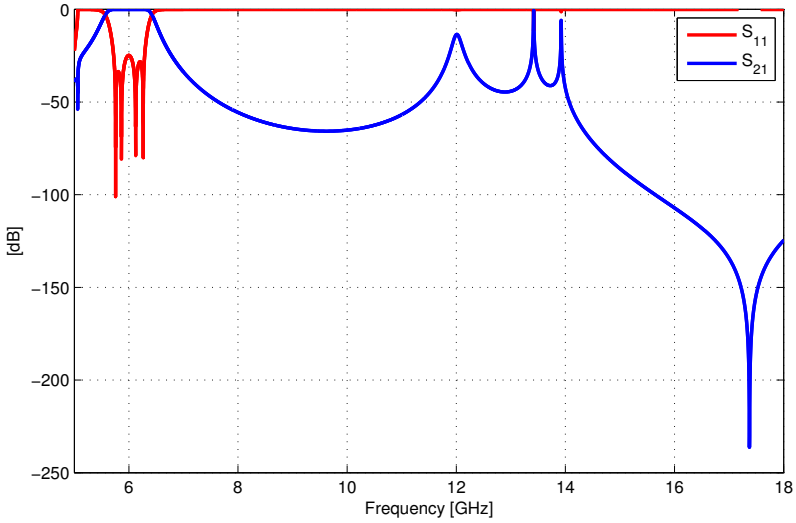

(b) Out-of-band response

Figure 38: C-band filter with $B = 570\,\mathrm{MHz}$

Table 20: C-Band coupling dimensions in mm

Bandwidth	l_{c1}	l_{c2}	l_{c3}
10 MHz	9.4122	20.6766	22.0529
27 MHz	7.1530	16.1111	17.4874
36 MHz	6.5051	14.7887	16.1649
54 MHz	5.6015	12.9246	14.3003
72 MHz	4.9702	11.6017	12.9767
100 MHz	4.2567	10.0915	11.4644
200 MHz	2.8037	6.9110	8.2778
300 MHz	1.9843	5.0634	6.3914

Table 21: C-Band phases of S_{11} in degrees

Bandwidth	Φ_1	Φ_2	Φ_3
10 MHz	34.69	33.54	33.53
27 MHz	36.64	33.60	33.57
36 MHz	37.64	33.65	33.60
54 MHz	39.60	33.79	33.68
72 MHz	41.49	33.99	33.78
100 MHz	44.34	34.44	34.05
200 MHz	53.29	37.18	35.65
300 MHz	60.75	41.63	38.32

3.8 TRANSFORMER SYNTHESIS

Use of the ridge filter in a satellite payload requires an additional interfacing network with the system. There are situations in which a particular type of transmission line is required by the pre-existing devices onboard and this factor must be taken into account. In our application a ridge waveguide transformer that matches the impedance of the ridge filter with the impedance of a standard rectangular waveguide at C-band WR-137 is required. The type of transformer of interest is a quarter wavelength composed by n steps.

There are two type of transformers:

HOMOGENEOUS used when two transmission lines have the same cut-off frequency;

INHOMOGENEOUS they come about when rectangular waveguides of different a dimensions are cascaded or when they are combined with ridge, circular or other types of waveguide.

Table 22: C-Band resonator lengths in mm

Bandwidth	l_{c1}	l_{c2}
10 MHz	8.8138	8.6639
27 MHz	9.0741	8.6775
36 MHz	9.2104	8.6884
54 MHz	9.4834	8.7184
72 MHz	9.7559	8.7594
100 MHz	10.1880	8.8573
200 MHz	11.7402	9.4511
300 MHz	13.3647	10.4367

Our case requires a *inhomogeneous* transformer. Using as reference model the figure 11 on page 25 it is possible to identiy the impedance of ridge (Z_{ridge}) the one of rectangular waveguide ($Z_{waveguide}$) and the impedances of each step Z_i. In some books the impedances of each step are associated to numbers only, so in this case we can rename the impedance of ridge with Z_0 and the impedance of rectangular waveguide WR-137 with Z_{n+1} where n is the number of steps. The synthesis of the transformer can be summarized in the following passages:

1. Determine the number of steps depending on reflections requirement.
2. Calculate the value of impedance of each steps.
3. Obtain the dimensions of ridge waveguide for each step that give the desired value of impedance.
4. Optimization of the structure in order to meet specifications of bandwidth and reflections.

Designed transformer will be suitable for the C-band presented in the previous sections so its bandwidth must be that of the filter with the wider bandwidth. For this reason we design a transformer of $B = 600$ MHz. The quarter wave transformer fractional bandwidth parameter is defined as:

$$w_g = 2\left(\frac{\lambda_{gA} - \lambda_{gB}}{\lambda_{gA} + \lambda_{gB}}\right) \tag{3.31}$$

where λ_{gA} and λ_{gB} are the longest and the shortest wavelengths in guide, respectively, in the pass band of quarter-wave transformer. The length L of each section (Fig. 11) is nominally one-quarter wavelength at central frequency and is given by:

$$L = \frac{\lambda_{gA}\lambda_{gB}}{2(\lambda_{gA} + \lambda_{gB})} = \frac{\lambda_{g0}}{4} \tag{3.32}$$

For the our filter is necessary a transformer with a return loss that is less of $-25\,\mathrm{dB}$ this means that in term of VSWR it must be:

$$\rho = \frac{1+|\Gamma|}{1-|\Gamma|} = 1.12 \tag{3.33}$$

The same *power-voltage* definition of impedance has been chosen for both ridge and rectangular waveguide. For Ridge it has been calculated with the graph of Fig. 8 on page 23, and for rectangular waveguide with the following formula:

$$Z_{\text{WR-137}} = 2\frac{b}{a}\frac{120\pi}{\sqrt{1-\left(\frac{f_{c_{\text{WR-137}}}}{f0}\right)^2}} \tag{3.34}$$

The value of impedances of the ridge and rectangular waveguide are:

$$Z_{\text{ridge}} = 76.528\,\Omega \tag{3.35}$$

$$Z_{\text{WR-137}} = 486.64\,\Omega \tag{3.36}$$

Variable R is the ratio between the impedance of rectangular waveguide and the ridge waveguide:

$$R = \frac{Z_{n+1}}{Z_0} \tag{3.37}$$

thus, the transformer has the following parameters:

$$w_q = 0.17288 \tag{3.38}$$

$$R = 6.3590 \tag{3.39}$$

In order to know how many steps are required for our transformer, is useful to look tables of [25, p. 267] where can be seen that for parameter values (3.38) and (3.39), to achieve a VSWR minimum of 1.12 (3.33) at least a *two* steps transformer is required.

The conditions that an ideal inhomogeneous transformer of two sections be maximally flat can be written for TE modes as:

$$\left(\frac{Z_2}{Z_1}\right)^2 = R \tag{3.40a}$$

$$\lambda_{g2}^2 - \lambda_{g1}^2 = \frac{1}{2}(\lambda_{g3}^2 - \lambda_{g0}^2) \tag{3.40b}$$

$$\left(\frac{Z_1}{Z_0}\right)^2 = \frac{\lambda_{g1}^2 + \lambda_{g2}^2\sqrt{R}}{\lambda_{g1}^2 + \lambda_{g2}^2\frac{1}{\sqrt{R}}} \tag{3.40c}$$

Conditions (3.40) are a system of three equations for 4 variables λ_{g1}, λ_{g2}, Z_1 and Z_2. Thus there are an infinity of maximally flat transformers of two sections and some have flatter responses than others. In most practical cases the transformer should have minimum reflection over a finite frequency band, rather than having maximally flat frequency response. A solution can be the optimization of the structure in order to obtain desired values of return loss. This procedure was employed in our application.

In order to obtain first transformer dimensions, the wavelength of the first step has been chosen arbitrarily to be

$$\lambda_{g1} = 80\,\mathrm{mm} \tag{3.41}$$

Thus by solving equations (3.40) is possible to obtain the first target parameters which are listed in table 23.

Now that we know the impedances and cut-off frequencies of both steps, it is possible to use graphs of Figs. 4 and 8 in order to obtain the dimensions of the two ridge waveguides. For practical reasons, the width dimension of all the ridges has been decided to fix to the width of the filter. In this way all the ridges are the same width and this will facilitate the manufacturing:

$$s_1 = s_2 = s_{\mathrm{ridge}} = 6.25\,\mathrm{mm} \tag{3.42}$$

Finding the exact dimensions of the ridge that meet values of table 23 and ridge condition (3.42) is difficult by hands. So the dimensions found are an approximation of the target values. They are listed in table 24. The VSWR of the deriving from first dimensions is shown in Fig. 39a.

At this point lengths and the gaps dimensios of the two steps are optimized using the EM simulator in order to obtain the desired maximum value of return loss in band. A *genetic algorithm* was used to optimized dimensions, which are finally listed in table 25.

Results in term of VSWR after the optimization are presented in Fig. 39b. In this figure is possible to notice that the requirements

Table 23: Transformer initial parameters

Parameter	step 1	step 2
λ_g	80 mm	68.372 mm
λ_c	63.979 mm	73.198 mm
$Z_{PV}(\omega_0)$	113.60 Ω	286.47 Ω
$Z_{PV}(\infty)$	70.953 Ω	209.35 Ω
length	20.025 mm	17.102 mm

Table 24: Transformer initial dimensions in mm

	step 1	step 2
a	16	27.5
b	7.2	12.375
s	6.25	6.25
d	1.656	6.9
length	20.025	17.102

Table 25: Transformer optimized dimensions in mm

	step 1	step 2
a	16	27.5
b	7.2	12.375
s	6.25	6.25
d	1.7613	6.9916
length	20.5427	14.5579

are satisfied in all the band and that in the worst case the value of the VSWR is 1.08.

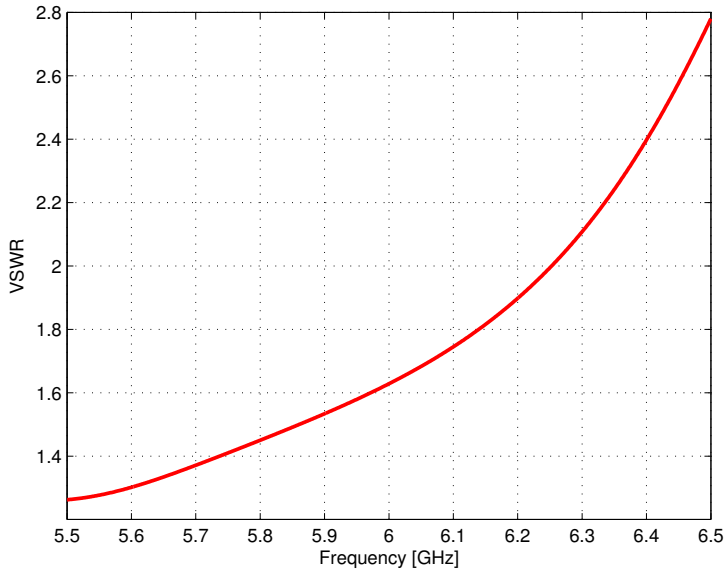

(a) VSWR of first transformer's dimensions

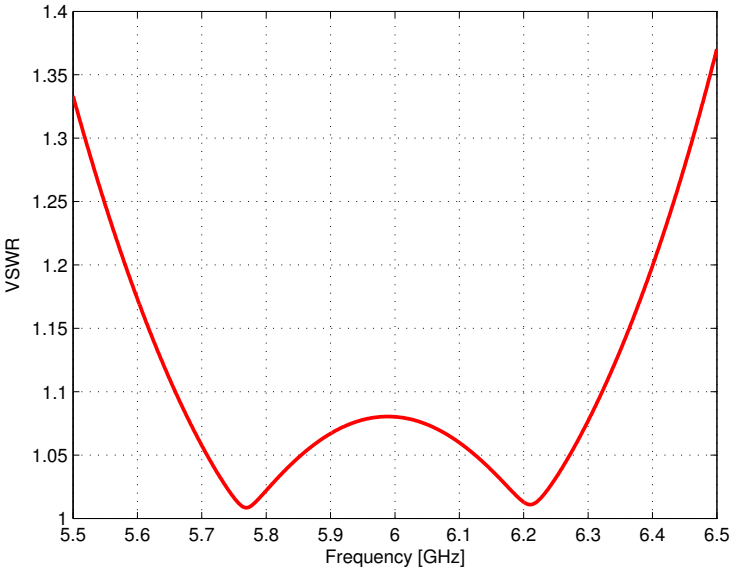

(b) Optimized and final VSWR

Figure 39: VSWR of transformer

3.9 ZAKI METHOD

An alterantive approach for the synthesis of ridge waveguide filter has been tested using methodoloy described in the article [45]. In this paper is presented a design procedure that permits to obtain the correct dimensions of the filter starting from the specification with the use of a full wave simulator. This method was initially designed for dieletric resonators, and consequently for narrow band filters. Now we want to apply these procedures to ridge waveguide filters for both narrow and wide band filters. This method can replace the design procedure of 3.5.2 while the procedure for obtaining the transverse dimensions remains unchanged.

The equivalent circuits of two series resonators coupled are shown in Fig. 40.

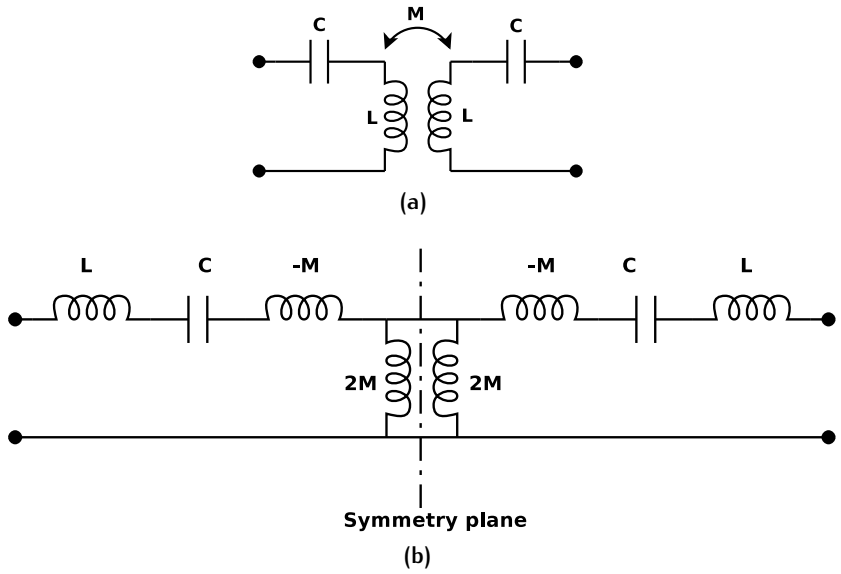

Figure 40: Equivalent circuits for coupled resonators

For any particular mode near its resonance, an equivalent circuit for the two coupled resonator is shown in Fig. 40a. The coupling coefficient k between the resonators is defined in terms of the equivalent circuit element by:

$$k = \frac{M}{L} \tag{3.43}$$

More interesting is the equivalent circuit of Fig. 40b in which the $L - C$ circuit of the resonator is connected to a T of immitances in a very similar way of Fig. 94 on page 144. In this circuit is

also indicated the *symmetry plane* in the middle. At this point the coupling coefficient may be rewritten in this manner:

$$k = \frac{M}{L} = \frac{f_e^2 - f_m^2}{f_e^2 + f_m^2} \tag{3.44}$$

where f_e and f_m are, respectively, the resonance frequency if we put an *electric* wall or a *magnetic* in the middle of the circuit.

It is well known that the coupling coefficient k between resonators i and $i+1$ can be also be represented by:

$$k_{i,i+1} = \frac{B}{f_0} \frac{1}{\sqrt{g_i g_{i+1}}} \tag{3.45}$$

Now a technique using the method of Zaki but applied to ridge filter will be described. The idea is to use (3.45) in order to optimize evanescent couplings with an EM in order to meet the specifications. Unlike the method of Zaki that considers a structure of 2 dieletric resonators that have a certain distance each others and a distance from the shorted circuit at the ends of resonators, an alterantive approach has been used. The idea is to place a *magnetic* wall in the middle of resonator and optimizing the length of coupling and the length of *half-resonator* in order to achieve a desired k and f_0. At this point, an eigenmode simulation is performed in order to optimize both the dimensions of half resonator and coupling, having as a goal functions the value of coupling coefficient k calculated with formula (3.44) and the central frequency f_0 given by:

$$f_0 = \sqrt{f_e \cdot f_m} \tag{3.46}$$

With this method is possible to calculate with the EM simulator both k and f_0 of a given coupling structure by simulating f_e and f_m. The importance thing to notice is that with our method is *not* possible to optimize directly value of k theoretically evaluated with formula (3.45) because of the different equivalent circuit used in the simulation.

Dividing by two a serie resonator, its element change: reactance L is divided by 2 and susceptance C is multiplied by 2 as depicted in Fig. 41. The consequence is that the values of coupling coeficients k of these structures are not the same of those of Fig. 40. Indeed the new couplings coefficients that we call $\overline{k}$ must be recalculated. The resonance frequency of a resonator defined in (A.23) is evaluated for both even and odd mode. From Fig. 41a, the resonance frequency for the odd mode is:

$$\omega_e^2 = \frac{1}{(L - 2M)C} \tag{3.47}$$

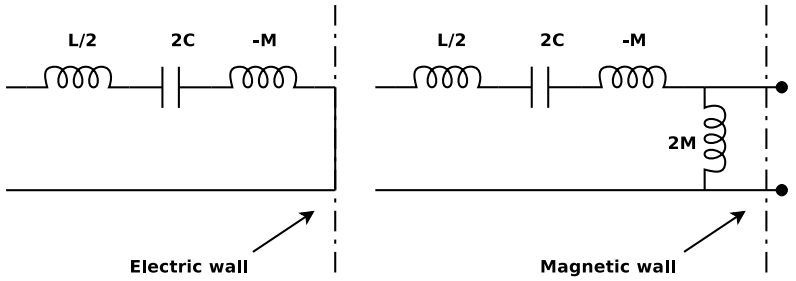

(a) Odd mode **(b)** Even mode

Figure 41: Equivalent circuits for resonators bounded by magnetic walls

and from Fig. 41b the magnetic frequency is given by:

$$\omega_m^2 = \frac{1}{(L+2M)C} \tag{3.48}$$

Thus, the coupling coefficient for our structure is obained combining eqs. (3.47) and (3.48) into (3.44):

$$\begin{aligned} \overline{k} &= \frac{\omega_e^2 - \omega_m^2}{\omega_e^2 + \omega_m^2} \\ &= \frac{\frac{L+2M-(L-2M)}{(L-2M)(L+2M)C}}{\frac{L+2M+L-2M}{(L-2M)(L+2M)C}} \\ &= 2\frac{M}{L} \\ &= 2k \end{aligned} \tag{3.49}$$

From (3.49) is possible to see that the value of coupling coefficient to optimize in the EM simulation structure where magnetic walls were put as boundary conditions in the middle of resonators, is twice. This method is valid only for the internal couplings. For external couplings others methods have to be used such as the *group delay* method. In this work the external couplings are obtained with optimization. Using the technique explained before, two examples filters of fractional bandwidth 1% and 10% will be designed.

3.9.1 Narrow band filter

The synthesis of a narrow band filter is now presented. The filter has a central frequency of 6 GHz and a bandwidth of 60 MHz

($w = 1\%$). The other specifications are the same of filter presented for C-band. The values of k are calculated with (3.45) and $\overline{k}$ with (3.49):

$$k = \{0.015216; 0.010409; 0.00771; 0.010409; 0.015216;\} \quad (3.50)$$

$$\overline{k} = \{0.030432; 0.020818; 0.01543; 0.020818; 0.030432;\} \quad (3.51)$$

The simulator optimizes the internal couplings and resonators, results are listed in table 26.

Table 26: Dimensions for 1% bandwidth filter with Zaki method

	variable	value (mm)
Zaki method	l_{c2}	16.0934
	l_{c3}	17.4733
	l_{r2A}	4.304 18
	l_{r2B}	4.2999
	l_{r2}	8.604 17
optimization	l_{r1}	9.001 807
	l_{c1}	7.138 884

where l_{r2A} and l_{r2B} are the half resonators left and right parts. The length of the second resonator is the sum of the two half: $l_{r2} = l_{r2A} + l_{r2B}$. The response of this filter is shown in Fig. 42. The in band response shows an equiripple return loss of -25 dB and a bandwidth of exact 60 MHz. The ouf of band does not change from those showed in the previous paragraphs.

3.9.2 Wide band filter

The method of Zaki was initially designed for dieletric resonators filters, indeed for narrow bandwidth. In this paragraph a method for wideband filters of 10% of fractional bandwidth will be described.

As explained before, the coupling coefficients are first calculated:

$$k = \{0.15216; 0.10409; 0.0771; 0.10409; 0.15216;\} \quad (3.52)$$

$$\overline{k} = \{0.30432; 0.20818; 0.1543; 0.20818; 0.30432;\} \quad (3.53)$$

Then the Zaki procedure is applied and results are shown in table 27.

Response after the optimization of the external couplings and resonators demonstrates that the circuital model is not suitable for wide band applications.

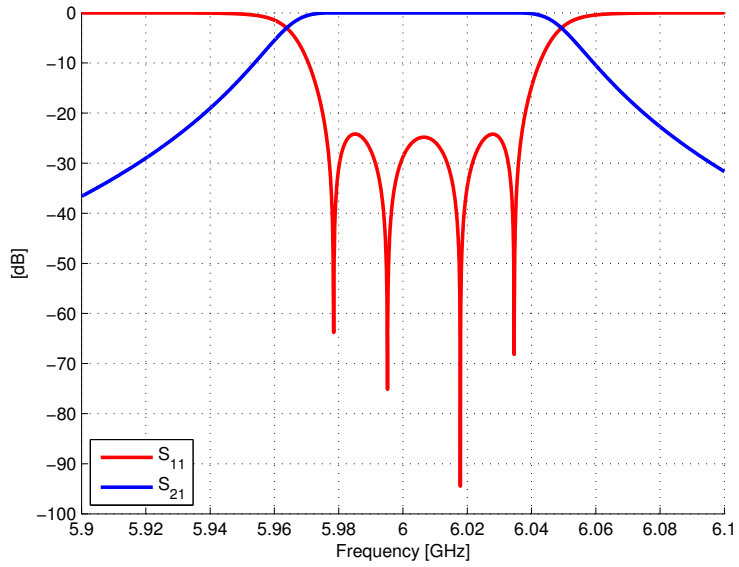

(a) In band response. The bandwidth is correct and equal to 60 MHz

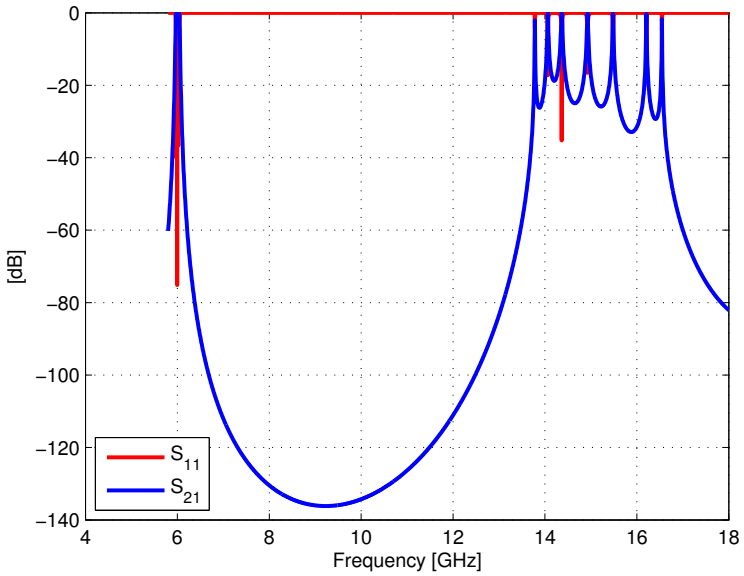

(b) Out band response

Figure 42: Response of 1% filter designed with Zaki method

Table 27: Dimensions for 10% bandwidth filter with Zaki method (first step)

	variable	value (mm)
Zaki method	l_{c2}	4.978 52
	l_{c3}	6.614 493 4
	l_{r2A}	5.229 48
	l_{r2B}	4.755 766
	l_{r2}	9.985 243
optimization	l_{r1}	13.286 83
	l_{c1}	1.827 715 343

Fig. 43a shows the in band response of the wide band filter designed with the method of Zaki. As it is possible to see, the return loss is not equiripple and out of specs, not all four poles are visibles. This is caused by the impossibility to put the magnetic wall exactly in the middle of resonator during the dimensional procedure. This technique is valid for narrow band filters when the lengths of resonators are quite similar: in this scenario putting the magnetic wall in the middle of resonator means having it very closed to the middle of resonator. From table 27 is evident that l_{r2A} and l_{r2B} are different and this is the explanation of the wrong return loss of the filter. However, the bandwidth is almost correct as well the central frequency.

To obtain the correct characteristic a *second step* is performed. Once we have the two half lengths of the resonators, we perform another optimization to the cavity but fixing the half resonator dimension as the average of the two lengths found in the step before. In this way we approximate the length of resonator using information of the step before and the procedure is repeated. In this secon step, the cavity is composed by the two half fixed resonators and the coupling, but now we have only one variable, that is the length of the coupling, and only one goal function that is the coupling coefficient $\overline{k}$. Also in this case only the internal couplings and resonators are evaluated while the externals are optimized as usual. Final dimensions after the second step are listed in table 28 and showed in Fig. 43b.

Results of this technique demonstrate that the correct bandwidth and equiripple return loss coherent with specifications are obtained. However, the computational time required for this technique exspecially for the wideband filters is significantly higher with respect to the procedure presented in section 3.5.

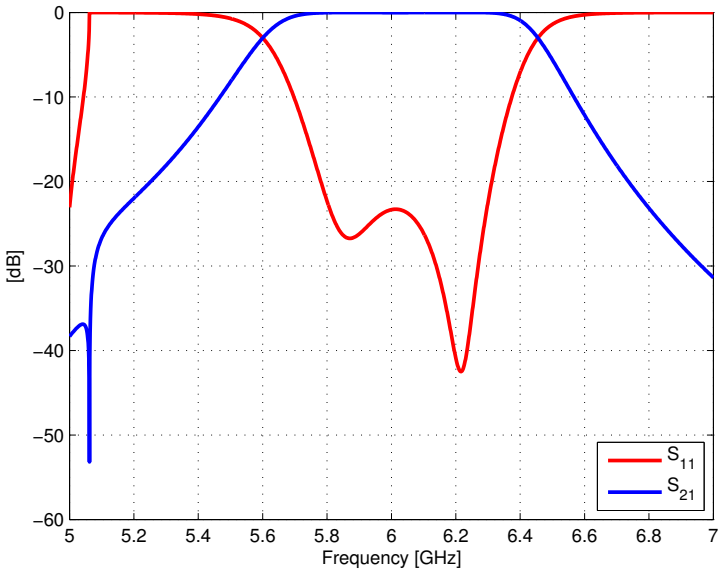

(a) First step

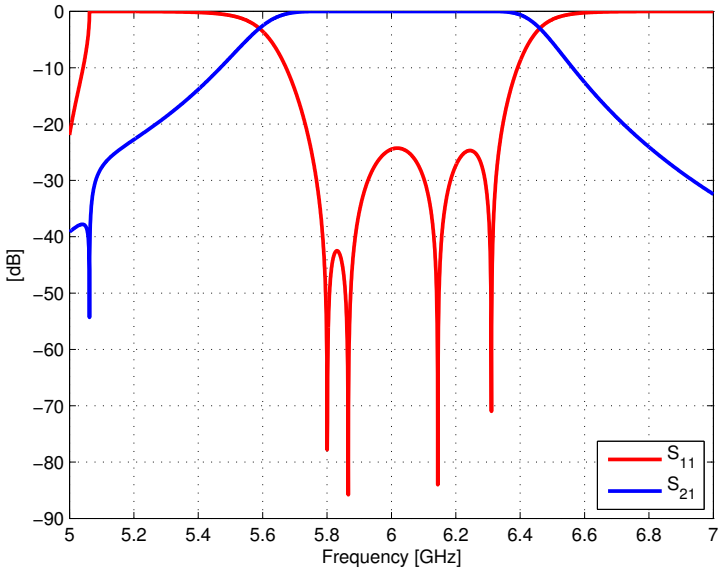

(b) Second step

Figure 43: Response of 10% filter designed with Zaki

Table 28: Dimensions for 10% bandwidth filter with Zaki method (second step)

variable	value (mm)
l_{c1}	1.9985
l_{c2}	5.1154
l_{c3}	6.4681
l_{r1}	12.9907
l_{r2}	9.9852

3.10 COMMENTS ON SIMULATIONS RESULTS

Using the method of synthesis proposed in section 3.5 the resulting ridge filters present good performance for out-of-band rejection and in-band return loss, but the finel bandwidth is enlarged by a factor of $2 \div 2.3$ with respect of the specification. In order to try to understand the problem let consider distribution of the fields of Fig. 44 at central frequency f_0:

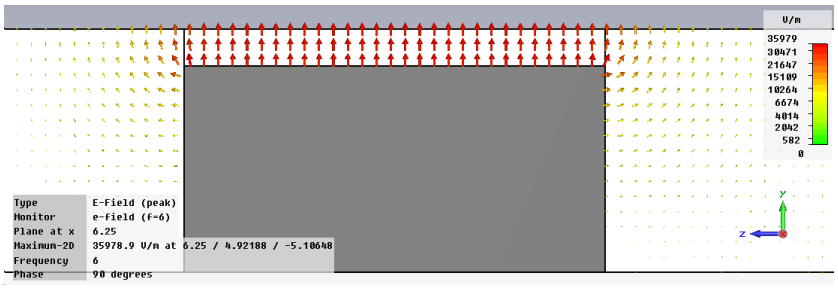

(a) Electric field. Lateral view

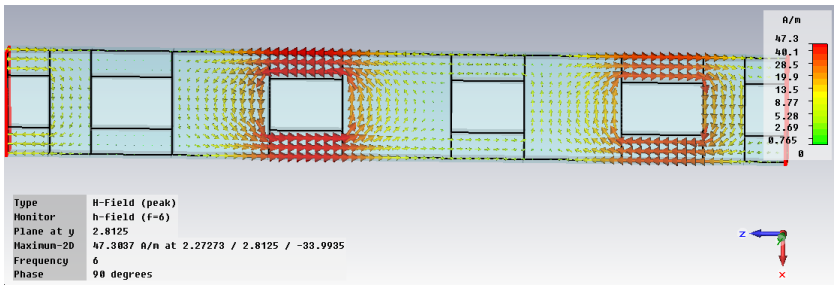

(b) Magnetic field. Top view

Figure 44: Fields distribution in ridge resonators

In Fig. 44a is showed the distribution of the electric field of the ridge resonator observed by the lateral view. It is possible to notice that distribution of the E field is manly concentrated in the gap where it is constant. The magnetic field is depicted

in Fig. 44b: it is circular around the ridge. In the gap the almost constant E field and the perpendicular H field indicate that the resonance mode is not a pure TE_{10} mode but it seems more a TEM mode instead. This is due to the reduced length of the resonators, that looking to dimensions of previous tables it is about one tenth of the wavelength in guide. In the situation in which $l_r \simeq \lambda_g/10$ the resonator operates like a concentrated capacitance. That structure reminds the *comb line* filter in which cylindrical posts are tuned by adjusting the capacitance on the top. However, the mode in our ridge filter is not exactly a TEM mode but it is a quasi-TEM. This means for examples that formulas for calculating K inverters have to be corrected for taking into account the type of the mode.

For our further discussion in chapter 4, the problem related to the bandwidth is not relevant. This is a sistematic error that can be controlled by a bandwidth scaling factor and when comparing two different filters the important thing to do is to check that the measured bandwidth of them is the same. Results demonstrate that the repetition of the filter is mainly affected by the transverse dimensions of the ridge instead of the bandwidth. For this reason we can conclude that the problem in section 3.5 does not affect the conclusions and the results of the next discussion.

4 RIDGE FILTER COMPARED WITH MODULAR BASELINE

In these chapter a possible application of the ridge filter will be described. This type of technology has been extensevely empolyed in the field of satellite payloads due to its properties in terms of SFR and compact size [15, 30–34, 37, 42]. Current design baseline for C-Band, Ku-Band and Ka-Band consists of a complex IFA, where multiple filter units are cascaded together. A first filter, typically high-order TE_{11n} or TE_{10n} mode band pass filter (BPF), between 3% and 5% fractional bandwidth, provides the IFA in-band characteristic and the required near-band rejection. A broadband low pass filter (LPF), suppresses the spurious generated by BPF over the wide out of band frequency range. An additional cover filter may be necessary for intermediate frequency rejection depending on the RF requirements. This solution, although simple in concept, is challenged by increasingly demand of very low-loss, reduced mass/footprint and stringent cost/schedule (i.e. no or little prototyping). The design technique described in chapter 3 has been employed to study the suitability of ridge waveguide filters to satellite IFA applications. Several C-band ridge filters have been designed and simulated for different bandwidths. As well, conventional modular structures (BPF+LPF) have been designed simulated [47] identical the ridge case.

4.1 SATELLITE PAYLOAD

In this work we are interested to understand the general structure of the RF payload of a generic satellite. A simplified block diagram is depicted in Fig. 45.

This scheme has to be read starting from left and proceeding towards the right. Below the list of the components:

INPUT ANTENNA It receives the signal from earth and it may be a parabolic or another type of antenna.

INPUT FILTER The main purpose of this filter is to select all the signals that the satellite has to receive, and also to prevent other undesired signals not into enter in the system.

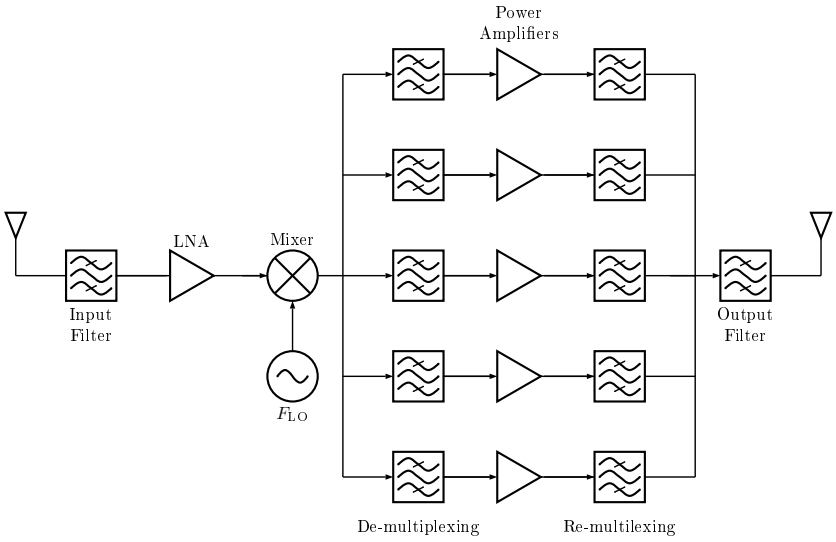

Figure 45: Simplified block diagram of a satellite RF payload.

LNA the low noise amplifier (LNA) is placed just after the input filter and amplifies the signal minimizing the noise.

DOWN CONVERSION This block translates to a local frequency f_{LO} the signal received. The block is presented as a combination of a mixer and an oscillator, but it may involve also other microwave passive components.

DE-MULTIPLEXER It is an array of bandpass filters that selects each channel for further processing. Depending on the project of the payload, they may be divided into even and odd channels.

POWER APLIFIERS Each arms has a power amplifier that permits the signal to reach the correct power level for being trasnsmitted.

RE-MULTIPLEXERS All the channels are then re-combined and transmitted at the desired carrier frequency.

OUTPUT FILTER Before the output antenna the output filter supresses spurius frequency components made in the previous stages like intermodulation products etc ...

OUTPUT ANTENNA It irradiates and phisically transmits the signal as an EM wave. Depending on the type of application, the output anntenna and the input antenna may be the same.

In Fig. 45 is possible to find two main parties that are the *low power* components and the *high power* components. The first one are those before the power aplifiers (input filter, LNA, down conversion, de-multiplexers) and then seconds are the power amplifies, the re-multiplexers and the output filter. The simplified block diagram of Fig. 45 only gives an overview of the RF payload system; depending on the design, many other microwave components like mixers, oscillators, filters and amplifiers may enter in that diagram. However, for our study Fig. 45 is useful in order to give a conceptual vision of the problem.

4.2 INPUT FILTER

The purpose of the *input filter* is to select, reject noise and to protect the system from undesired spurius frequency out of band. In many telecommunication satellites, all the trafic channel are transmitted in adjacent bands, so the input filter must select all the channals and removing noise. Thus the main properties of the first filter stage are:

1. large bandwidth,
2. high SFR,
3. minimized insertion loss (IL).

A lot of literature discusses the problem of bandwidth (BW) and many techniques for solving problem such as the frequency dipendence of inverters or the dispersion of the filter are suggested. Moreover, the IL is basically related to the conductivity and, generally, to the electric properties (ε, μ and σ) of the material constituting the filter. Thus it is possible to choose a material that minimize the IL.

Actually, in many telecommunication satellites, an *inductive iris* bandpass filter is employed for the input stage of the payload. These type of filters has been widely studied and their affidability is a standard for the common requirements for space components. For these filters, an usual prototype of $\lambda_g/2$ resonators with K inverters is not a good choice because it is not possible to meet the requirement of the SFR up to the second or the third harmonic. The out-of-band response of an inductive iris filter is shown in Fig. 47.

This figure shows the out-of-band response of a 4 resonators bandpass filter with inductive iris couplings. The central frequency of this filter is 6 GHz and the bandwidth is 100 MHz.

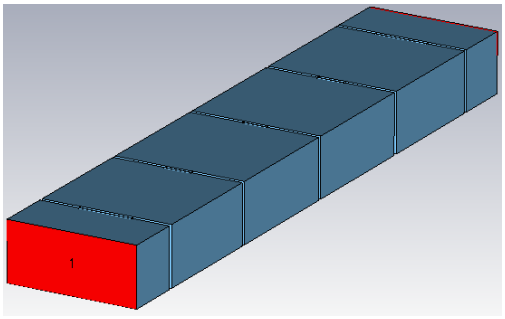

Figure 46: Inductive iris bandpass filter

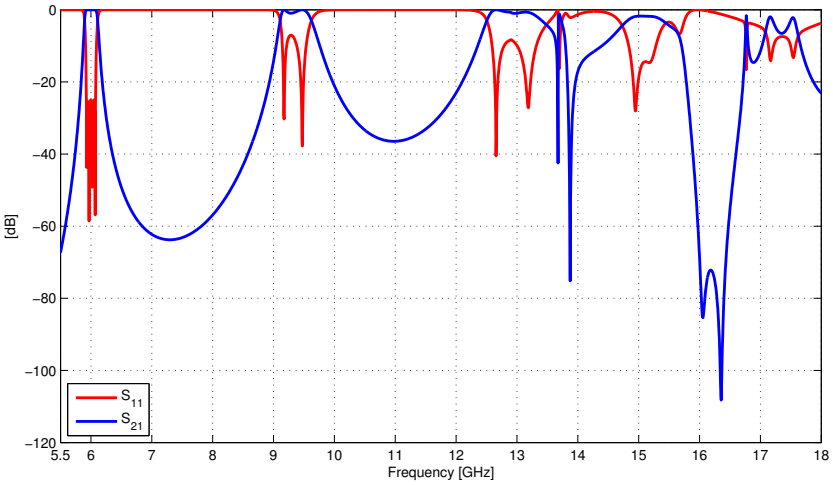

Figure 47: Out of band of a 4 poles inductive iris bandpass filter.

Repetition of filter depicted in Fig. 47 that theretically should be placed around $2f_0$ it can be found at 9 GHz ($1.5f_0$).

It is clear that this type of filter does not meets the specifications and another solution must be investigated. To avoid this problem in many satellite applications a *modular approach* is used. In order to satisfy the high SFR a *low pass* filter is cascaded after the bandpass one. In this way the lowpass filter cleans the undesired spurius repetition of the inductive iris filter. Thus the *input filter* is replaced by the cascading of a bandpass and a low pass filter as depicted in Fig. 48.

4.2.1 Lowpass features

The lowpass filter used in this study was choosen to have an assessment as realistic as possible, so a lowpass used for satellite applications at the ku-band was scaled to our range of frequencies. The shape of the lowpass filter is a rectangular corrugated

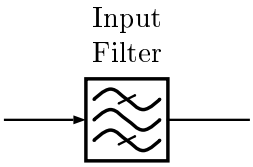

(a) Input filter

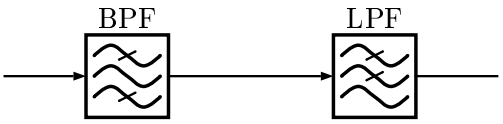

(b) Modular approach

Figure 48: Filters cascading

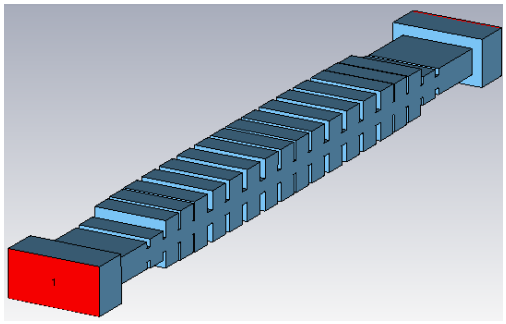

Figure 49: Lowpass corrugated filter.

waveguide with 28 dB of RL at central frequency and a cutoff placed at 6.5 GHz.

Fig. 49 shows the shape of the lowpass corrugated filter. The S-parameters for both in-band and out-of-band frequencies are shown in Fig. 50. The repetition of the filter is located above the 14 GHz. There features permit to have simulation that are very closed to real data in term of RL and IL. It has been measured that the insertion loss for this filter calculated at f_0 is:

Table 29: Lowpass filter insertion loss at f_0

Material	Insertion loss [dB]
Aluminum	-0.12324
Silver	-0.09627

4.2.2 Modular approach

The configuration of the cascading of the bandpass and the lowpass is shown in Fig. 51; the bandpass and lowpass are eas-

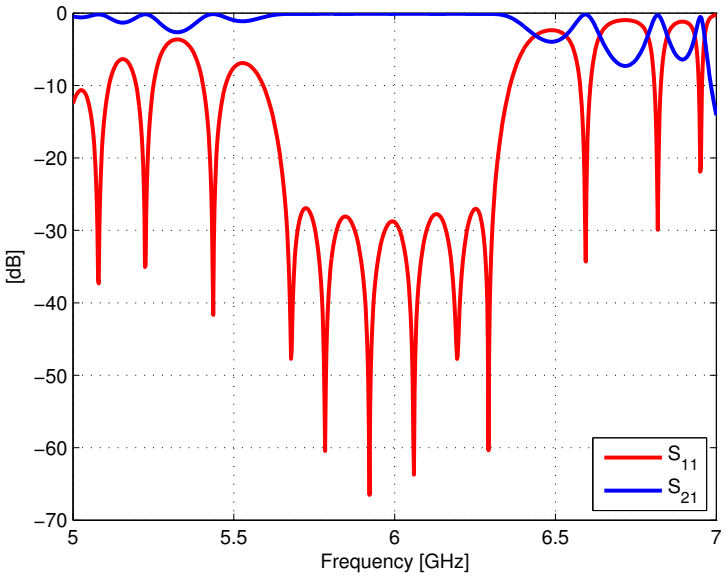

(a) In-band response

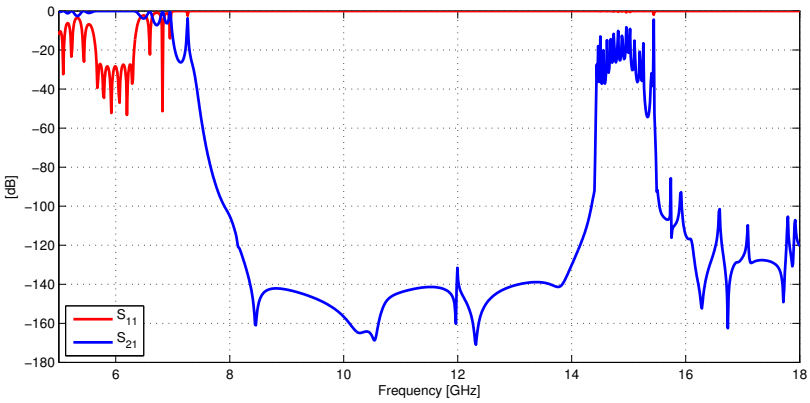

(b) Out-of-band response

Figure 50: Lowpass characteristic

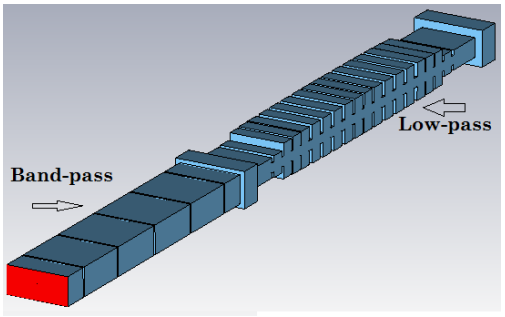

(a) Structure

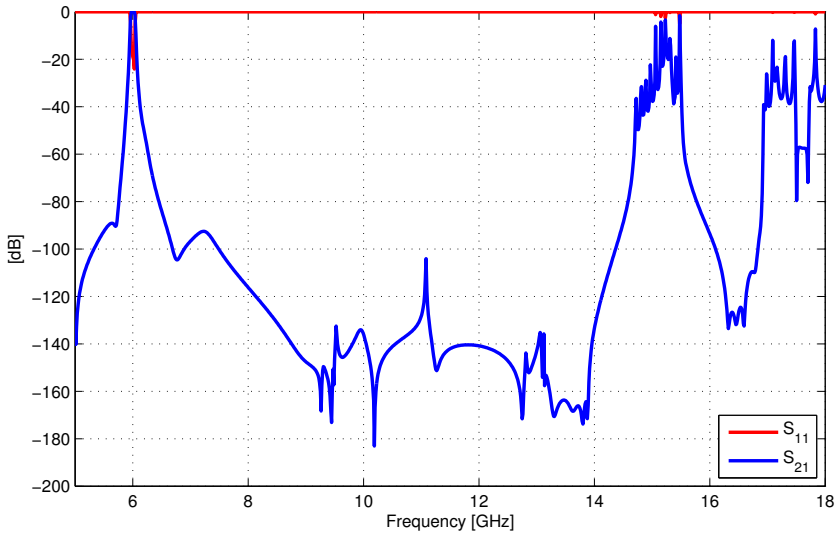

(b) Out-of-band response

Figure 51: Modular baseline

ily recognizable. This is the typical configuration used in many input filters in satellite RF payloads. The graph of Fig. 51b proves that the repetition of the baseline is above the second harmonic due to the rejection properties of the lowpass stage. Respect of a normal bandpass, this configuration has a greater size and weight, parameters of critical importance in the satellite payload. Fig. 52 gives an immediate view of the dimensions of both baseline and ridge and then, the advantage of the latter is more evident.

4.3 INSERTION LOSS TRADE-OFF

Once the traditional baseline cascading configuration has been described, is of interest to investigate if the ridge waveguide

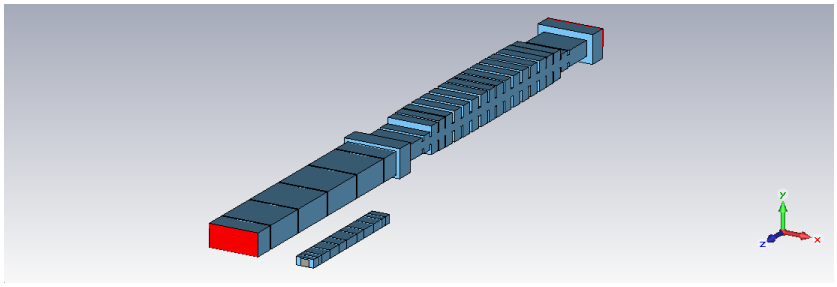

(a) Perspective view

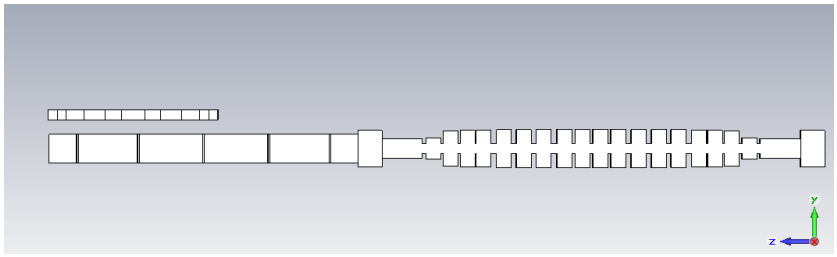

(b) Longitudinal view

Figure 52: Sizes of baseline and ridge

bandpass filter can replace the modular bandpass-lowpass layout. Looking at Fig. 35 is evident that the SFR is considerably improved if compared with the out of band characteristic of the common inductive iris bandpass filter of Fig. 47. First to begin in the comparisons between the two strategies, is necessary to check that the two tipologies have a SFR that is similar. In Fig. 53 the S_{21} parameters of the baseline and the ridge are put together. The spurius of the ridge is located at 14 GHz while the one for the modular filter is around 15 GHz. Nonetheless it is very difficult to have two filters with exactly the same spurius trend, so it can be assumed that the baseline and the ridge have the same spurius behavior.

A consequence of what has been stated in section 2.4 on page 20, the insertion loss is significantly increased in a ridge waveguide than a rectangular one. This means that also the IL of the ridge filter is worse than the inductive iris filter. It is well known by the theory [25] that the insertion loss of a filter *decreases* with larger bandwidth filters. Thus, it is necessary to investigate for which bandwidth the ridge filter could replace the modular approach; since the two configurations are similar in term of SFR indeed is necessay now to discover which is the best option from the profile of the insertion loss.

Using the synthesis techniques described in chapter 3, several ridge waveguide filters of different bandwidth have been

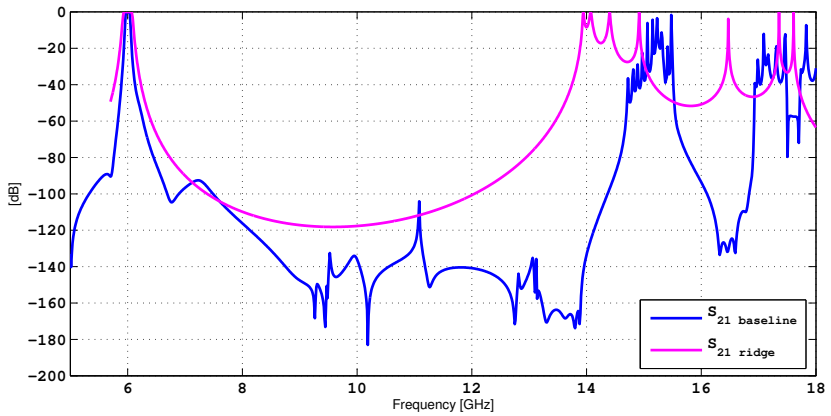

Figure 53: Through of baseline and ridge

Table 30: Insertion loss in dB of ridge filter evaluated at f_0

BW [MHz]	Aluminum	Silver
22	-2.530	-1.940
60	-0.950	-0.725
81	-0.720	-0.551
122	-0.490	-0.378
164	-0.380	-0.293
226	-0.290	-0.220
425	-0.170	-0.130
570	-0.140	-0.110

designed. In order to facilitate the work of the machinist, it has been decided to design the ridge filters at C-bands and, more precisely, at $f_0 = 6$ GHz. There were not followed strict specifications in term of selectivity of the filter, it was only decided to compare two classes of filter composed by 4 resonators and having SFR up to the second harmonic. The same has been for the modular baseline with the lowpass described in the paragraph 4.2.1 and with a inductive iris bandpass filter with the same number of resonators and same bandwidth. For these two category of filters has been calculated the IL at central frequency (f_0) with the formula (A.6). Once the number of resonators is fixed, it is very important to evaluate the IL of two filters having exactly the same bandwidth. In this way the same number of inductive iris bandpass filters has been designed with the help of the automatized procedure available in FEST^{3D} [1]. The lowpass filter remains the same for all the inductive iris bandpass filters.

Values of IL are listed for ridge filter and inductive iris filter respectively in tables 30 and 31. In order to have the total inser-

Table 31: Insertion loss in dB of inductive iris filter evaluated at f_0

BW [MHz]	Aluminum	Silver
22	-0.604	-0.452
60	-0.224	-0.167
81	-0.167	-0.128
122	-0.113	-0.088
164	-0.086	-0.068
226	-0.065	-0.052
425	-0.038	-0.032
570	-0.030	-0.025

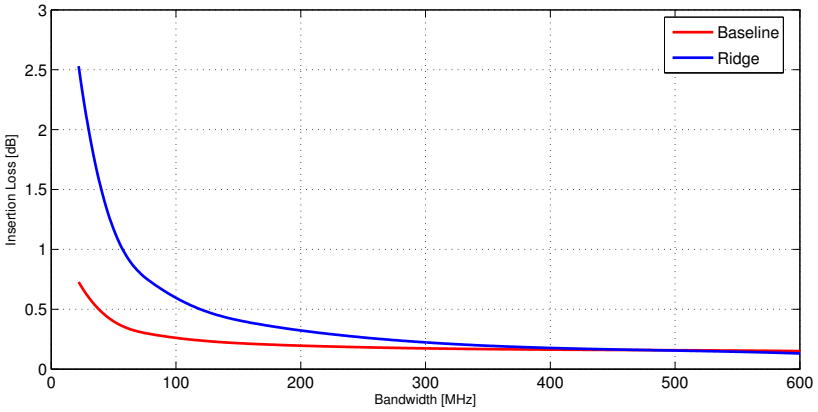

Figure 54: Changes of the insertion loss for ridge and modular baseline with respect to bandwidth for a 4 poles filter at $f_0 = 6$ GHz.

tion loss of the modular filter bandpass and lowpass, the contribution of the lowpass must be added. Thus, the insertion loss of the baseline is obtained adding to the values of table 31 the loss of the lowpass listed in table 29. By increasing the bandwidth the IL of the baseline, that is composed by the contribution of the bandpass and the lowpass (fix component), tends asymptotically to the IL of the lowpass.

Results of the insertion loss study are better understandable if presented in a graph. Fig. 54 shows the changes of the IL for both the ridge and the modular approach. For narrow bandwidths the losses at central frequency for the ridge are cosiderably high: -2.53 dB for the Aluminum and -1.94 dB if the material of the filter is Silver. The *new* observation that can be made from Fig. 54 is that by increasing the bandwidth the insertion loss of the ridge filter decreases faster than the baseline. There is a *cross-over* in which the IL of the ridge and the baseline are equal and, over it, the losses for the ridge are even better. Fig. 54

shows that already at 400 MHz the two curves are very closed to each others and with a cubic interpolation technique is possible to find the point of the cross-over, that is place at 480 MHz equivalent to the 8% of relative bandwidth. Curves of Fig. 54 refers to the Aluminum as material composing filters. Very conceptually identical results can be obtained with Silver: it can be easily shown that the trends of the insertion loss for the two layouts is the same, except for a uniform translation to lower values as consequence of the lower resistivity of Silver.

5 BREADBOARD MANUFACTURING AND MEASUREMENTS

In the six-months stage period at ESTEC the first part of the intership was dedicated to study the properties and characteristic of the ridge waveguide, to develop a synthesis method to get final dimensions of the filter, to study the state of art of the BPF plus the harmonic LPF standard configuration and to make a comparison with a ridge filter with similar RF characteristic while preserving spurious-free out of band rejection up to the second harmonic. The physical realization of a prototype of the filter was necessary in order to experimentally confirm the results obtained with the simulators and was also necessary to have te possibility to get in touch with physical and mechanical problems related to manufacturing process. After the building of the filter, it has been subjected to metrological measures and then to the RF measures at the ESTEC microwave laboratory.

5.1 MANUFACTURING OF RIDGE FILTER

In cooperation with the ESTEC machine shop was possible to build the ridge filter. Microwave filters are in general critical components, since they have to be lightweight and dimensionally stable. In addition, the stability in term of temperature and pressure must be guarantee. The metal surfaces need to perform excellent conductivity properties in order to avoid unacceptable resistive losses. A widely used technique is to put a very thin coating of high conductivity (σ) metal, such as silver, usually plating only the inner surfaces. In this case the dimensions of the filter must be reviewed in order to take into account the layer of plating material. Costs of such material have a great impact on overall the manufacturing process of the filter and sometimes is necessary to find a sort of compromise between the reducing of losses through the employment of a high conductivity material, and the total budget available. In our application, since it is not necessary to build a filter with optimized performaces regarding the insertion loss, was decided to make the filter in Aluminum. The choice to leave filter the filter without any silver plating was due to several aspects: budget, simplier manufac-

turing process, no need to change the internal dimensions to incorporate the silver coating and a reduced amount of time of building. Naturally the material involves only the losses of the filter and has no impact on the EM properties. When manufacturing a filter, industries guarantee the nominal values of the structure not to vary more than a certain value (*tolerance*). Therefore, filter performances are dependent on the suitable tolerance. Filters for on-board applications have to face very stringent requirements. Usually it is not possible manufacturing them to have the desired performance without post-production adjustments, thus tuning elements are often required. These provide extra sources of loss, and can generate leak radiation from inside to outside and vice versa. In this project this elements are *tuning screws* that are placed both in the transformer and at the top of the ridges. Screws of the transformer are able to adjust the RL response of the filter, while the screws over the ridges can correct the shift in frequency of its characteristic. Sample filters used for test and/or experimental applications usually do not need to be tuned, since they have to face less stringent requirements. However, in order to achieve accurate and reliable results, great care must be reserved to manufacturing processes.

5.1.1 Structural design

Manufacturing of the filter requires that a suitable structure is designed for both machining and interfacing with others microwave components. First of all was decided to build the filter in two parts of aluminum: the first one includes the whole ridge filter with transformer to standard rectangular waveguide, the second is the lid that closes the structure. The lid is a flat part of aluminum the closes the overall structure, indeed the filter has been designed consequently. The transformer has been aligned in order to present a common plane with the upper part of the ridge fitler so it is possible to close the structure without creating additional steps that could be very sensible during the manufacturing bringing to more error possibilities. This types of hollowed metal block structures can be connected each others with flanges at both ends. Practical reasons related to interfacing, testing and manufacturing requirements force the standardization of input/output waveguide and flange dimensions. In Fig. 55 is drown the layout of a WR-137 standard flange. A particular important are the values of dimensions of halls, positions and size of diameters. This data have been extracted from the *Maury Microwave Catalogue* and this information applies also to flanges of others manufacturers. In that figure is possible to ob-

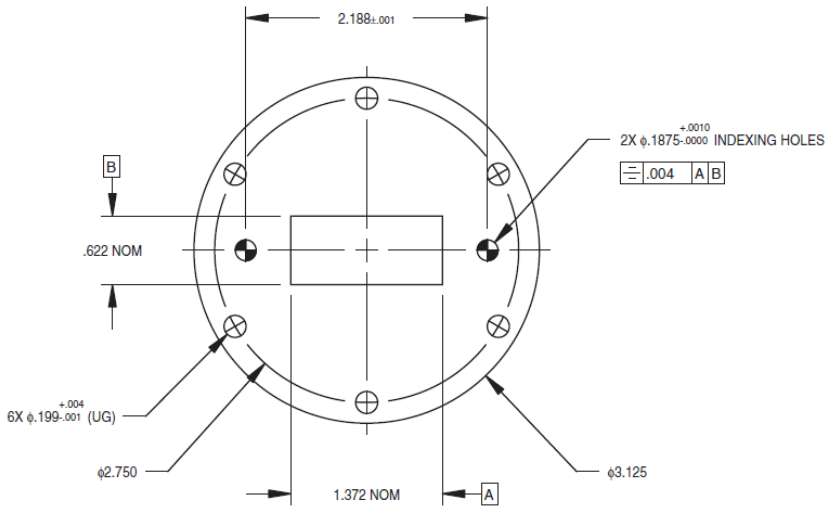

Figure 55: WR-137 standard flange

serve the presence of two alignment halls that allow to get fine calibrations. The total number of screws that will connect the transition to the ridge filter will be six.

Another very important topic that must be covered when building filter, is to assure that the lid is well closed with the bottom of the filter. To guarantee that the contact between the two surfaces is sufficient, the following strategy has been applied. Since the pressure is given by the formula

$$P = \frac{F}{A} \tag{5.1}$$

that is the force F over a surface of area A, in order to increase the value of pressure P with a given force F, is immediate that this can be done by reducing the total amount of contact area between the lid and the bottom of the filter. This strategy is called *high pressure flange* and allow to enhance the pressure and the contact between them.

Thickness of the wall of the filter has been choosen to be 5 mm. This dimension is suitable for inserting *mounting screws* ISO 4762 M2.5x10 HEXAGON SOCKET HEAD CAP.

In Fig. 56 there are all the computer-aided design (CAD) components necessary for the machining. It is possible to notice the halls of the mounting screws in 56a and the high pressure flage is obtained reducing the total surface of contact with the lid axactly as depicted in Fig. 56a. The lid (Fig. 56b) is a flat piece of aluminum where are placed the mounting screws; is of interest the division of the flange (Fig. 56c) in two parts. In addition, two wings are inserted in order to improve the contact and alignment

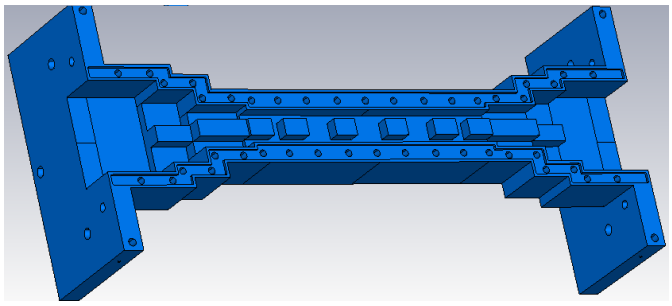

(a) Bottom

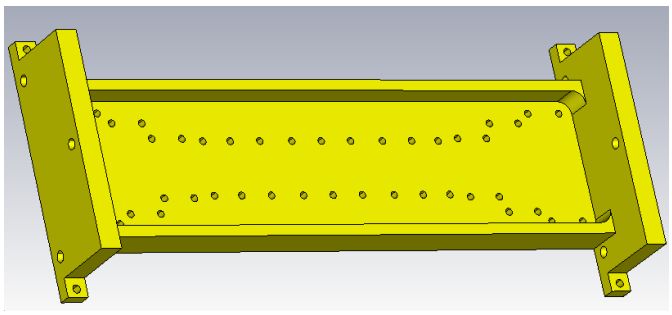

(b) Lid

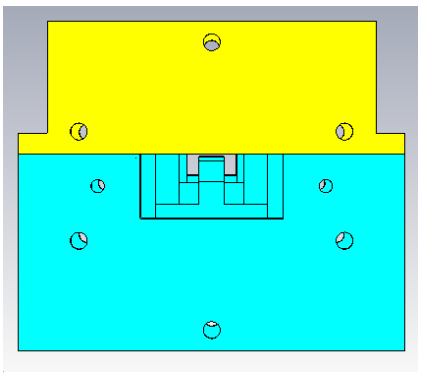

(c) Front and flange

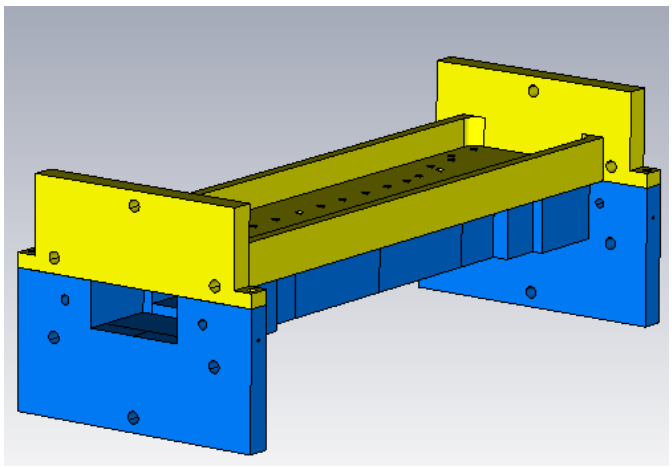

(d) Filter's structure

Figure 56: Ridge filter CAD model

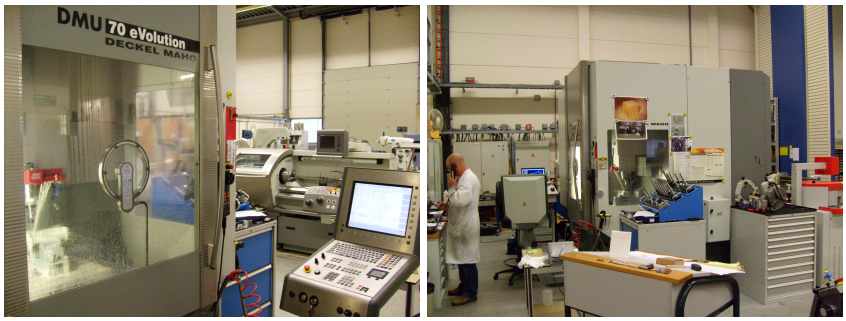

(a) (b)

Figure 57: Milling machine

between the two part of the flanges. Is important to remember that hollowed part composing the high pressure flange appears only in one of the two sides. As is possible to see in Fig. 56a a depression in the lower part of the filter (blue zone) means that the lid is completely flat.

5.1.2 Milling Machine

With the collaboration of ESTEC machine shop, the ridge waveguide filter has been machinined using the *milling machine*. This is a DMU DECKEL MAHO 70eVolution. With five NC axes, it is best suited for the high efficient 5-sided machining and 5-axes simultaneous contouring. The NC-swivel rotary table pivots the workpiece around its center of gravity and allows undercuts of up to 12 degrees. Thanks to the dynamic linear drive in the X-axis, the DMU 70 eVo linear reaches accelerations up to 1 g and rapid traverses up to 3149,6 ipm. With 18,000 rpm in the standard version and spindle options with up to 42.000 rpm. Pictures 57 show the milling machine used for this work. The tolerance of this machine is exstimated in 20 μm and the possibility to change the size of the mils permit to help making the job faster. Since our application does not need curved or round corners, only three axis (x,y,z) of the machine are used.

Starting from a CAD model, this machine will build the desired shape from a cube of aluminum for example. However, the artifact created by this machine is not always the same of the model also if we do not consider the tolerance error. In fact, the inner corners are rounded and this effect must be considered before the machining. In our ridge filter there are not inner corners except that in the transformer. It has been exstimated that the minimum diameter of the tool is about a third of the depth that

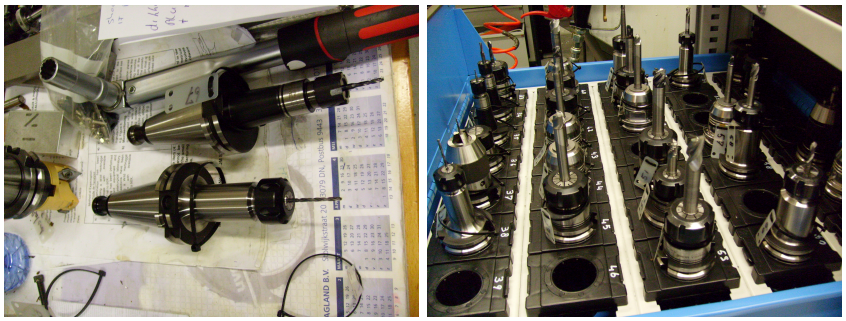

(a) (b)

Figure 58: CAT-40 toolholders

it is milling. For our transformer this means that a radius of 2 millimeters and 1.5 millimeters are inserted in ther inner corners of the first and second step. No radii are present in the ridge filter since all the corners are externals. The milling machine can change automatically one of the tools depicted in Fig. 58.

5.1.3 Yield anlysis

First of thinking to build a filter is necessary a yield analysis that permits to have a look over the impact of the tolerance errors of the manufacturing process on the scattering parameters of the filter. This can be done with the FEST simulator by performing a *tolerance* analysis. Every length that can be changed by the manufacturing process is added an error that can be fixed by the user. In our case, the tolerance of the milling machine has been exstimated in 20 µm so the simulator will add to all sensible lengths a random value of gaussian distribution of zero mean and 20 µm of standard deviation. At each iteration the simulator will change every sensible length by adding (or substracting) the original length with the random number. Once the errors are calculated the simulation is performed and the graphic is plotted. The loop continues for hundred of simulation and at end can show the impact of the tolerance errors of the building process. In Fig. 59 the yield analysis has been performed to the longitudinal dimensions of both ridges and evanescent inverters and also to the cross dimensions of the ridge. Fig. 59a shows the impact of the of the errors applied to all dimensions except for the gaps (the d dimension of Fig. 1 on page 15) while in Fig. 59b are considered also the errors over the gaps. It is evident that if the gaps would built correctly no great impact to the response of the filter is caused. In fact, no great changes are appreciable

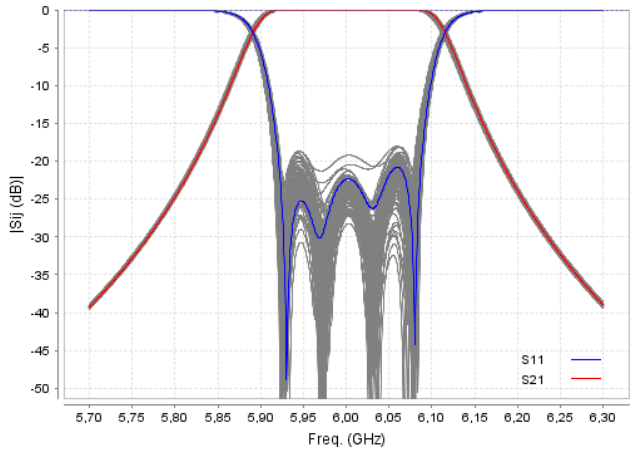

(a) Yield analysis without GAPs variation

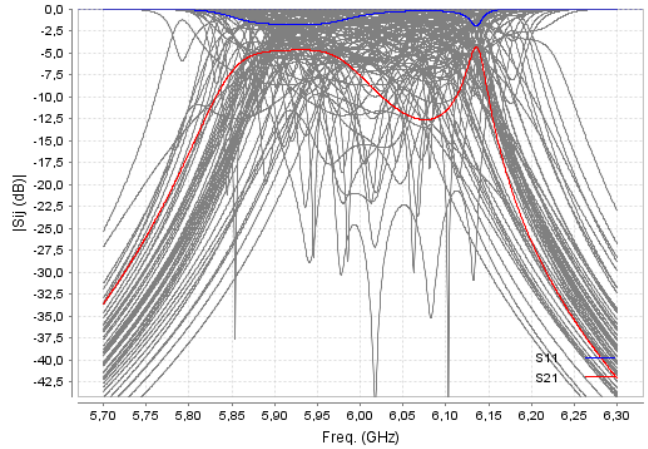

(b) All variables variation included GAPs

Figure 59: Yield analysis with 20 µm of standard deviation

and the the overall S parameters are quite similar to the original one. In the real life this situation is not practical because it is impossible that errors do not affect the dimension of the gaps. So we can conclude that this type of filter is very sensible to the manufacturing process and tuning screws will almost certainly be necessary. For this reason has been decided to build two lids. If the measurements will demonstrate that the response of the filter will not be good in term of return loss or central frequency, in one of the two lids tuning screws would be inserted. Moreover since the gaps have a fix dimension respect the lid, if they are built to large it is easy to put a screw to compensate the enlargement of the gap, but in the case of a reduction there are no ways to correct it. For this reason has been decided to increase

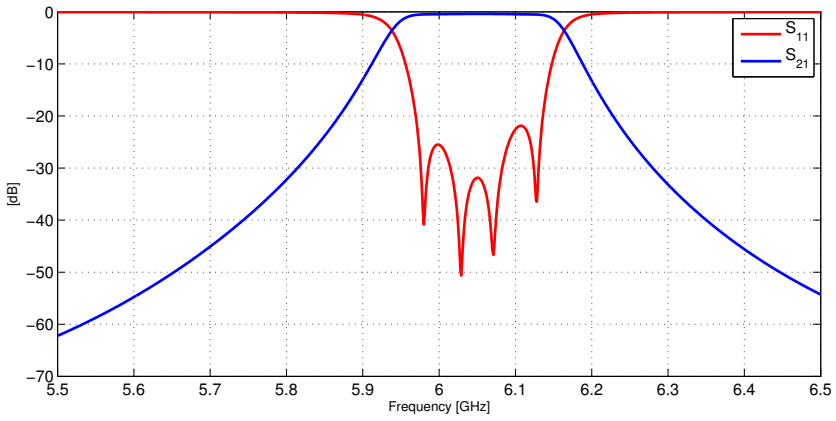

Figure 60: Response of the ridge filter after the increasing of the gaps of 20 µm. The characteristic is shifted and the return loss is not perfectly equiripple.

the dimension of the gaps by 20 µm in order not to have this type of problem. The consequences of the enhance of the gaps bring to a shift in frequency and to a variation of the RL. The results of these modifications are shown in Fig. 60. The shift in frequency is about 50 MHz up in frequency and the RL is not perfectly equiripple. However, these results are encouraging as they demonstrate that the final response is still a filter with characteristics similar to the previous.

The filter to be built was choosen among those at C-Band for practical reasons: at these frequency dimensions are greater and for the machine shop is easies to manufacturing it. Amid the C-band filter has been choosen the filter of Fig. 32 for its good S-parameter characteristics. The final dimensions listed in table 32 From table 32 the ratios are: $s/a = 0.45$ and $d/b = 0.1529$ so

Table 32: Cross-section of the modified ridge filter in millimeters

a	12.500
b	5.625
s	6.250
d	0.860

by looking graphs of chapter 2 is obtainde that $f_c = 5.095\,\text{GHz}$, $Z_{PV}(\infty) = 41.806\,\Omega$ and $Z_{VI}(\infty) = 39.252\,\Omega$.

Dimensions of the transformer are unchanged (see table 25) and the longitudinal dimensions of the ridge filter are summerized in table 33.

Table 33: Longitudinal dimensions of ridge filter

Element	Variable	Value (mm)
Couplings	l_{c1}	4.9702
	l_{c2}	11.6017
	l_{c3}	12.9767
	l_{c4}	11.6017
	l_{c5}	4.9702
Resonators	l_{r1}	9.7559
	l_{r2}	8.7594
	l_{r3}	8.7594
	l_{r4}	9.7559

5.1.4 Manufacturing Process

With the help of some pictures the manufacturing process of the ridge waveguide bandpass filter will be here described.

PREPARATION This filter will be built in aluminum so first a big slab of aluminum has been cut in order to obtain a block of desired dimensions suitable for the milling machine. These first steps are showed in Fig. 61. At the machine shop there are several layers of aluminum in the deposit (Fig. 61a), one of these was cut (Fig. 61b) to obtain the final block of Fig. 61c to be milled.

MILLING The block af aluminum is milled with several tools of different diameters. Figs. 62a and 62b show the milling. The model of the filter was imported in the CAD *Catia* program that is interfaced with the miller. The speed of the tool is normally around 18 000 rpm. The machinist sets and monitors all the steps in order to avoid collisions or other mistakes. An picture of the simulation was took during the process (Fig. 62c). A simulation of the entire machining process can demonstrate that all parameters setted are correct.

FINISHES The filter composed by the two parts has been assembled with the mounting screws and it is finally finished. In addition, a second lid was manufactured in case of tuning would be necessary. Fig. 63 show the final filter. To be notice the high pressure flanges in Fig. 63a and the alignment pins in the lid of Fig. 63b.

(a)

(b)

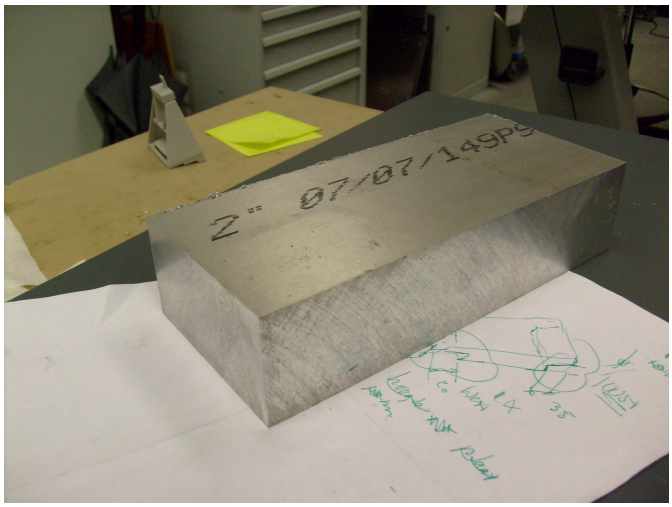

(c)

Figure 61: Preparation of Aluminum

(a)

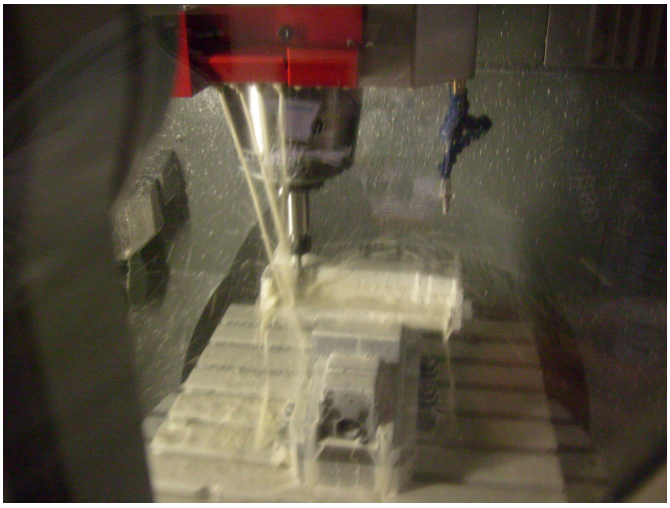

(b)

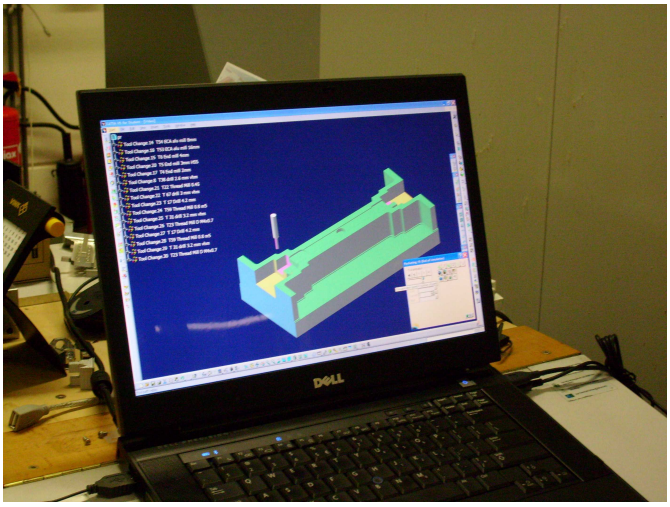

(c)

Figure 62: Milling

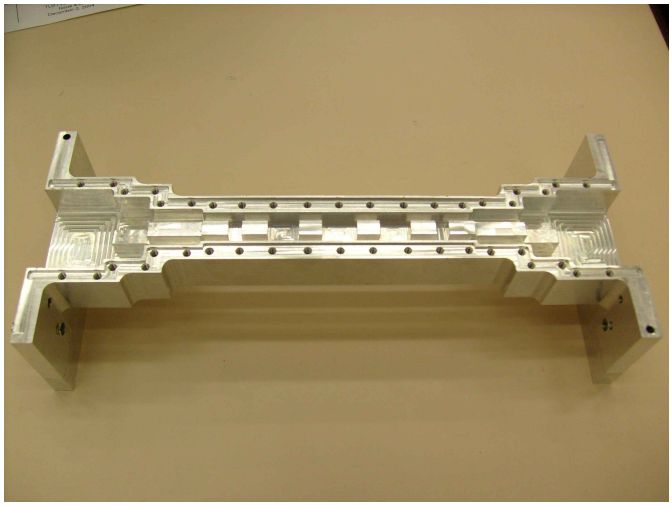

(a)

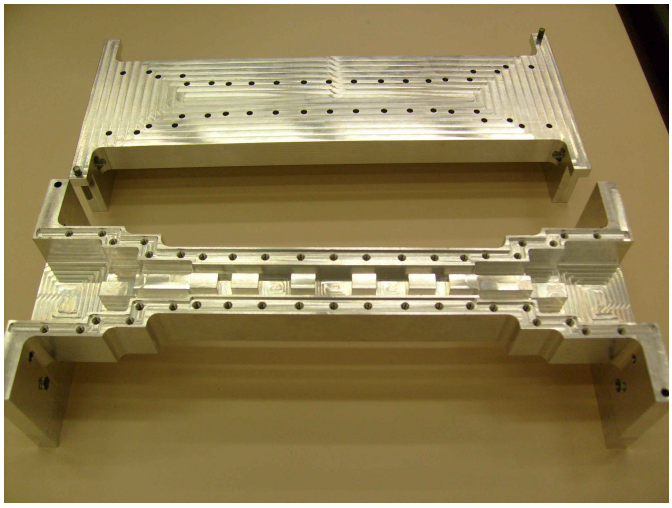

(b)

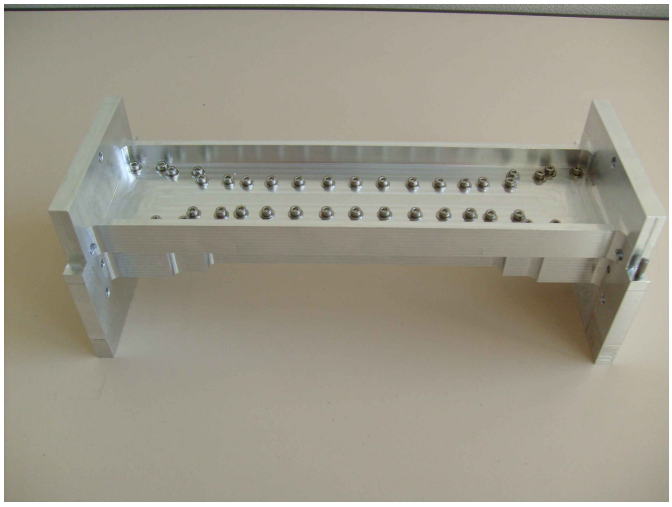

(c)

Figure 63: Ridge waveguide filter finished

5.2 MANUFACTURING OF TAPERS

Measuring the S parameters outside the band of the filter requires the use of correct adapters. In order to connect adapters for different bands, and consequently of different dimensions, is necessary to insert tapers between transitions and the input ports of the filter. As is possible to evince from Fig. 64, there was

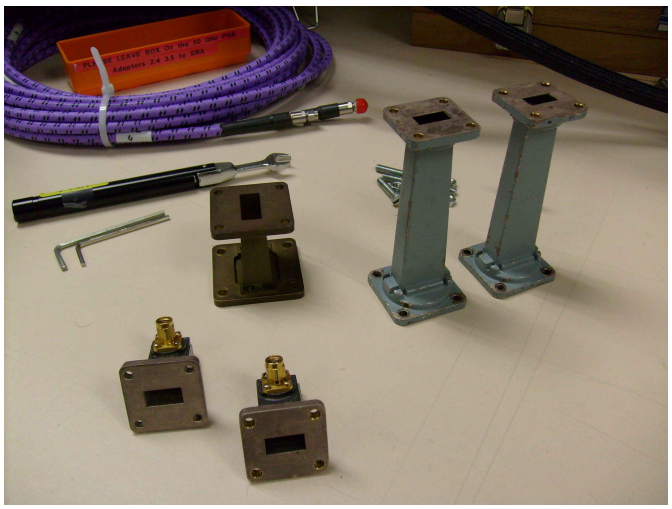

Figure 64: Adapters

only one taper from WR112 to WR90 instead of a couple. Since there were no other possibilities for perfoming the out of band measurements (see 5.4.3 on page 122) was decided to build a copy of the existing taper in aluminum by measuring its dimensions. The manufacturing process for the taper was very similar to one for the filter. Before proceeding with the building, a simulation of the VSWR of the taper was done in order to verify the correctness of the dimensions taken. The VSWR of the taper had been simulated and the result is depicted in Fig. 65. This graph demonstrates that the VSWR is less than 1.05 in the bands of interest. Afterwards the CAD model was created: the structure was divided in two parts in a very similar way of the filter. The upper part closes the bottom part with 6 mounting screws, 2 alignment pins and high pressure flanges to improve the contact between the two surfaces. The CAD model of the tapers is shown in Fig. 66.

Unlike for the filter, manufacturing of tapers requires the use of all the 5 axis of the milling machine. Fig. 67 summarizes the steps of the building. Is interesting to see in Fig. 67a how the system recoqnizes the dimensions of the block of aluminum with the help of a prope: the prope is composed by a ball at the

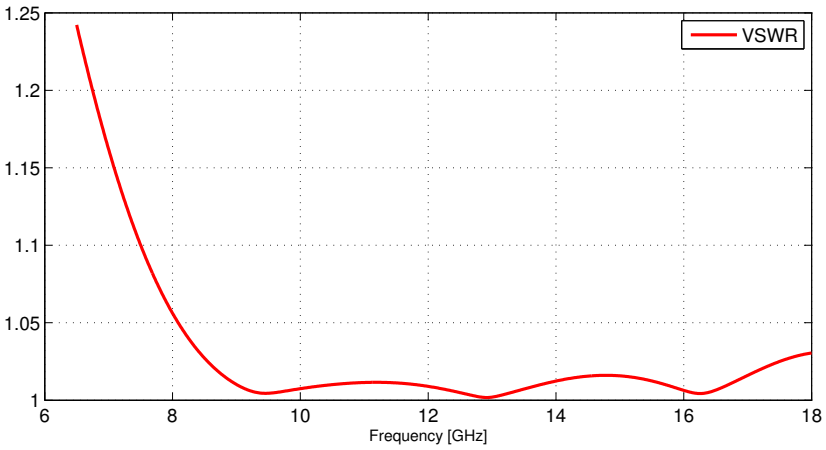

Figure 65: VSWR of the taper WR112-90

end of a shaft of very hard material. When the prope touches the block of aluminum the system stores the coordinates of this point and use them for further operations. It has been deciced to build 3 of these tapers in order to have 2 pairs together with the taper already owned at the laboratory. In Fig. 67b is showed a step of the building and in particular the bottom part of the 3 tapers. At the end, a final handwork (Fig. 67c) concludes the work and correct any inaccuracies.

At this point, the work of the machine shop is concluded and all the pieces producted there for the present work are shown in Fig. 68.

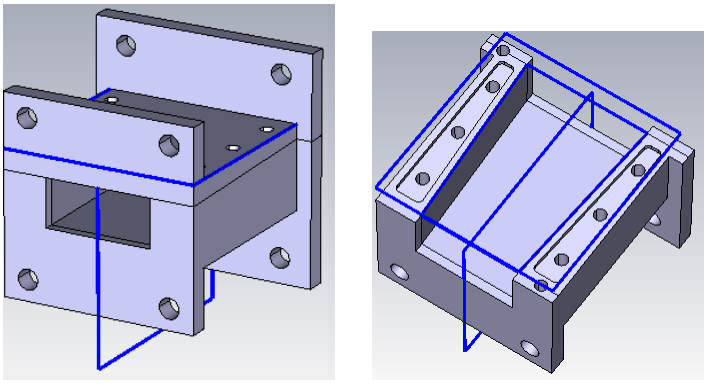

(a) Taper model **(b)** Bottom part

Figure 66: CAD model of tapers

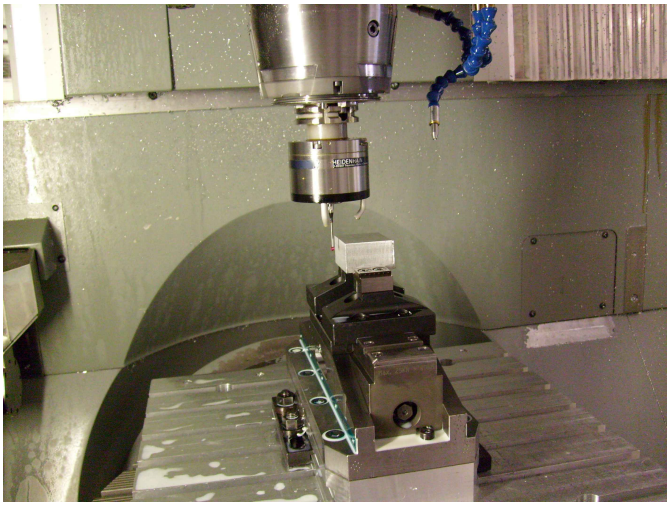

(a)

(b)

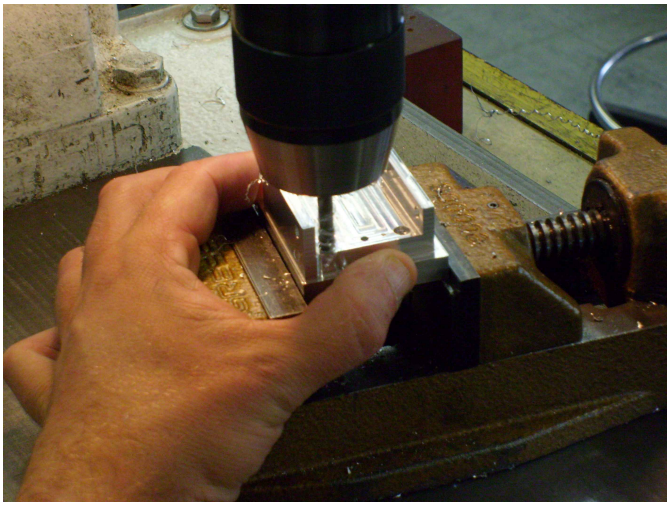

(c)

Figure 67: Tapers building

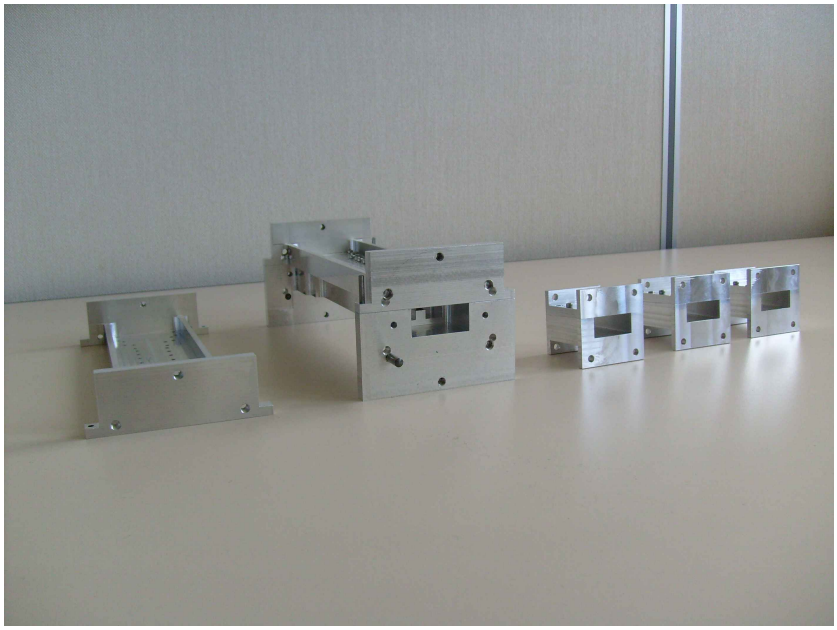

Figure 68: All components built

5.3 METROLOGICAL MEASUREMENTS

After the building of the filter is necessary to verify if the filter has been manufactured with the correct dimensions and to check if the errors are in accordance to the tolerance declared by the machine shop. The sensitiveness of the ridge filter has been showed in Fig. 59 and particular attention must be paid to the correctness of the gaps. For some parts of the filter the maximum tolerance of 20 μm is not enough and a higher precision is required. In order to appreciate dimensions which are the order of μm is necessary to perform a *metrological analysis*. This was done at the metrological laboratory at ESTEC. The laboratory is capable of performing a wide variety of optical and mechanical measurement techniques. The Metrology Laboratory performed on the 07/09/2010 and 08/09/2010 multiple dimensional measurements of the waveguide filter on the Mitutoyo Chrysta Appex Coordinate Measuring Machine at the temperature of $T = 20.5 \pm 1.0\,C^\circ$ and relative humidity $RH = 40 \div 60\%$. This is machine probes the object of interest and takes the 3D coordinates of the point it touches. The two pictures 69 show the Mitutoyo equipment. An example of this type of analysis is depicted in Fig. 70. The measurement uncertainty is defined based on the manufacturer's specification and for the following data is fixed in 2.95 μm. The following tables list the dimensions of all the components of the filter indicating for each the nomi-

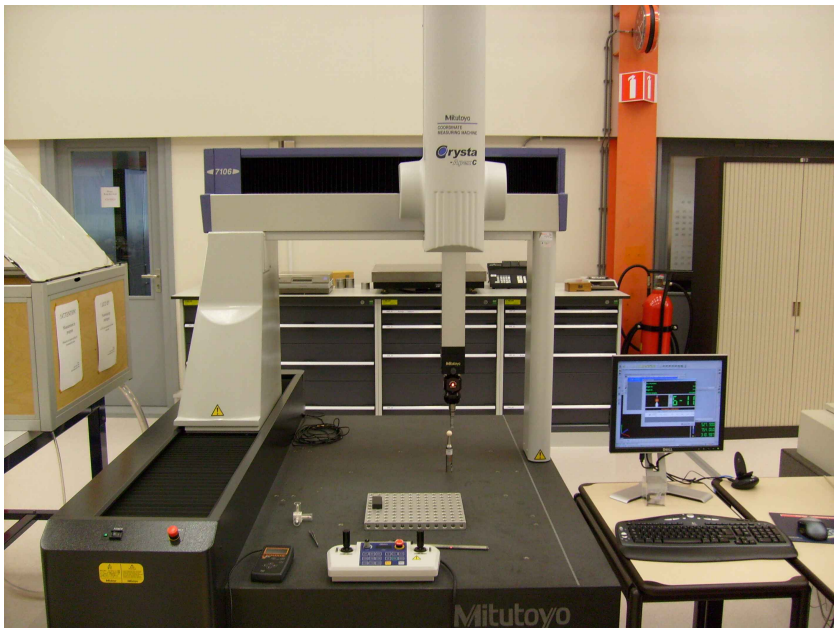

(a)

(b)

Figure 69: Mitutoyo Chrysta Appex Coordinate Measuring Machine

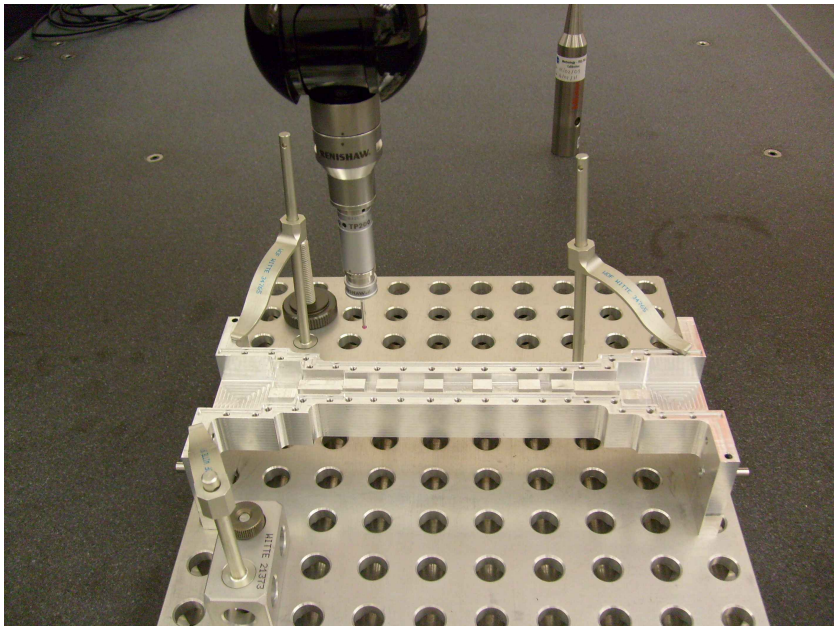

Figure 70: Metrological analysis of ridge filter

nal value and the deviation from it. Starting from the port 1 and proceeding towards the port 2, each part of the filter has been renamed as follow:

TRANSFORMER 1 Is the first step of the transformer starting from the rectangular WR-137 waveguide.

TRANSFORMER 2 Is the second step of the transformer, following *transformer 1*.

INPUT Is the input port of the ridge filter. It is a piece of ridge waveguide.

COUPLING k Is the k-th coupling.

RESONATOR j Is the j-th resonator.

OUTPUT Is the output port of the ridge filter identical to the input.

TRANSFORMER 3 Is the second step of the transformer at port 2.

TRANSFORMER 4 Is the first step of the transformer at port 2, the last before the standard WR-137 waveguide.

All the data in tables 34, 35, 36, 37, 38, 39 and 40 are expressed in millimeters.

Table 34: Height measurements with respect to top plane

Height of:	Nominal	Mean	STDV	DEV
Transformer 1	6.992	6.991	0.003	0.000
Transformer 2	1.761	1.758	0.006	−0.004
Input	0.860	0.862	0.001	0.002
Resonator 1	0.860	0.866	0.002	0.006
Resonator 2	0.860	0.868	0.001	0.008
Resonator 3	0.860	0.866	0.003	0.006
Resonator 4	0.860	0.864	0.003	0.004
Output	0.860	0.869	0.001	0.009
Transformer 3	1.761	1.759	0.005	−0.003
Transformer 4	6.992	6.987	0.002	−0.005

In all these tables, are presented the *mean* of the values measured. Every time the machine takes a measure, it has an uncertainty that is an error of normal distribution of mean zero and standard deviation (STDV) of 2.95 µm. So each measure is repeated in order to have a mean value which is the most possible accurate. After several measures is calculated a mean and these value are listed in the tables of this section. In addition, when calculating the distance between two planes, like in most our cases, is necessary to calculate a mean value because not in all cases the plane is perfect and looking to two simmetric points not always their distance is equal. Is also presented the deviation (DEV) from the nominal value. It is important that the values of deviation from the nominal value are minor or equal to the tolerance of 20 µm.

Particular attention is reserved for the correctness of the gap sizes and looking at table 34 it can be seen that the maximum variation from the nominal value of is 8 µm. This result is particularly encouraging because more the gap are precise, more are the probabilities not to have to use tuning screws. Is possible to explain that the deviation from the nominal value of the resonator's gap is so low because they are all equal and is particularly easy for the milling machine to achieve so high levels of precision.

The lengths of resonators, couplings and transformer of table 35 confirm that dimensions are in accordance with the tolerance declared by the machine shop. Only the *input* and *output* waveguide are excessively out of the target but luckily the length of this two pieces is arbitrary. Lengths of resonators are all minor respect to the nominal value. A shortening of the resonator

Table 35: Length measurements

Length of:	Nominal	Mean	STDV	DEV
Transformer 1	14.558	14.536	0.002	−0.022
Transformer 2	20.543	20.543	0.004	0.001
Input	9.756	9.923	0.006	0.167
Resonator 1	9.756	9.751	0.017	−0.005
Resonator 2	8.759	8.751	0.017	−0.009
Resonator 3	8.759	8.748	0.007	−0.012
Resonator 4	9.756	9.749	0.018	−0.007
Output	9.756	9.916	0.002	0.160
Transformer 3	20.543	20.543	0.004	0.001
Transformer 4	14.558	14.525	0.007	−0.033
Coupling 1	4.970	4.966	0.014	−0.004
Coupling 2	11.602	11.610	0.012	0.008
Coupling 3	12.977	12.986	0.013	0.009
Coupling 4	11.602	11.613	0.007	0.011
Coupling 5	4.970	4.967	0.010	−0.003

brings to a shift up in frequency, so it is possible that the final measure demonstrate a little shift of the central frequency.

Other measures confirm in most of the cases that the tolerance are satisfied. Errors in the transformer are less compromising with respect to the ridge filter or the gaps of resonators. There is an error between the lengths of the lid and the and the bottom part of the filter as demonstrated by table 40. This mismatch can cause problems when interfacing the filter with other microwave components or the transitions connecting to the vectorial network analyzer (VNA). The reason of this mistake is mainly due

Table 36: Width of ridge measurements

Width of:	Nominal	Mean	STDV	DEV
Transformer 1	6.250	6.287	0.013	0.037
Transformer 2	6.250	6.267	0.015	0.017
Input	6.250	6.283	0.027	0.033
Resonator 1	6.250	6.237	0.017	−0.013
Resonator 2	6.250	6.233	0.012	−0.018
Resonator 3	6.250	6.242	0.014	−0.008
Resonator 4	6.250	6.238	0.010	−0.012
Output	6.250	6.269	0.008	0.019
Transformer 3	6.250	6.250	0.006	0.000
Transformer 4	6.250	6.284	0.009	0.034

Table 37: Width of waveguide measurements

Width of:	Nominal	Mean	STDV	DEV
Transformer 1	27.500	27.500	0.024	0.000
Transformer 2	16.000	16.004	0.011	0.004
Input	12.500	12.479	0.009	−0.021
Resonator 1	12.500	12.496	0.003	−0.004
Resonator 2	12.500	12.499	0.007	−0.001
Resonator 3	12.500	12.500	0.002	0.000
Resonator 4	12.500	12.502	0.002	0.002
Output	12.500	12.490	0.003	−0.010
Transformer 3	16.000	15.995	0.012	−0.005
Transformer 4	27.500	27.484	0.014	−0.017

Table 38: Position of the centre measurements

Position of:	Nominal	Front	Back	DEV	
Transformer 1	10.625	10.625	10.606	0.000	−0.019
Transformer 2	4.875	4.884	4.882	0.009	0.007
Input	3.125	3.115	3.109	−0.010	−0.016
Resonator 1	3.125	3.140	3.140	0.015	0.015
Resonator 2	3.125	3.142	3.139	0.017	0.014
Resonator 3	3.125	3.141	3.134	0.016	0.009
Resonator 4	3.125	3.137	3.133	0.012	0.008
Output	3.125	3.116	3.117	−0.009	−0.008
Transformer 3	4.875	4.873	4.871	−0.002	−0.004
Transformer 4	10.625	10.587	10.603	−0.038	−0.022

to an error of calculating distances and reference planes of the milling machine. The lid and the bottom part derive from two separate blocks of aluminum so the machine had some problems in calculating the correct distances. This problem can be solved in the future by building both the lid and the bottom part of the filter on the same block of aluminum. In this way there are no uncertainties and the two pieces could have the same dimensions.

5.4 RF MEASUREMENTS

The characterization of our ridge filter has been made with the measure of the S-parameters at port 1 and 2. For measuring the scattering parameters a VNA device was employed. Tests have been conducted at the ESTEC TEC-ETM microwave laboratory

Table 39: Standard WR-137 waveguide measurements

	Nominal	Mean	STDV	DEV
WR137 1				
Width	34.850	34.906	0.001	0.056
Height	15.799	15.858	0.005	0.059
WR137 2				
Width	34.850	34.906	0.001	0.056
Height	15.799	15.855	0.003	0.056

Table 40: Envelope dimension measurements

Length of:	Mean	STDV
Bottom part	229.139	0.010
Lid	229.032	0.002

with an Agilent 8722ES Microwave Vector Network Analyzers. Normally only in-band measurements are required for characterizing the response of the filter. In our case is necessary to verify that the repetition of the filter is located around 14 GHz so an *out of band* measurement is required. The system is composed by the following parts:

- VNA
- coaxial cables
- coaxial to waveguide adapters
- device under test (DUT)

Fig. 71 is a schematic of the measurement system.

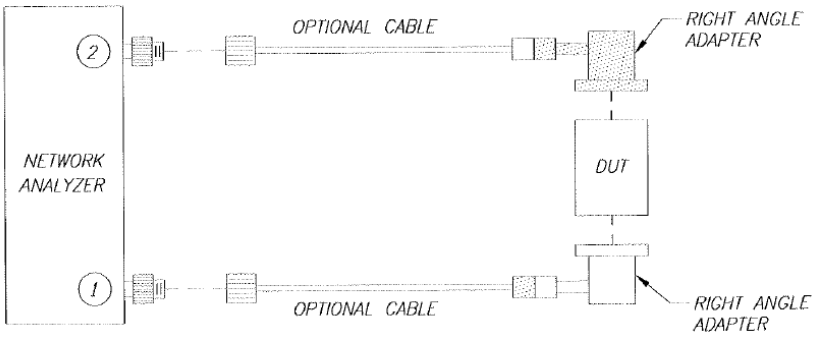

Figure 71: Measurement system

5.4.1 Calibration

Calibration of the VNA is a fundamental step to do before proceeding with the measures. A measurement calibration is a process which mathematically derives the systematic error model for the VNA. This error model is an array of vector error coefficients used to establish a fixed reference plane of zero phase shift, zero reflection magnitude, lossless transmission magnitude and known impedance. The array of coefficients is computed by measuring a set of known devices or calibration standards connected at a fixed measurement plane. When performing a two-port calibration, we have some choices based on the type of calibration standards we want to use. The two most common are:

1. short open load through (SOLT)
2. through reflected line (TRL)

Calibration kit available at the laboratory for the WR-137 waveguide required a TRL calibration method. TRL solves for the same 12 error terms as the more common SOLT calibration, but uses a slightly different error model and is especially useful for microwave, noncoaxial environments such as fixture, wafer probing, or waveguide. When requested by the VNA calibration process, the steps to be done are the following:

THROUGH also indicated with *thru*, is a measurement with the two transitions connected directly together;

REFLECTED is performed by putting a high-reflection standard at each adapter;

LINE a transmission line of known length and losses is inserted between the two adapters.

TRL calibration is computed initially at a reference plane that corresponds to the middle of the thru. In this case, the line standard can be assumed to be the portion of the line standard left over after subtracting a length equal to the length of the thru standard. After the error coefficients are computed, they are adjusted to establish a testport reference plane based on either the model of the thru standard or the model of the reflect standard. When selecting the reflect standard to set the testport reference plane, the assumption is that the reflect standard is precisely known as both magnitude and phase of the reflect standard will be used to compute the testport reference plane. Selecting the thru standard to set the reference plane obviously works for a zero length

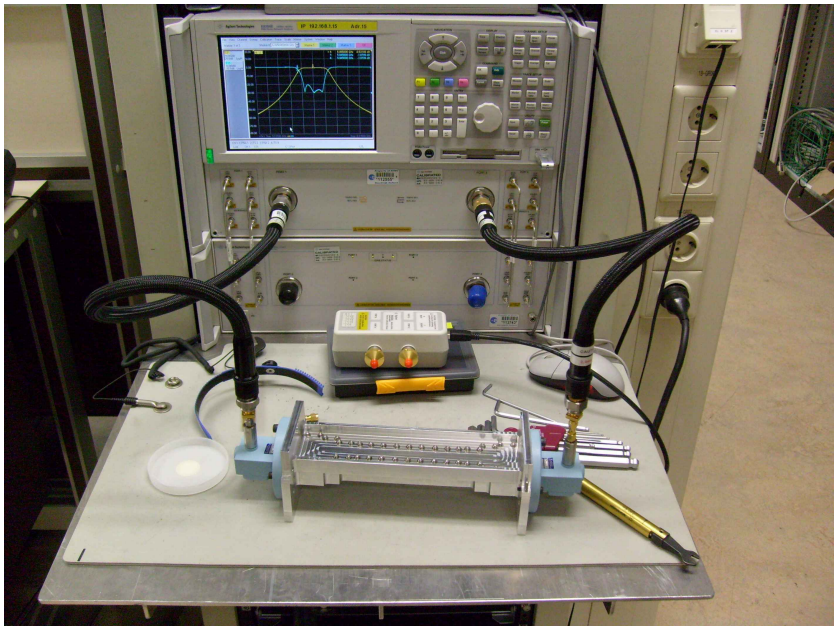

Figure 72: Filter under test

thru. In the case when the thru standard is a line with non-zero length, the model of the thru standard is used to compute the testport reference plane. In the case of coax or waveguide, using the model of the thru standard alone will provide excellent results.

5.4.2 In band

Once calibration has been performed everything is ready for the measurement. For the in-band measure the calibration was defined in the range $5.5 \div 6.5$ GHz. Fig. 72 shows the measurement of the filter. If the calibration was correct, we obtain immediately the response of the filter. Fig. 73a is the plot of the S-parameters measured by the VNA. These measurements refers to the ridge waveguide filter without any tuning screw, they are simply the response of the filter when connected with the device. This result is very encouraging because it shows that the RL of the filter is 20 dB for the worst case. There is not a complete symmetry in the structure caused by the building process that lead to $S_{21} \neq S_{12}$ at central frequency. This is produced by some asymmetries introduced by the manufacturing tolerance and by the error in the length of the lid highlighted by table 40. Anyway, for both sides of the filter S_{21} and S_{12} have a worst case of in band return loss of 20 dB. In Fig. 73b is showed in the same

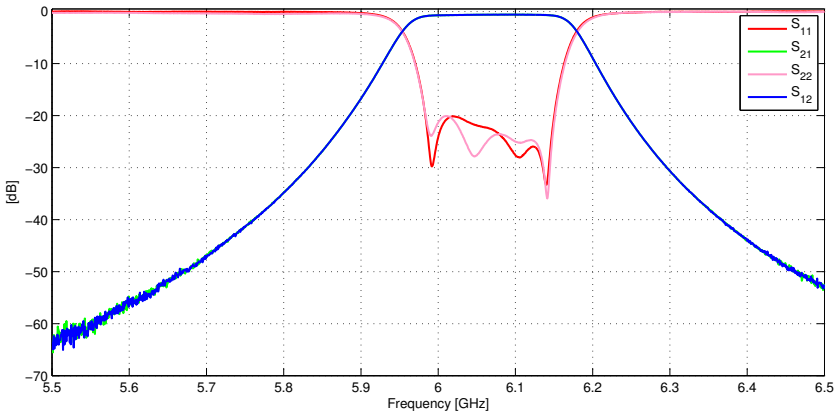

(a) Measurements

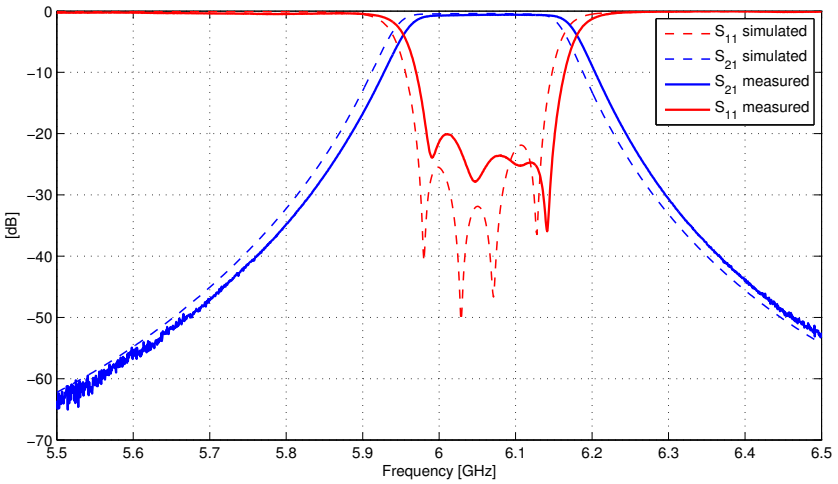

(b) Comparison between simulation and measures.

Figure 73: In band response of the filter

graph the response of the simulation and the measures of the filter. This figure confirm a very well accordance between them and only a shift of 10 MHz up in frequency was found. The results of the in band response of Fig. 73 assert that tuning is *not* required for our study. Taking into account the shift in frequency originated by the modifications at the gaps (Δ_{gaps}) and the tolerance errors ($\Delta_{tolerance}$), the new central frequency f_0' is given by (5.2).

$$\begin{aligned} f_0' &= f_0 + \Delta_{gaps} + \Delta_{tolerance} \\ &= 6\,GHz + 50\,MHz + 10\,MHz \\ &= 6.06\,GHz \end{aligned} \tag{5.2}$$

The insertion loss calculated at f_0' is -0.59 dB that is 0.2 dB worst than those simulated and listed in table 30.

5.4.3 Out of band

Out of band measurements are performed to verify that repetition of the filter is above the second harmonic. Due to the higher frequency and the dimension of the input waveguide of the filter (WR-137), in the range of frequencies $6.5 \div 18$ GHz the calibration of the transitions used for the in band measures is not appropriate. Outside the range of frequencies proper for the transition, the propagation is overmoded and the calibration is not possible. Depending on the range of frequency to be measured, the correct transition and calibration kit must be used. In order to cover the range of frequencies $6.5 \div 18$ GHz, the measures were splitted as the following:

1. $6.5 \div 10$ GHz with the WR-112 calibration kit
2. $10 \div 12.5$ GHz with the WR-90 calibration kit
3. $12.5 \div 18$ GHz with the WR-60 calibration kit

For each of the above bands, the relative TRL calibration was performed. The input port of the ridge filter is a standard WR-137 so in order to use others transitions are necessary tapers to connect them. At the microwave laboratory there were tapers between WR137-WR112, WR112-WR90 and WR90-WR60. Composing a chain of tapers made possible the measures untill the 18 GHz.

Unfortunately, in the laboratory there were not the compltete calibration kits for WR-90 and WR-60. For this reason the measure at frequencies above 10 GHz are less accurate due to the

not correct calibration. In Fig. 74a is the response of the filter up to 10 GHz; for doing this measurement the original WR-112 calibration kit with the correct calibration constants were used. Otherwise, no calibration constants have been found in the laboratory. The spikes of the S_{11} parameter above the 10 GHz that can be observed in Fig. 74b, are due to the calibration errors. In fact they are in contrast with the energy balance principle stated in A.3 on page 129. The measurement setup for the out of band is shown in Fig. 75. The relatively long chain of tapers itself introduces reflections and losses; the calibration process put the reference plane just after the two transitions so that all the mismatches and reflections degrade the quality of the measurement. Fig. 76 depicts all the measurement components (tapers, adapters ...) used in the laboratory. Although these spikes indicate the imperfection of the measure at these frequencies, for our investigation is important to see that the repetition of the filter is located around the 14 GHz and to confirm that the response is clean at least untill $2f_0$. Thus the parameter to look is the S_{21} and it gives the demonstration that repetition of the filter TE_{102} is exactly, as expected, at 14 GHz.

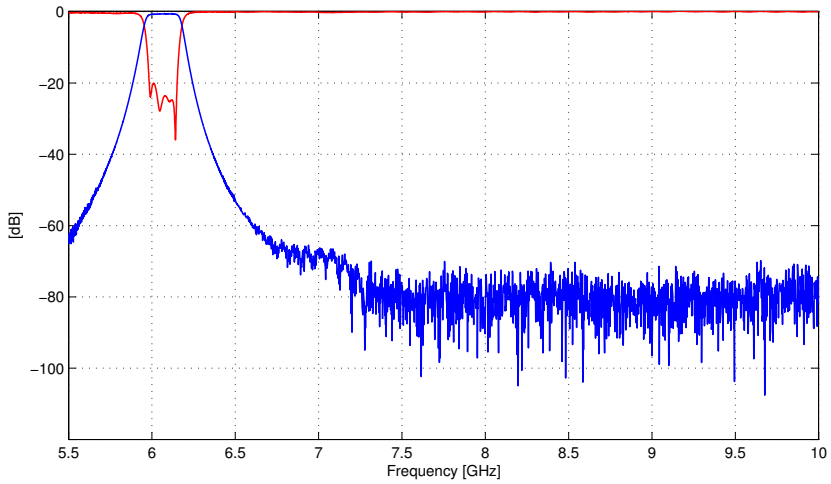

(a) Out band up to 10 GHz

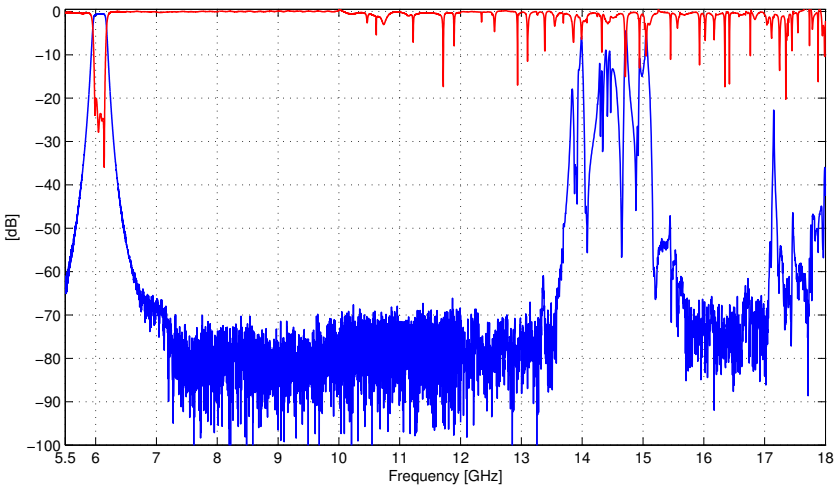

(b) Out band up to 18 GHz. The spikes of the S_{11} above the 10 GHz are due to the incorrect calibration.

Figure 74: Out band measurements

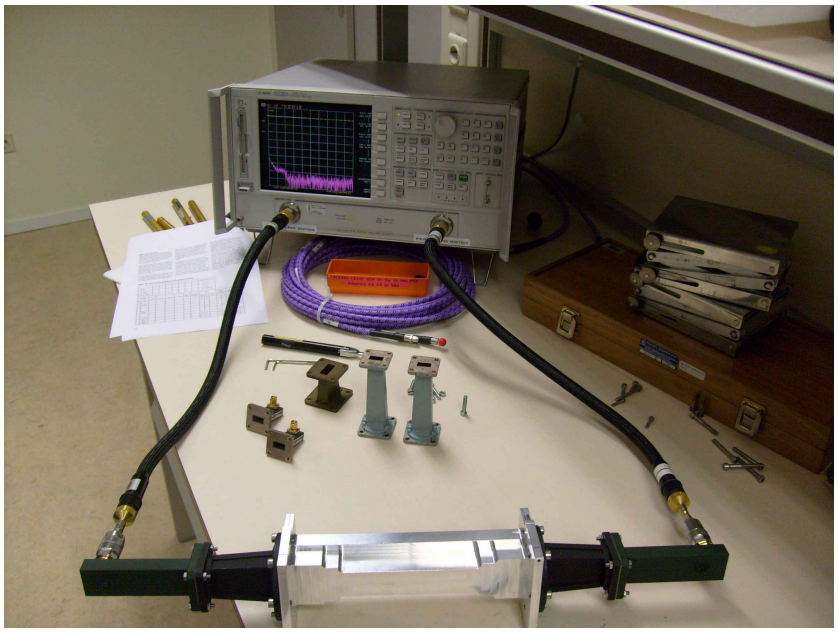

(a) Configuration for measurement up to 10 GHz

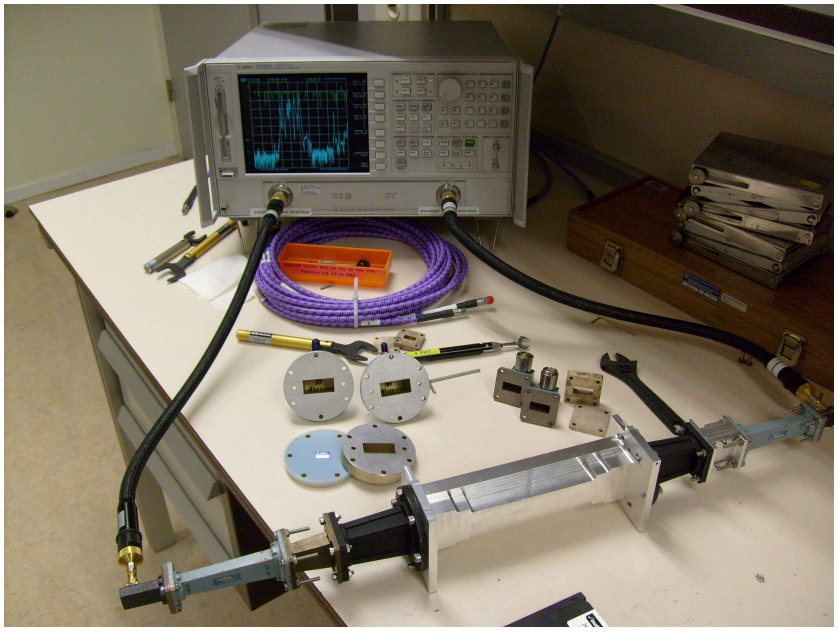

(b) Configuration for measurement up to 18 GHz. To be notice the chain of three tapers for connecting WR-60 adapter to WR-137 filter's input port.

Figure 75: Out band configurations

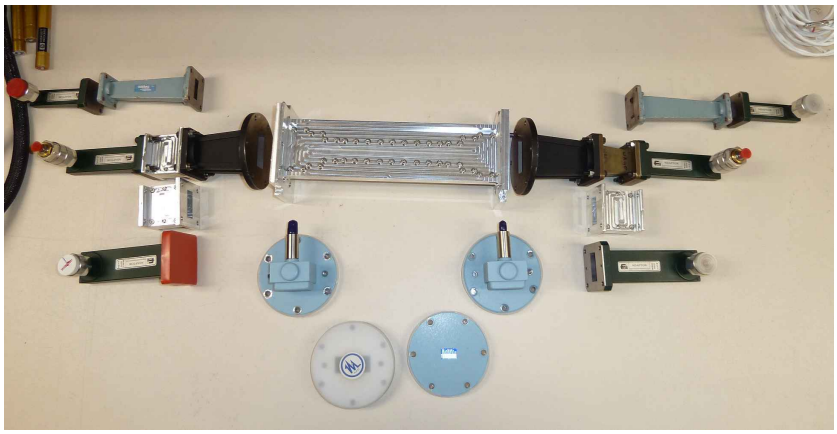

Figure 76: Microwave measurements components

6 CONCLUSIONS

In this work synthesis and applications of a ridge waveguide bandpass filter were presented. Performance of the ridge filter have been demonstrated to be in accordance with the specification of rejection beyond the second harmonic for both C-Band and Ka-band filters. The repetition of the filter in term of TE_{102} has been proved that it can be controlled by adjusting properly the ridge cross section. Dimension of the gap must be chosen by a compromise solution between the requirement of high spuriuos free range and low attenuation of the waveguide. Making this sort of trade off, ridge waveguide filters that meet low insertion loss characteristics and high out of band rejections have been showed. Two different techniques for the synthesis of the filter section have been proposed and described. Bandwidth problems that involved the first method is essentially caused by a wrong calculation of the slope parameter and consequently the values of K inverters. An explanation can be done when the distribution of the fields has been showed. The fundamental mode in the structure is not a pure TE_{10} but it looks like a TEM mode. Moreover, with the reduced length of resonators ($l \approx \lambda_g/10$) the resonance is not completed confinated in the ridge but is distributed also in the evanescent waveguide. This type of discussion was not implemented here and is a suggestion for a future development. The technique of Zaki for dieletric resonators was applied to the case of ridge resonators of our filter. It shows that for narrowband filters (ie. $w = 1\%$) this method gives directly final results with the exact bandwidth, while for wideband filter (ie. $w = 10\%$) a second step is needed.

The general block diagram scheme of a satellite payload system has been presented and the main requirements for the input stage filter were mentioned. The modular approach consisting of a cascade BPF and a LPF was described and compared with ridge waveguide filters designed with the methods presented in the chapter of synthesis. For the bandwidths of interest here, has been proved that the out of band rejection of the ridge has not changed significantly, so it is possible to affirm that for our investigation tha bandwidth does not affect the characteristic of the spuriuos. For this reason, even if the design procedure gives filters of an enalerged bandwidth, this is not critical for

our discussion because any comparison must be made at the same measured bandiwdth. If the application requires the exact bandwidth is possible to use method of Zaki presented here for the case of ridge, which allows to design filters with correct bandwidth specification. Price to pay for the Zaki method is the more computational time required and the needing for a second step of synthesis for wideband filters. The comparison with the IFA filter in term of insertion loss for several bandwidths was conducted and it showes the advantages of the ridge for *wide-bandwidths* over the classical modular approach.

A breadboard filter was built at the machine shop and both metrological and RF measurements were performed. In-band measurements demonstrated that the manufacturing process did not altered considerably gaps and the rusulting frequency response have -20 dB of return loss, meaning that no tuning is necessary. Out of band measures showed that the spuriuos properties of the ridge filter agree with simulations results.

Due to the nature of out-of-band response, better insertion loss for wider bandwidths, and the reduced size and mass storage with respect to the classical modular baseline, it is possible to conclude that ridge waveguide bandpass filters are good candidate for the input stage of a satellite payload.

A BASIC FILTER THEORY

A.1 DEFINITIONS

A filter is a passive two-ports device that performs a signal processing function for removing unwanted frequency components from the signal or to to enhance wanted ones. Generally, the signal comes from the port 1 and exits from 2 like shown in Fig. 77.

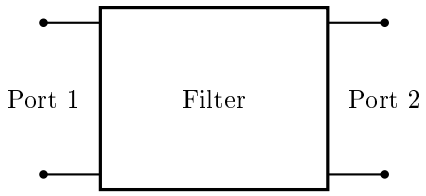

Figure 77: Network view of the filter

For any N-port junction is possible to define the scattering matrix $\mathcal{S}$ that for the filter of Fig. 77 is reduced to matrix (A.1):

$$\mathcal{S} = \begin{bmatrix} S_{11} & S_{12} \\ S_{21} & S_{22} \end{bmatrix} \tag{A.1}$$

By considering a symmentrical structure the following condition is satisfied:

$$S_{21} = S_{12} \tag{A.2}$$

In a first study a lossless situation is considered: all conductors are PEC and under this hypothesis is always true that the total energy can only pass through the junction or it can be reflected:

$$|S_{11}|^2 + |S_{21}|^2 = 1 \tag{A.3}$$

By an ideal point of view, filters may be divided in different typologies:

- Lowpass filters
- Highpass filters

- Bandpass filters
- Stopband filters

An ideal low-pass filter completely eliminates all frequencies above the cutoff frequency while passing those below unchanged. Its response is a rectangular function in the frequency domain and a cardinal sinus in the time domain Fig. 78. Highpass has

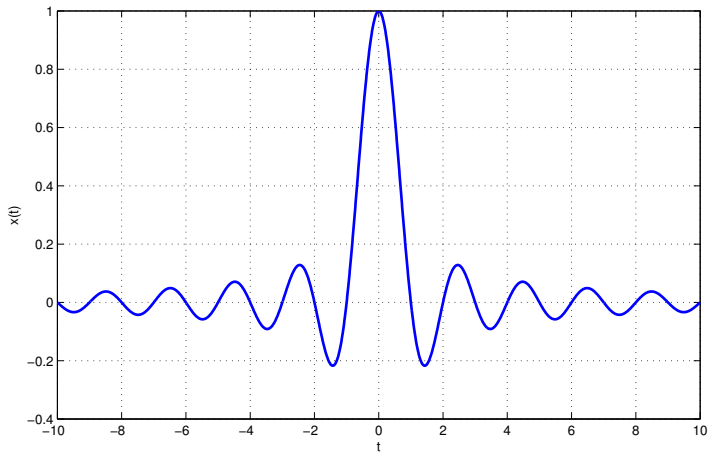

Figure 78: Time domain response of ideal lowpass filter

the opposite behaviour because it allows high frequencies to be transmitted to the output port. Bandpass filters are designed to transmit to the output port only a restricted range of frequencies defined between two frequency points. Stopdband is the dual filter of the bandpass while it does not affect all the frequencies except for a specified range of frequencies. Fig. 79 summarizes the ideal frequency responses of the four major filter typologies.

Is common to consider the variation with frequency of the IL, defined as the ratio between the power P_0 available at the generator and the power P_L transfered to the load. Normally this ratio is expressed in dB by:

$$A|_{dB} = 10 \log_{10} \frac{P_0}{P_L} \tag{A.4}$$

Sometime is possible to find the notation L_{ar}: this symbol represents the peak attenuation in the bandpass spectrum and so it has an equivalent meaning with definition (A.4).

In Fig. 80 is drown the S parameters of a symmetric 5 poles Tchebycheff bandpass filter. Looking this image the *bandwidth* is defined like the interval of frequencies where the S_{11} parameter is less then or equal to a certain prescribed valued called RL.

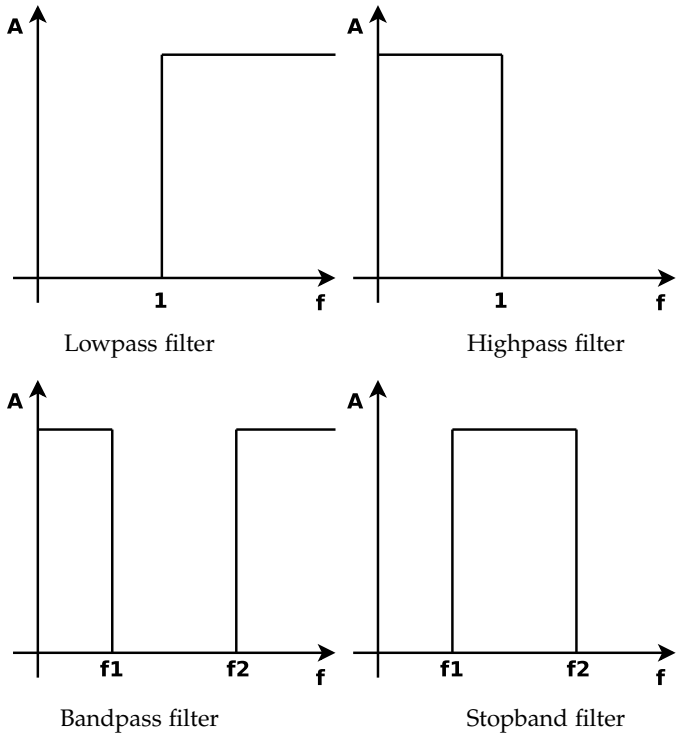

Figure 79: Frequency response of ideal filters

The two extreme frequencies where the $S_{11} < RL$ are defined, respectively, f_1 and f_2. The bandwidth is defined as:

$$B = f_2 - f_1 \tag{A.5}$$

The IL is defined as the worst case of magnitude S_{21} in the bandwidth and in dB is expressed as

$$IL = 20 \log_{10} |S_{21}| \tag{A.6}$$

In some comparative studies is possible to evaluate the IL at f_0.

In practical cases in the bandwidth range of the filter, the reflections caused by the ripples of the return loss are so small that are trascurable if compared with the losses of the material componing filters.

The order of the filter is the number of resonators that it is composed and consequently the number of poles: from Fig. 80 the resonators are identified as the zeros of the RL within the bandwidth.

Another important parameter is the *out of band rejection* that is the behaviour of the filter outside the bandwidth.

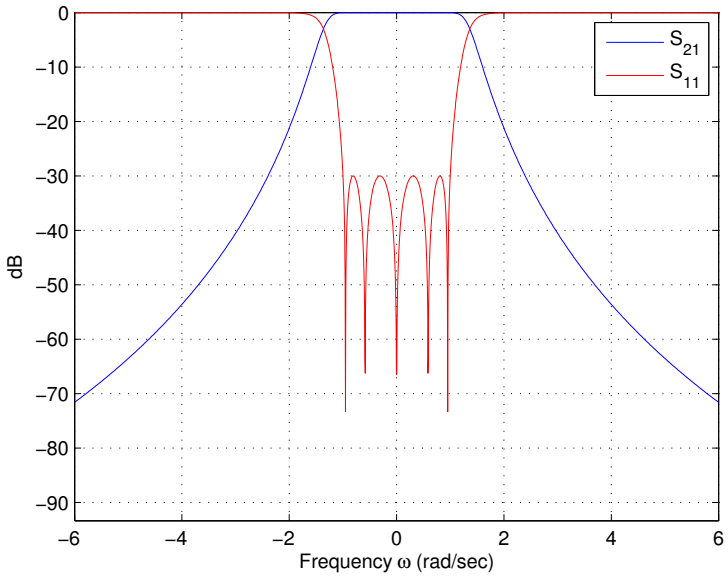

Figure 80: A five poles Tchebycheff bandpass filter

A.2 LOWPASS PROTOTYPE

Filter design theory begins with the definition of the attenuation A function of frequency accordingly with the specifications.

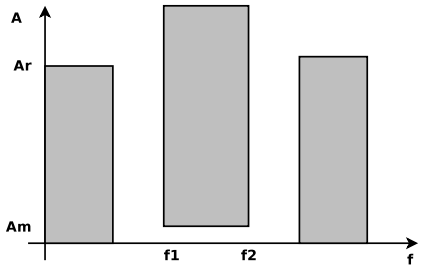

Figure 81: Design attenuation mask

In Fig. 81 is depicted the boundary of attenuation among the different frequencies. In particular the minimum outband attenuation A_R and the maximum inband attenuation A_m are here defined. The characteristic of the filter must be in accordance with this specifications.

Design method consists initially to consider a lowpass filter prototype structure that is a passive, reciprocal, normally lossless two-port network which is designed to operate from a 1Ω generator into a 1Ω load. The network response has a lowpass characteristic with its band-edge frequency at $\omega' = 1$. Since the

network is normally lossless there is no need to specify the passband insertion loss since this is related to the return loss by (A.3) unitary condition.

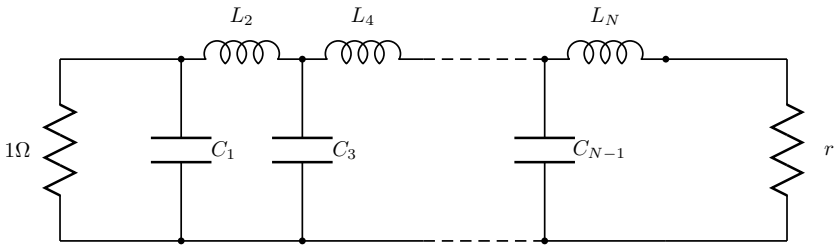

Figure 82: Lowpass prototype.

A model of the lowpass filter [10] is shown in Fig. 82. The last element is a shunt capacitance if N is odd, and series inductance if N is even. The number of capacitors and inductors increase the selectivity of the filter and with $N \to \infty$ its frequency response tends to those of Fig. 79. The highpass prototype is the dual of Fig. 82 and simply the capacitors and inductors are exchanged like shown in Fig. 83.

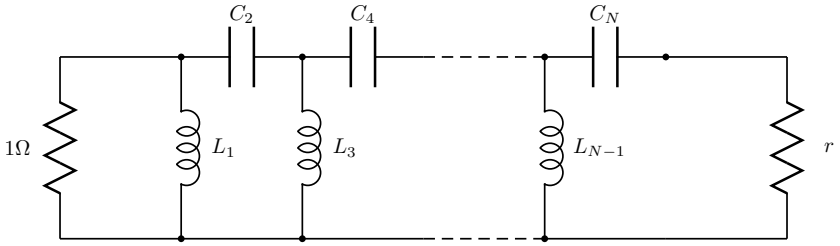

Figure 83: Highpass prototype.

The frequency of the normalized lowpass prototype is indicated with ω' and the lowpass cutoff with ω'_1. For convenience, the following conditions are assumed:

1. the passband edge occurs at $\omega'_1 = 1$
2. the left-hand load resistance is 1 Ohm
3. the first element is a shunt capacitance for the lowpass and a shunt inductance for the highpass.

The values of C_i and L_j of Fig. 82 are chosen in order to obtain the desired attenuation characteristic. Is common to assign to shunt capacitors values $g_1\ g_3\ g_5 \cdots$ and to series inductances $g_2\ g_4\ g_6 \cdots$. Maximally flat, Tchebycheff and Elliptic polinomial are widelly used in common applications.

A.2.1 Maximally flat prototype

The maximally flat or *Butterworth* approximation is the simplest meaningful approximation to an ideal lowpass filter. The behaviour of the attenuation in the frequency normalized lowpass domain ω' is given by:

$$L_{ar} = 10\log_{10}(1+\omega'^{2N}) \tag{A.7}$$

where N is the order of the filter and its caracheristic is show in Fig. 85.

Depending of specifications of the attenuation mask of Fig. 81 the number of resonators is given [25] by

$$N \geqslant \frac{A_m|_{dB} + A_R|_{dB}}{20\log_{10}(x_c)} \tag{A.8}$$

The values of g_i parameters for the Butterworth polinomials are calculated by formulas:

$$g_0 = 1 \tag{A.9a}$$

$$g_i = 2\sin\left[\frac{(2i-1)\pi}{2N}\right] \quad i = 1,2,\cdots,N \tag{A.9b}$$

$$g_{N+1} = 1 \tag{A.9c}$$

A.2.2 Tchebycheff characteristic

In this project the Tchebycheff polinomial characteristic is used for the design of the filter because it has the advantage of a better out-of-band rejection and the equiripple return loss can be easely controlled. In the normalized lowpass prototype ripples vary between two values in the passband up to the band-edge at $\omega' = 1$. The insertion loss is given by

$$IL = 10\log_{10}[1+\varepsilon^2 T_N^2(\omega)] \tag{A.10}$$

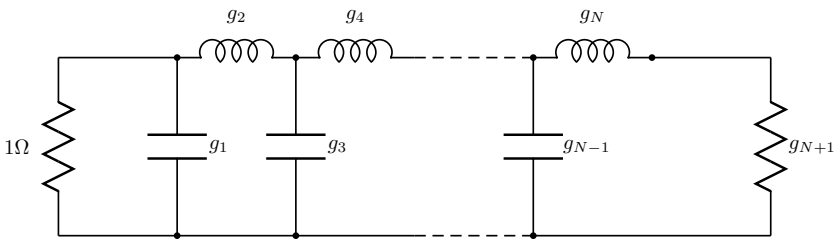

Figure 84: Lowpass prototype with g_i constants.

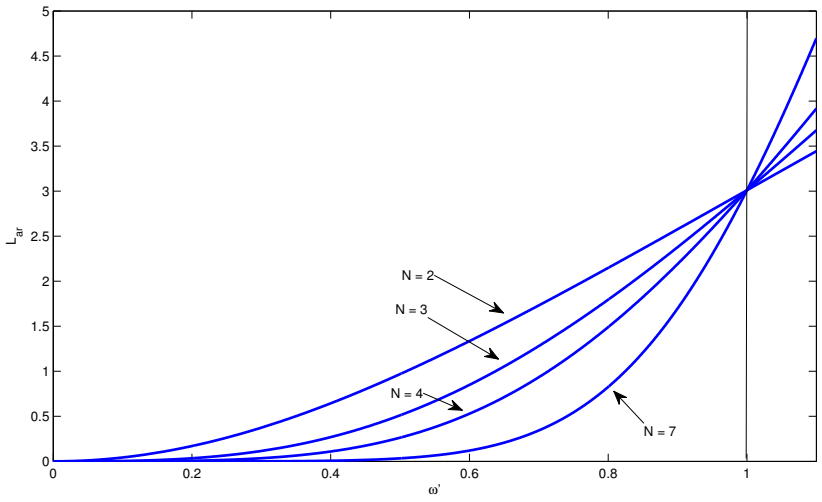

Figure 85: Maximally flat characteristic

The response is equiripple, resistor terminated at both ends, the element values may be computed as follows:

$$\begin{aligned} \beta &= \ln\left(\coth\frac{L_{Ar}}{17.37}\right) \\ \gamma &= \sinh\left(\frac{\beta}{2N}\right) \\ a_i &= \sin\left[\frac{(2i-1)\pi}{2N}\right] \\ b_i &= \gamma^2 + \sin^2\left(\frac{i\pi}{N}\right) \end{aligned} \tag{A.11}$$

where L_{Ar} is the peak of attenuation in the bandpass. After calculating parameters (A.11) the g_i values are obtained as:

$$\begin{aligned} g_1 &= \frac{2a_1}{\gamma} \\ g_i &= \frac{4a_{i-1}a_i}{b_{i-1}g_{i-1}} \\ g_{N+1} &= 1 \qquad \text{for N odd} \\ &= \coth^2\left(\frac{\beta}{4}\right) \qquad \text{for N even} \end{aligned} \tag{A.12}$$

In order to choose the attenuation characteristics, it is necessary to value the degree of the filter N and the coefficient ε, which is a parameter connected to the insertion losse ripple L_{Ar}:

$$\varepsilon = 10^{\frac{L_{Ar}}{10}} - 1 \tag{A.13}$$

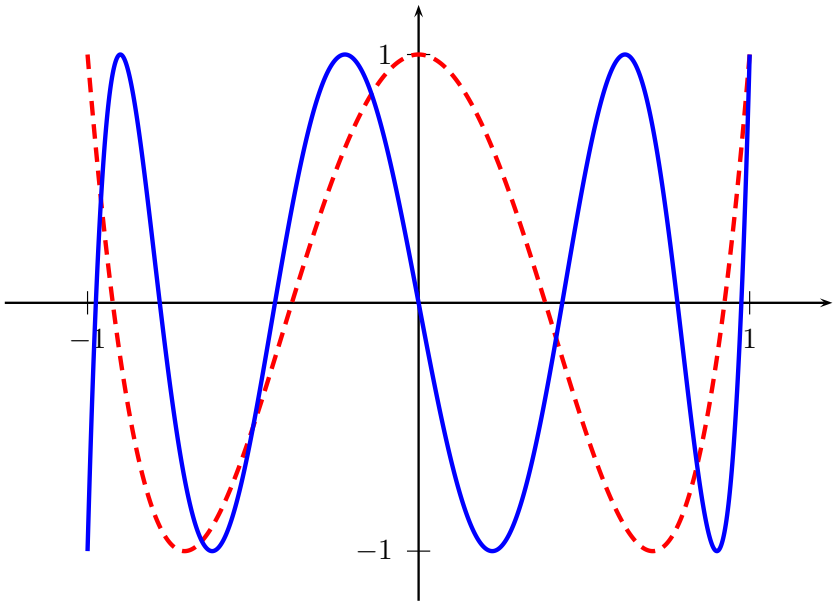

Figure 86: Tchebycheff polinomials. In red dashed line is represented the $T(\omega)$ of fourth order, with the blue line a $T(\omega)$ of the seventh order.

However, the requirements in the filters projects are mainly related to the *return loss*, so, in order to calculate (A.13), L_{Ar} is given by:

$$L_{Ar} = -10\log_{10}\left(1 - 10^{\frac{RL}{10}}\right) \tag{A.14}$$

A.3 BANDPASS TRANSFORMATION

To convert che lowpass prototype of Fig. 82 into a bandpass one, a transformation is required. The band-edges at $\omega_1' = \pm 1$ in the lowpass prototype must map into the band-edges of the bandpass filter ω_1 and ω_2 like in Fig. 80. The trasmission zeros at infinity in the lowpass must now occur at both $\omega = 0$ and $\omega = \infty$. The midband of the lowpass prototype at $\omega' = 0$ must map into the centre of the passband in the bandpass filter ω_0. This can be achieved by the following transformation:

$$\omega' \rightarrow \frac{1}{w}\left(\frac{\omega}{\omega_0} - \frac{\omega_0}{\omega}\right) \tag{A.15}$$

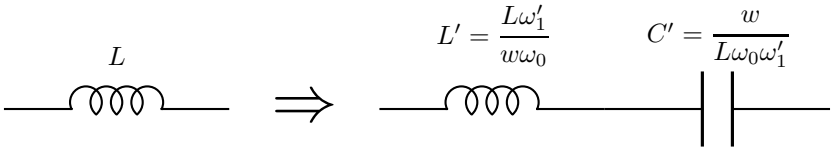

Figure 87: Bandpass transformations of an inductor.

For $\omega' = -1$ and $\omega' = +1$ to map to ω_1 and ω_2 then:

$$-1 = \frac{1}{w}\left(\frac{\omega_1}{\omega_0} - \frac{\omega_0}{\omega_1}\right) \tag{A.16}$$

$$+1 = \frac{1}{w}\left(\frac{\omega_2}{\omega_0} - \frac{\omega_0}{\omega_2}\right) \tag{A.17}$$

By solving equations (A.16) and (A.17) are obtained:

$$\omega_0 = \sqrt{\omega_1 \cdot \omega_2} \tag{A.18}$$

$$w = \frac{\omega_2 - \omega_1}{\omega_0} \tag{A.19}$$

ω_0 is thus the geometric midband frequency; w is the *fractional bandwidth* and its reciprocal value is also known as *bandwidth scaling factor*.

At this point performing the transformation (A.15) to a serie inductor we obtain:

$$\begin{aligned} Z = \jmath\omega' L \Rightarrow \jmath L\frac{1}{w}\left(\frac{\omega}{\omega_0} - \frac{\omega_0}{\omega}\right) \\ = \jmath\left(\frac{L}{w\omega_0}\right)\omega - \frac{\jmath}{\omega\frac{1}{(L\omega_0/w)}} \end{aligned} \tag{A.20}$$

The resulting impedance is that of a series connected L-C circuit in which $L' = \frac{L}{w\omega_0}$ and $C' = \frac{w}{L\omega_0}$ like depicted in Fig. 87.

In a dual way is possible to calculate the admittance of a shunt capacitor after the bandpass transformation

$$\begin{aligned} Y = \jmath\omega' C \Rightarrow \jmath L\frac{1}{w}\left(\frac{\omega}{\omega_0} - \frac{\omega_0}{\omega}\right) \\ = \jmath\left(\frac{C}{w\omega_0}\right)\omega - \frac{\jmath}{\omega\frac{1}{(C\omega_0/w)}} \end{aligned} \tag{A.21}$$

that corresponds to a parallel L-C circuit with $C' = \frac{C}{w\omega_0}$ and $L' = \frac{w}{C\omega_0}$ like shown in Fig. 88. With relations (A.20) and (A.21)

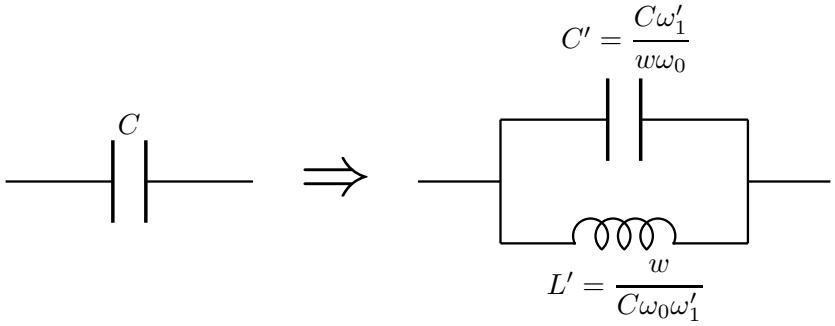

Figure 88: Bandpass transformations of a capacitor.

the lowpass filter of Fig. 84 is transformed to the bandpass filter of Fig. 89.

The values of L_k and C_k are directly obtained by expressions (A.20) and (A.21) and are for even (serie arms) and odd (shunt arms) subscript:

$$L_{k_{odd}} = \frac{w}{\omega_o \omega_1' g_k} \tag{A.22a}$$

$$C_{k_{odd}} = \frac{\omega_1' g_k}{w\omega_0} \tag{A.22b}$$

$$L_{k_{even}} = \frac{\omega_1' g_k}{w\omega_0} \tag{A.22c}$$

$$C_{k_{even}} = \frac{w}{\omega_o \omega_1' g_k} \tag{A.22d}$$

The dual form of bandpass filter is the band-stop which has the same prototype of the last one except for having the series and shunt resonators respectively exchanged, in a very similar way like the lowpass and the highpass prototype fiters. With relations (A.22) is immediate to obtain this important equation:

$$L_k C_k = \frac{1}{\omega_0^2} \tag{A.23}$$

that is valid for each value of k.

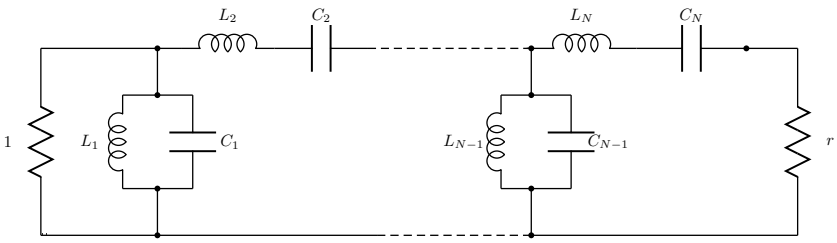

Figure 89: Bandpass prototype filter

A.3.1 Immittance inverters

In deriving design equations for certain types of bandpass and bandstop filters it is desirable to convert the prototype if Fig. 89 which use both inductances and capacitance to equivalent forms which use only series or only parallel resonators. This can be done with the aid of the idealized inverters which are symbolized in Fig. 90

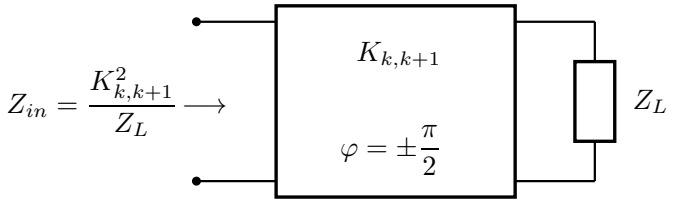

(a) K inverter

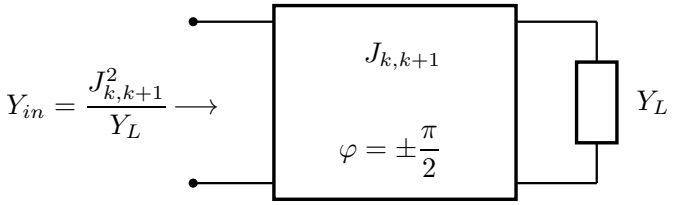

(b) J inverter

Figure 90: Definition of impedance and admittance inverters

An idealized *impedance inverter* operates like a quarter-wavelength line of characteristic impedance K at all frequencies. Therefore, if it is terminated in an impedance Z_L, the input impedance Z_{in} seen looking at the other end is:

$$Z_{in} = \frac{K^2}{Z_L} \tag{A.24}$$

In a dual way is defined the *admittance inverter* like a quarter-wavelength of line of characteristic admittance J at all frequencies. The input admittance seen looking in a J-inverter terminated to a Y_L load is:

$$Y_{in} = \frac{J^2}{Y_L} \tag{A.25}$$

With the term *immittance inverter* is usually to indicate both the impedance and admittance inverters. The figure 90a depicts the idealized structure and definition af an impedance inverters with K parameter of inversion (for this reason is common to call it *K-inverter*). In Fig. 90b is represented the admittance inverter

(or *J-inverter*). Both of them may have an image phase shift of either ± 90 degrees or an odd multiple factor.

Becouse of the inverting action indicated by equations (A.24) and (A.25), a series inductance with an inverter on each side looks like a shunt capacitance from its exterior terminals. Likewise, a shunt capacitance with a inverter on both sides looks like a series inductance from its external terminals. This property can be applied also to a serie or parallel resonator. By a realization point of view, filter of Fig. 89, composed by both series and shunt resonators, is not practical because a structure with only parallel, or only shunt, resonators is preferred. For this reason the immittance inverters are employed to achieve this goal like shown in Fig. 91.

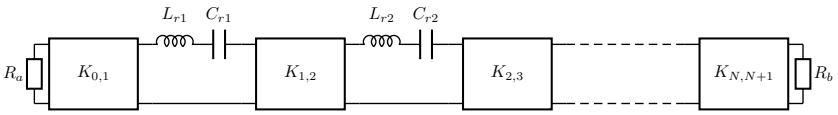

Figure 91: Bandpass prototype filter with K-inverters

In order to generalize the problem and to obtain relations of the K-inverters that are indipendent from the type of application, the values of inductors and capacitors of Fig. 91 are not the same of those of Fig. 89: in this example each element has a r subscript. This is because the two types of structure have a different impedance level that must be corrected.

If is calculated the impedance seen at a plane after the second resonator towards the source, like drawn in Fig. 92, indicating with $Z_{0,in}$ the impedance of the bandpass prototype and with $Z_{r,in}$ the impedance after the second resonator of the bandpass filter with K-inverters, is to be

$$Z_{0,in} = Z_{r,in} \tag{A.26}$$

so the expression for both $Z_{0,in}$ and $Z_{r,in}$ will be calculated in order to obtain che general expression of inversion parameters.

$$\begin{aligned} Z_{0,in} &= j\omega L_2 + \frac{1}{j\omega C_2} + \frac{1}{j\omega C_1 + \dfrac{1}{j\omega L_1} + 1} \\ &= \sqrt{\frac{L_2}{C_2}} \left[j\left(\frac{\omega}{\omega_0} - \frac{\omega_0}{\omega}\right) + \frac{\sqrt{\dfrac{C_2 C_1}{L_2 L_1}}}{j\left(\dfrac{\omega}{\omega_0} - \dfrac{\omega_0}{\omega}\right) + \sqrt{\dfrac{C_1}{L_1}}} \right] \end{aligned} \tag{A.27}$$

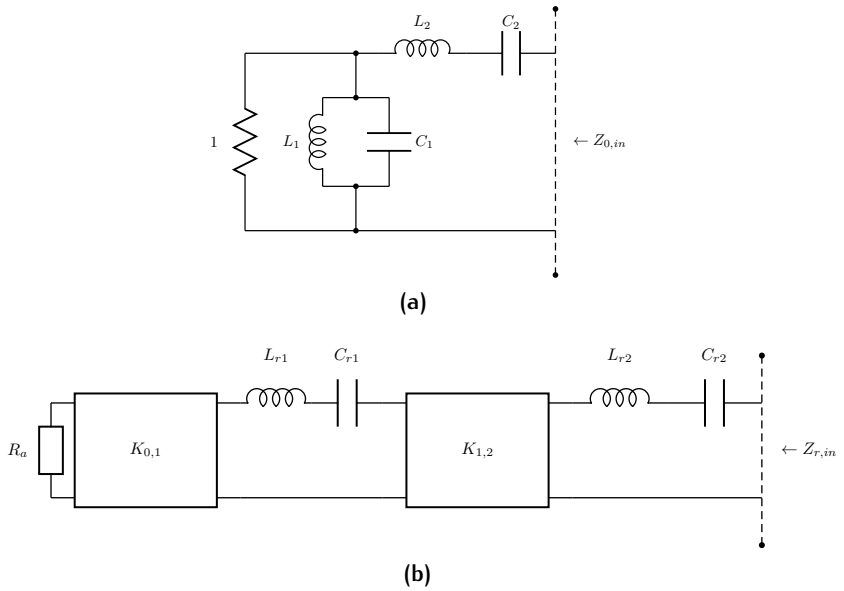

Figure 92: Bandpass with a cut-plane. The impedance seen at the dashed line must be the same for both filters.

Note that in the previous passage the relation (A.23) was used. The same strategy is applied to the second part of Fig. 92.

$$
\begin{aligned}
Z_{r,in} &= \jmath\omega L_{r2} + \frac{1}{\jmath\omega C_{r2}} + \frac{K_{1,2}^2}{\jmath\omega L_{r1} + \dfrac{1}{\jmath\omega C_{r1}} + \dfrac{K_{0,1}^2}{R_a}} \\
&= \sqrt{\frac{L_{r2}}{C_{r2}}} \left[\jmath\left(\frac{\omega}{\omega_0} - \frac{\omega_0}{\omega}\right) + \frac{K_{1,2}^2 \sqrt{\dfrac{C_{r2}C_{r1}}{L_{r2}L_{r1}}}}{\jmath\left(\dfrac{\omega}{\omega_0} - \dfrac{\omega_0}{\omega}\right) + \dfrac{K_{0,1}^2}{R_a}\sqrt{\dfrac{C_{r1}}{L_{r1}}}} \right]
\end{aligned}
\tag{A.28}
$$

where the fundamental relation of an impedance inverter (A.24) was used. Looking to equations (A.27) and (A.28), we can see that they are the same functions of ω except for a constant $\sqrt{L_{r2}/C_{r2}}$ in place of $\sqrt{L_2/C_2}$, which represents a change of

impedance level if we make the quantity inside the square brackets the same. Hence, let

$$K_{1,2}^2\sqrt{\frac{C_{r2}C_{r1}}{L_{r2}C_{r1}}} = \sqrt{\frac{C_2L_1}{L_2C_1}}$$
$$\frac{K_{0,1}^2}{R_a}\sqrt{\frac{C_{r1}}{L_{r1}}} = \sqrt{\frac{L_1}{C_1}}$$

so that operating some simple calculation and using relation (A.23) we obtain:

$$K_{0,1} = \sqrt{\frac{L_{r1}R_a}{C_1}} \tag{A.29}$$

$$K_{1,2} = \sqrt{\frac{L_{r1}L_{r2}}{L_1C_2}} \tag{A.30}$$

With the aid of the relations (A.22), we may write, for arms k and $k+1$:

$$K_{0,1} = \sqrt{\frac{\omega_0 w}{\omega_1'}\cdot\frac{L_{r1}R_a}{g_1}} \tag{A.31a}$$

$$K_{k,k+1} = \frac{\omega_0 w}{\omega_1'}\sqrt{\frac{L_{rk}L_{r,k+1}}{g_k g_{k+1}}} \tag{A.31b}$$

$$K_{N,N+1} = \sqrt{\frac{\omega_0 w}{\omega_1'}\cdot\frac{L_{rN}R_b}{g_N}} \tag{A.31c}$$

Considering a circuit of input impedance expressed by its real part and imaginary part like

$$Z(\omega) = R(\omega) + jX(\omega)$$

or the admittance

$$Y(\omega) = G(\omega) + jB(\omega)$$

the *slope* parameter is defined as the variation of the reactance, for a serie circuit, or the susceptance at central frequency:

$$x = \frac{\omega_0}{2}\frac{\partial X(\omega)}{\partial\omega}\bigg|_{\omega=\omega_0} \tag{A.32}$$

$$b = \frac{\omega_0}{2}\frac{\partial B(\omega)}{\partial\omega}\bigg|_{\omega=\omega_0} \tag{A.33}$$

In this way the for a serie resonator with the formula (A.32) is

$$x_k = \omega_0 L = \frac{1}{\omega_0 C} = \frac{\omega_1' g_k}{w} \tag{A.34}$$

in the same way for a parallel resonator:

$$b_j = \omega_0 C = \frac{1}{\omega_0 L} = \frac{\omega_1' g_j}{w} \tag{A.35}$$

Since the lumped-element circuits are difficult to construct at microwave frequencies, it is usually desiderable to realize the resonators in distributed-element forms rather than the lumped-element forms in Fig. 89 and 91. As a basis for establishing the resonance properties of resonators regardless of their form it is convenient to specify their *rosonance frequency* ω_0 and their *slope* parameter. Any resonator that exhibit a series-type resonance the reactance slope parameter is given by (A.32), for a parallel resonator formula (A.33).

A.4 DIRECT COUPLED FILTERS

Fig. 93 shows a generalized circuit for a bandpass filter having impedance inverters and series-type resonator characteristics. The filter is designed from a lowpass prototype having a response like that of Fig. 85 or 86 and having prototype parameters g_1, g_2, g_3, ..., g_{N+1} and ω_1' band edge.

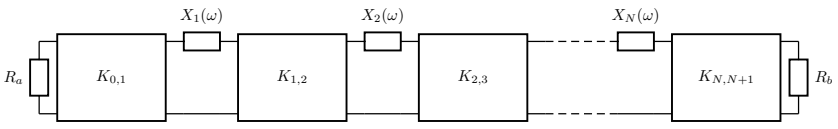

Figure 93: Generalized bandpass filter circuit

The resonator slope parameters x_1, x_2, x_3, ..., x_N for the bandpass filter may be selected arbitraly to be of any size corresponding to convenient resonator designs. Likewise, the terminations R_a, R_b and the fractional bandwidth w may be specified as desired. The K inverters relations are obtained combaining

slope parameters definitions (A.33), (A.33) with relations (A.31):

$$K_{0,1} = \sqrt{\frac{R_a x_1 w}{g_0 g_1 \omega_1'}} \tag{A.36a}$$

$$K_{j,j+1} = \frac{w}{\omega_1'}\sqrt{\frac{x_j x_{j+1}}{g_j g_{j+1}}} \tag{A.36b}$$

$$K_{N,N+1} = \sqrt{\frac{R_b x_N w}{\omega_1' g_N g_{N+1}}} \tag{A.36c}$$

The definition equations of K-inverters (A.36) are indipendent to the type or resonators used, the trasmission lines and characteristic impedance.

A.4.1 Practical realization of immittance inverters

One of the simplest forms of ivnerters is a quarter-wavelength of transmission line. This invertion property is relatively narrow-band nature, a quarter-wavelength line can be used satisfactorily as an impedance or admittance inverter in narrow-band filters.

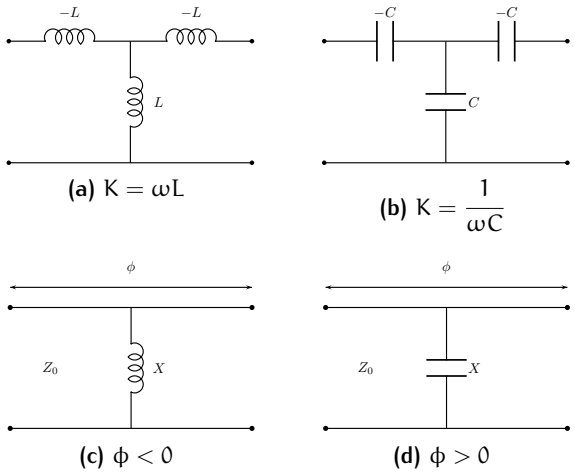

(a) $K = \omega L$ **(b)** $K = \frac{1}{\omega C}$ **(c)** $\phi < 0$ **(d)** $\phi > 0$

Figure 94: Common circuits for K-inverters. This type of circuits are used with series resonators.

Besides a quarter-wavalength line, there are numerous other circuits which operate as inverters. All necessarily give an image phase of odd multiple of $\varphi \pm 90$ degrees, and many have good inverting properties over a much wider bandwidth. Fig. 94 shows four inverting circuits which are useful in filters where the negative L or C can be absorbed into adjacent series elements of the

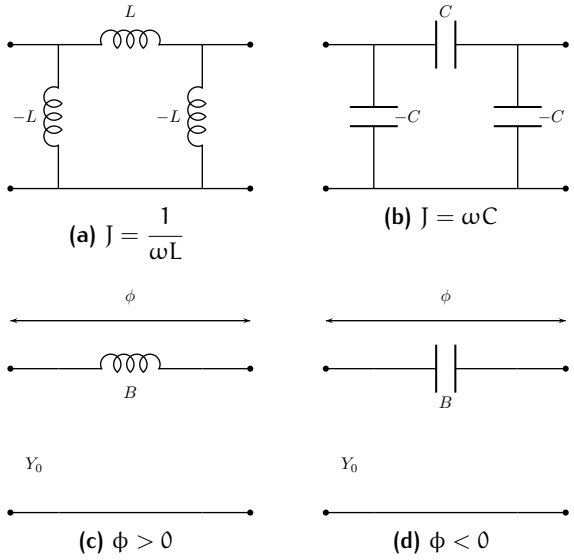

Figure 95: Common circuits for J-inverters. This type of circuits are used with shunt resonators.

same type so as to give a resulting circuit having all positive elements. The inverters shown in Figs. 94(c),(d) are particularly useful in circuits where the line of positive or negative electrical length ϕ shown in hte figures can be added or substracted from adjacent lines of the *same impedance*. The circuits shown at Figs. 94(a) and (c) have an over-all image phase shift of -90 degrees, while those at Figs. 94(b) and (d) have an over-all image phase shift of $+90$ degrees. Totally, networks of Figs. 94 are much more broadband inverters than is a quarter-wavelength line: in the cases of (c) and (d) this statement assumes that $|X/Z_0| \ll 1$ which is usually the case in the practical application of these circuits.

The calculation of K and φ parameters of networks of Figs. 94(a) and (b) is performed with the *eigenvalue method*: taking for example circuit Fig. 94(a), if we put respectivelly and electric and a magnetic wall, the shorted circuit impedance and the open circuit impedance are $Z_{sc} = -\jmath\omega L$ and $Z_{sc} = \jmath\omega L$ and through the use of well-known relationships

$$K = \sqrt{Z_{sc} Z_{oc}} = \omega L \tag{A.37}$$

$$\varphi = 2 \arctan\left(\pm\sqrt{\frac{-Z_{sc}}{Z_{oc}}}\right) = \pm\frac{\pi}{2} \tag{A.38}$$

In the case of the shunt inductive reactance, $X = \omega L$ (Fig. 94(c)), negative electrical lengths are required on each side of the re-

actance. The formulas may be derived conveniently from the short/open circuit impedance of half the structure:

$$\begin{aligned}\varphi &= 2\arctan\left(\pm\sqrt{\frac{-X_{sc}}{X_{oc}}}\right)\\ &= 2\arctan\sqrt{\frac{Z_0\tan\frac{\phi}{2}}{Z_0\tan\left[\frac{\phi}{2}+\arctan\left(\frac{2\omega L}{Z_0}\right)\right]}}\end{aligned} \tag{A.39}$$

$$K = Z_0\sqrt{-\tan\left(\frac{\phi}{2}\right)\tan\left[\frac{\phi}{2}+\arctan\left(\frac{2\omega L}{Z_0}\right)\right]} \tag{A.40}$$

If we set $\varphi = \pm\frac{\pi}{2}$, it is necessary at ω_0 that

$$K = Z_0\tan\left|\frac{\phi}{2}\right| \tag{A.41a}$$

$$\phi = -\arctan\frac{2X}{Z_0} \tag{A.41b}$$

$$\left|\frac{X}{Z_0}\right| = \frac{K/Z_0}{1-(K/Z_0)^2} \tag{A.41c}$$

A dual analogous procudere can be applied to networks and circuits of Fig. 95 obtaining:

$$J = Y_0\tan\left|\frac{\phi}{2}\right| \tag{A.42a}$$

$$\phi = -\arctan\frac{2B}{Y_0} \tag{A.42b}$$

$$\left|\frac{B}{Y_0}\right| = \frac{J/Y_0}{1-(J/Y_0)^2} \tag{A.42c}$$

A.4.2 Half wavelength resonators

Is not rare that in microwave filters a piece of transmission line is used as a resonator terminated, ideally, in either an open circuit or a short circuit. There are two many categories of resonators: series and shunt resonators.

Circuits represented in Fig. 96 are two transmission lines of characteristic impedance Z_0 and Y_0. The first is loaded with a shorted circuit and the second with an open one. It is well

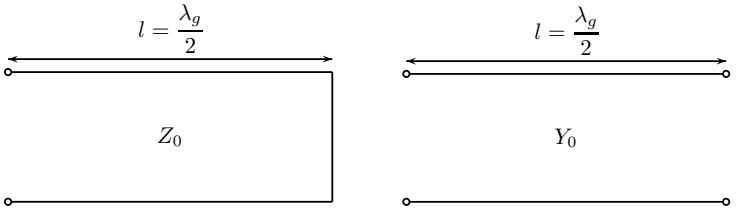

(a) Serie **(b)** Shunt

Figure 96: Serie and shunt half-wavelength resonators.

known that at a central frequency the resonance condition imposes that the reactance, or the susceptance, is zero:

$$X(\omega_0) = 0 \tag{A.43}$$

so if we consider a lossless transmission line and we want to find out the length of the lines of Fig. 96 that get the resonant condition (A.43) verified, equation (A.44) must bu zero at central frequency for both circuits.

$$X_{in} = jZ_0 \tan(\beta l) \tag{A.44}$$

This is accomplished when $\beta l = \pi$ ad so the length of transmission line is:

$$l = \frac{\lambda_g}{2} \tag{A.45}$$

where λ_g is the wavelength into the transmission line, that for ones propagating TE or TM modes of cut-off wavelength λ_c is:

$$\lambda_g = \frac{\lambda}{\sqrt{1 - \left(\frac{\lambda}{\lambda_c}\right)^2}} \tag{A.46}$$

In order to calculate the reactance slope parameter, combaining eqs (A.32) and (A.44) are obtained this relations:

$$x = \frac{\pi}{2} Z_0 \left(\frac{\lambda_g}{\lambda_0}\right)^2 \tag{A.47}$$

$$b = \frac{\pi}{2} Y_0 \left(\frac{\lambda_g}{\lambda_0}\right)^2 \tag{A.48}$$

The values of the slope are used in the calculation of K-inverter parameters in a prototype of all equal resonators of the filter.

If Fig. 97 are represented equivalent circuit of series and parallel resonators. Fig. 97a is the RLC equivalent circuit for the

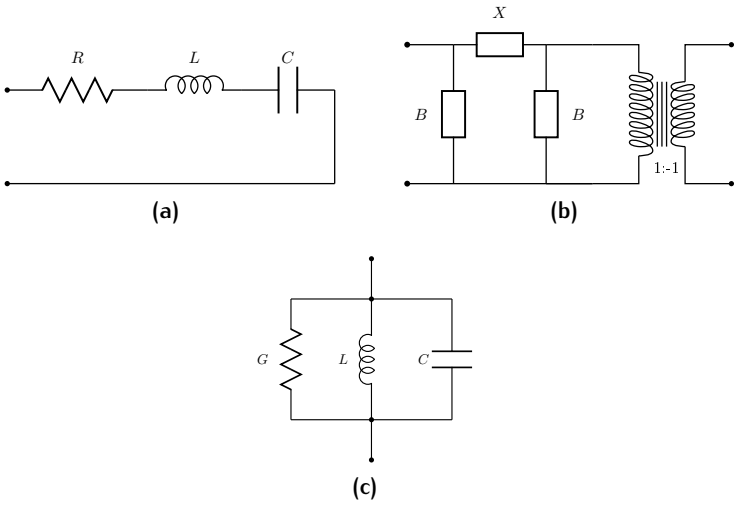

Figure 97: Equivalent circuits for serie and shunt half-wavelength resonators.

series resonator; the presence of the resistance R is not considered ($R = 0$) in the studying of lossless resonators. In Fig. 97b is possible to see tree reactive elements which provide the frequency dependance of the circuit, while the ideal transformer provides the phase reversal of a half-wave line. If the electrical length of the resonator is $\theta = \beta l$ the reactive elements of Fig. 97b are

$$X = Z_0 \sin\theta \tag{A.49}$$

$$B = -Y_0 \cot\frac{\theta}{2} \tag{A.50}$$

The parallel equivalent circuit is depicted in Fig. 97c in which the conductance G is not included ($G = 0$) in the lossless case.

In the case of coupled filters the impedance inverters are replaced by coupling discontinuities. This structures that were presented in Fig. 94 and 95 are in practice discontinuities that excite high order modes. Since this superior excited modes are generally below cut-off, they remain confinated to the coupling discontinuity like stored energy. This energy can be modeled by an inductor or a capacitor depending if the energy is magnetic or electric type. The presence of an additional reactive component (L or C) has the consequence to be absorbed in to the adiacent resonator. In this way the resonant frequency of the filter is shifted and it is no more f_0 because in the

$$\omega = \frac{1}{\sqrt{LC}} \tag{A.51}$$

parameters L and C of the equivalent circuit of resonator have been changed. To correct this behavior lenght of resonator is adjusted in order to re-obtain the desired resonance frequency f_0. The electrical lengths mentioned in section A.4.1 have the purpose to correct the length of adiacent resonators. Basically a half-wavelength resonator has an electrical length of π, so the real electrical length after correction due to the presence of discontinuity is:

$$\theta_k = \pi + \frac{\phi_{k-1,k}}{2} + \frac{\phi_{k,k+1}}{2} \tag{A.52}$$

To notice that in (A.52) values of ϕ_k can be negative: this brings to a shortening of the length of resonator.

A.4.3 Quarter wavelength resonators

Half-wavelength resonators are widely used but they have the disadvantage of the repetition at $2f_0$. To avoid the problem of repetition resonators with quarter-wavelength are used. They have some other advantages [24] like a shorted length, a second bandpass centered at $3f_0$, higher mid-stop-band attenuation. The filters using quarter-wavelength are used in a analogous way of half-wavelenght, but they themselves have inverting effect so that if at one end of each resonator they behave like series resonators, at their other ends they will operate like shunt resonators. For this particular property, they must see a high impedance at one end and a low impedance at the other end. It can be shown [46] that filters can be constructed using two-port, quarter-wavelength resonators if they are coupled alternately by K and J-inverters. The design procedure is much the same as for the preceding cases. Inversion values are obtained by eqs. (A.53).

$$\frac{K_{01}}{Z_0} = \sqrt{\frac{\pi w}{4 g_0 g_1 \omega_1'}} \tag{A.53a}$$

$$\frac{J_{j,j+1}}{Y_0} = \frac{K_{j,j+1}}{Z_0} = \frac{\pi w}{4\omega_1'} \frac{1}{\sqrt{g_j g_{j+1}}} \qquad j = 1 \ \ldots \ N-1 \tag{A.53b}$$

$$\frac{K_{N,N+1}}{Z_0} = \sqrt{\frac{\pi w}{4 g_N g_{N+1} \omega_1'}} \tag{A.53c}$$

Prototype circuit may be started out with either a K inverter or a J inverter, but from there on the K and J inverters must alternate. The basic electrical length of resonators of this type of filters is $\pi/2$ at central frequency. However the length of each resonator

must be correct in order to take into account the effect of the coupling discontinuity. Referring to Figs 94 and 95 the electrical length k-resonator is:

$$\theta_k = \frac{\pi}{2} + \frac{\phi_{k-1,k}}{2} + \frac{\phi_{k,k+1}}{2} \tag{A.54}$$

BIBLIOGRAPHY

[1] (2010), «FEST^{3D} Full-wave Electromagnetic Simulation Tool (by ESA/ESTEC)», http://www.fest3d.com/. (Cited on page 93.)

[2] Awai, I. e Zhang, Y. (2005), «New expression of coupling coefficient between resonators based on overlap integral of EM field», in «Microwave Conference Proceedings, 2005. APMC 2005. Asia-Pacific Conference Proceedings», vol. 4, p. 4 pp.

[3] Awai, I. e Zhang, Y. (2008), «Separation of Coupling Coefficient Between Resonators into Magnetic and Electric Components Toward Its Application to BPF Development», in «Microwave Conference, 2008 China-Japan Joint», p. 61 –65.

[4] Bastioli, S., Marcaccioli, L. e Sorrentino, R. (2008), «Waveguide Pseudoelliptic Filters Using Slant and Transverse Rectangular Ridge Resonators», *Microwave Theory and Techniques, IEEE Transactions on*, vol. 56 (12), p. 3129 –3136. (Cited on page 13.)

[5] Bornemann, J. e Arndt, F. (1990), «Transverse resonance, standing wave, and resonator formulations of the ridge waveguide eigenvalue problem and its application to the design of E-plane finned waveguide filters», *Microwave Theory and Techniques, IEEE Transactions on*, vol. 38 (8), p. 1104 –1113.

[6] Bui, L., Ball, D. e Itoh, T. (1984), «Broadband Millimeter-Wave E-Plane Bandpass Filters», in «Microwave Symposium Digest, MTT-S International», vol. 84, p. 236 – 237.

[7] Chen, T.-S. (1957), «Calculation of the Parameters of Ridge Waveguides», *Microwave Theory and Techniques, IRE Transactions on*, vol. 5 (1), p. 12 –17. (Cited on page 21.)

[8] Cohn, S. (1947), «Properties of Ridge Wave Guide», *Proceedings of the IRE*, vol. 35 (8), p. 783 – 788. (Cited on pages 15 and 24.)

[9] Cohn, S. (1955), «Optimum Design of Stepped Transmission-Line Transformers», *Microwave Theory*

and Techniques, IRE Transactions on, vol. 3 (3), p. 16 –20. (Cited on page 26.)

[10] Cohn, S. (1957), «Direct-Coupled-Resonator Filters», *Proceedings of the IRE*, vol. 45 (2), p. 187 –196. (Cited on page 133.)

[11] Couffignal, P., Nanan, J.-C., Tao, J., Baudrand, H. e Theron, B. (1990), «A Multimodal Variational Approach for the Characterization of Waveguide Discontinuities for Microwave Filter Design», in «Microwave Conference, 1990. 20th European», vol. 1, p. 919 –924. (Cited on page 29.)

[12] Craven, G. e Mok, C. (1971), «The Design of Evanescent Mode Waveguide Bandpass Filters for a Prescribed Insertion Loss Characteristic», *Microwave Theory and Techniques, IEEE Transactions on*, vol. 19 (3), p. 295 – 308. (Cited on pages 13 and 30.)

[13] Craven, G., Mok, C. K. e Skedd, R. F. (1969), «Integrated Microwave Systems Employing Evanescent Mode Waveguide Components», in «Microwave Conference, 1969. 1st European», p. 285 –289.

[14] Craven, G. F. e Skedd, R. F. (1987), *Evanescent mode microwave components*. (Cited on page 30.)

[15] Fahmi, M., Ruiz-Cruz, J., Mansour, R. e Zaki, K. (2009), «Compact Ridge Waveguide Filters With Arbitrarily Placed Transmission Zeros Using Nonresonating Nodes», *Microwave Theory and Techniques, IEEE Transactions on*, vol. 57 (12), p. 3354 –3361. (Cited on page 85.)

[16] Gao, J. (2001), «Analytical calculation of the coupling coefficient of a waveguide-cavity coupling system», in «Particle Accelerator Conference, 2001. PAC 2001. Proceedings of the 2001», vol. 2, p. 957 –959 vol.2.

[17] Helszajn, J. (2000), *Ridge waveguide and passive microwave components*, Institution of Electrical Engineers, Stevenage, UK. (Cited on page 16.)

[18] Hensperger, E. (1958), «Broad-Band Stepped Transformers from Rectangular to Double-Ridged Waveguide», *Microwave Theory and Techniques, IRE Transactions on*, vol. 6 (3), p. 311 –314. (Cited on page 26.)

[19] Hoefer, W. e Burton, M. (1982), «Closed-Form Expressions for the Parameters of Finned and Ridged Waveguides», *Microwave Theory and Techniques, IEEE Transactions on*, vol. 30 (12), p. 2190 –2194. (Cited on page 17.)

[20] Hopfer, S. (1955), «The Design of Ridged Waveguides», *Microwave Theory and Techniques, IRE Transactions on*, vol. 3 (5), p. 20 –29. (Cited on pages 15, 17, 20, and 33.)

[21] Levy, R. (1967), «Theory of Direct-Coupled-Cavity Filters», *Microwave Theory and Techniques, IEEE Transactions on*, vol. 15 (6), p. 340 – 348. (Cited on page 39.)

[22] Levy, R. (1973), «A Generalized Design Technique for Practical Distributed Reciprocal Ladder Networks», *Microwave Theory and Techniques, IEEE Transactions on*, vol. 21 (8), p. 519 – 526. (Cited on page 36.)

[23] Marcuvitz, N. (1986), *Waveguide handbook*, Institution of Electrical Engineers, Stevenage, UK. (Cited on page 17.)

[24] Matthaei, G. (1958), «Direct-coupled, band-pass filters with $\lambda_o/4$ resonators», vol. 6, p. 98 – 111. (Cited on page 149.)

[25] Matthaei, G. L., Jones, E. e Young, L. (1964), *Microwave filters, impedance-matching networks, and coupling structures*, McGraw-Hill, New York, NY. (Cited on pages 71, 92, and 134.)

[26] McKay, M. e Helszajn, J. (1999), «Voltage-current definition of impedance of single-ridge waveguide», *Microwave and Guided Wave Letters, IEEE*, vol. 9 (2), p. 66 –68. (Cited on page 24.)

[27] Mok, C., Stopp, D. e Craven, G. (1972), «Susceptance-loaded evanescent-mode waveguide filters», *Electrical Engineers, Proceedings of the Institution of*, vol. 119 (4), p. 416 –420.

[28] Nanan, J.-C., Tao, J.-W., Baudrand, H., Theron, B. e Vigneron, S. (1991), «A two-step synthesis of broadband ridged waveguide bandpass filters with improved performances», *Microwave Theory and Techniques, IEEE Transactions on*, vol. 39 (12), p. 2192 –2197. (Cited on pages 13 and 30.)

[29] Pyle, J. (1966), «The Cutoff Wavelength of the TE10 Mode in Ridged Rectangular Waveguide of Any Aspect Ratio», *Microwave Theory and Techniques, IEEE Transactions on*, vol. 14 (4), p. 175 – 183. (Cited on page 17.)

[30] Rong, Y., Zaki, A., Gipprich, J., Hageman, M. e Stevens, D. (1999), «LTCC wide-band ridge-waveguide bandpass filters», *Microwave Theory and Techniques, IEEE Transactions on*, vol. 47 (9), p. 1836 –1840. (Cited on pages 13 and 85.)

[31] Ruiz-Cruz, J., Sabbagh, M., Zaki, K., Rebollar, J. e Zhang, Y. (2005), «Canonical ridge waveguide filters in LTCC or metallic resonators», *Microwave Theory and Techniques, IEEE Transactions on*, vol. 53 (1), p. 174 – 182.

[32] Saad, A. (1984), «Novel Lowpass Harmonic Filters for Satellite Application», in «Microwave Symposium Digest, MTT-S International», vol. 84, p. 292 – 294.

[33] Saad, A. (1987), «A Unified Ridge Structure for Evanescent Mode Wideband Harmonic Filters: Analysis and Applications», in «Microwave Conference, 1987. 17th European», p. 157 –162. (Cited on page 13.)

[34] Saad, A., Mitha, A. e Brown, R. (1986), «Evanescent Mode-Serrated Ridge Waveguide Bandpass Harmonic Filters», in «Microwave Conference, 1986. 16th European», p. 287 –291. (Cited on page 85.)

[35] Sakiotis, N. e Chait, H. (1959), «Broad-Band Ferrite Rotators Using Quadruply-Ridged Circular Waveguide», *Microwave Theory and Techniques, IRE Transactions on*, vol. 7 (1), p. 38 –41. (Cited on page 15.)

[36] Shen, T. e Zaki, K. (2001), «Length reduction of evanescent-mode ridge waveguide bandpass filters», in «Microwave Symposium Digest, 2001 IEEE MTT-S International», vol. 3, p. 1491 –1494 vol.3. (Cited on pages 13 and 29.)

[37] Shen, T. e Zaki, K. A. (2001), «Folded Evanescent-Mode Ridge Waveguide Bandpass Filters», in «Microwave Conference, 2001. 31st European», p. 1 –4. (Cited on page 85.)

[38] Soto, P. e Boria, V. (2004), «A versatile prototype for the accurate design of homogeneous and inhomogeneous wide bandwidth direct-coupled-cavity filters», vol. 2, p. 451 – 454 Vol.2.

[39] Tao, J. e Baudrand, H. (1988), «Rigorous analysis of triple-ridge waveguides», *Electronics Letters*, vol. 24 (13), p. 820 –821. (Cited on page 13.)

[40] Tao, J. e Baudrand, H. (1991), «Multimodel variational analysis of uniaxial waveguide discontinuities», *Microwave*

Theory and Techniques, IEEE Transactions on, vol. 39 (3), p. 506 –516. (Cited on page 29.)

[41] Vanin, F., Schmitt, D. e Levy, R. (2004), «Dimensional synthesis for wide-band waveguide filters and diplexers», *Microwave Theory and Techniques, IEEE Transactions on*, vol. 52 (11), p. 2488 – 2495. (Cited on page 31.)

[42] Vanin, F., Wollack, E., Zaki, K. e Schmitt, D. (2006), «Polarization-Preserving Quadruple-Ridge Waveguide Filter and Four-fold Symmetric Transformer», in «Microwave Symposium Digest, 2006. IEEE MTT-S International», p. 127 –130. (Cited on page 85.)

[43] Yildirim, N. e Hizal, A. (2005), «Waveguide filters with ridged and unequal width resonators», p. 4 pp. (Cited on page 13.)

[44] Young, L. (1963), «Direct-Coupled Cavity Filters for Wide and Narrow Bandwidths», *Microwave Theory and Techniques, IEEE Transactions on*, vol. 11 (3), p. 162 – 178.

[45] Zaki, K. e Chen, C. (1987), «Coupling of Non-Axially Symmetric Hybrid Modes in Dielectric Resonators», *Microwave Theory and Techniques, IEEE Transactions on*, vol. 35 (12), p. 1136 – 1142. (Cited on page 75.)

[46] Zhang, Q. e Lu, Y. (2009), «Synthesis of wide-band bandpass filters with quarter-wavelength resonators», p. 2037 – 2040. (Cited on page 149.)

[47] Zhang, Q. e Lu, Y. (2010), «Dimensional synthesis method for wide-band waveguide iris filters», *Microwaves, Antennas Propagation, IET*, vol. 4 (9), p. 1256 –1263. (Cited on page 85.)